

EFFECTS OF NOISE ON TELESEISMIC T^* ESTIMATION AND ATTENUATION
TOMOGRAPHY OF THE YELLOWSTONE REGION

by

DAVID C. ADAMS

A DISSERTATION

Presented to the Department of Geological Sciences
and the Graduate School of the University of Oregon
in partial fulfillment of the requirements
for the degree of
Doctor of Philosophy

June 2009

University of Oregon Graduate School

Confirmation of Approval and Acceptance of Dissertation prepared by:

David Adams

Title:

"Effects of Noise on Teleseismic t^* Estimation and Attenuation Tomography of the Yellowstone Region"

This dissertation has been accepted and approved in partial fulfillment of the requirements for the Doctor of Philosophy degree in the Department of Geological Sciences by:

Eugene Humphreys, Chairperson, Geological Sciences

Emilie Hooft Toomey, Member, Geological Sciences

Douglas Toomey, Member, Geological Sciences

James Isenberg, Outside Member, Mathematics

and Richard Linton, Vice President for Research and Graduate Studies/Dean of the Graduate School for the University of Oregon.

June 13, 2009

Original approval signatures are on file with the Graduate School and the University of Oregon Libraries.

© 2009 David C. Adams

An Abstract of the Dissertation of
David C. Adams for the degree of Doctor of Philosophy
in the Department of Geological Sciences to be taken June 2009

Title: EFFECTS OF NOISE ON TELESEISMIC t^* ESTIMATION AND
ATTENUATION TOMOGRAPHY OF THE YELLOWSTONE REGION

Approved: _____
Eugene D. Humphreys

Studies on seismic attenuation are an important complement to those on seismic velocity, especially when interpreting results in terms of temperature. But estimation of attenuation (t^*) is more computationally involved and prone to contamination by noise, especially signal-generated noise. We have examined the effects of various forms of synthetic noise on t^* estimation using time and frequency domain methods with varying window lengths and data frames of reference. We find that for S-waves, error due to noise can be reduced by rotating the data into the estimated polarization direction of the signal, but unless the exact nature of the noise is known, no method or window size is clearly preferable. We recommend the use of multiple estimation methods including a careful assessment of the uncertainty associated with each estimate, which is used as a weight during inversion for $1/Q$. Our synthetic tests demonstrate that the misfit between

actual and estimate-predicted traces or spectra correlates with t^* error, and a similar relationship is suggested for real data.

Applying this approach to data from the Yellowstone Intermountain Seismic Array, we employ two important constraints during inversion. First, we scale the misfit values so that the resulting weights are comparable in magnitude to the squares of the eventual data residuals. Second, we smooth the model so that the maximum attenuation ($1/Q$) does not exceed a value which would totally explain the observed velocity anomaly. The tomographic models from all the estimation methods are similar, but in the vicinity of the Yellowstone mantle plume, S-wave models show greater attenuation than do P-wave models. We attribute this difference to greater focusing by the plume of S-waves. All models show relatively high attenuation for the plume at depth, but above 250 km attenuation in the plume drops rapidly to values less than those of the surrounding mantle. We attribute this drop to the onset of partial melting, which dehydrates the olivine crystals, suppressing dislocation mobility and thereby attenuation. These attenuation models suggest excess plume temperatures at depth which are too low to support a plume origin in the lower mantle.

This dissertation includes unpublished co-authored material.

CURRICULUM VITAE

NAME OF AUTHOR: David Congdon Adams

PLACE OF BIRTH: Boston, Massachusetts

DATE OF BIRTH: March 27, 1952

GRADUATE AND UNDERGRADUATE SCHOOLS ATTENDED:

University of Oregon, Eugene
Montana State University, Bozeman, Montana
Harvard University, Cambridge, Massachusetts

DEGREES AWARDED:

Doctor of Philosophy, Geological Sciences, 2009, University of Oregon
Master of Science in Earth Science, 1997, Montana State University
Bachelor of Arts in Biology, 1976, Harvard University

AREAS OF SPECIAL INTEREST:

Seismology
Geodynamics

PROFESSIONAL EXPERIENCE:

Teaching and research assistant, Department of Geological Sciences,
University of Oregon, 1999-2002
Teaching assistant, Department of Earth Science, Montana State University,
1995-1996

PUBLICATIONS:

Adams, D.C. 1977. Cine analysis of the medullary bundle system in *Cyathea fulva*. *American Fern Journal* **67**:73-80.

Adams, D.C., and P.B. Tomlinson. 1979. *Achrosticum* in Florida. *American Fern Journal* **69**:42-46.

Lageson, D.R., Adams, D.C., Morgan, L., Pierce, K.L., and R.B Smith. 1999. Neogene-Quaternary tectonics and volcanism of southern Jackson Hole, Wyoming and southeastern Idaho, in Hughes, S.S., and Thackray, G.D., eds., *Guidebook to the Geology of Eastern Idaho: Pocatello, Idaho* Museum of Natural History. p. 115-130.

ACKNOWLEDGMENTS

I wish to thank Professor Eugene D. Humphreys for his guidance in this effort and for general inspiration and empowerment. I also wish to thank Professor Douglas R. Toomey for making available additional data and for providing valuable advice in the preparation of this manuscript.

To my wife and children

TABLE OF CONTENTS

Chapter	Page
I. INTRODUCTION	1
1.1. Q and t^*	1
1.2. Noise	2
1.3. Resolution	4
1.4. Input Signal	6
1.5. Noise Mitigation	7
1.6. Description of Work	9
II. EFFECTS OF SIGNAL-GENERATED NOISE ON ESTIMATION OF T^* WITH THE USE OF TELESEISMIC ARRAYS AND STRATEGIES FOR MITIGATION.....	10
2.1. Introduction.....	10
2.2. Teleseismic t^* Estimation.....	12
2.2.1. Frame of Reference.....	12
2.2.2. Spectral Ratio Method	16
2.2.3. Waveform Modeling Method	21
2.2.4. Measures of Uncertainty	26
2.3. Synthetic Noise Tests.....	27

Chapter	Page
2.3.1. Noise Simulation.....	28
2.3.1.1. Lithospheric Scattering	28
2.3.1.2. Rayleigh Waves	28
2.3.1.3. Shear Wave Splitting	29
2.3.1.4. Basin Reverberation.....	29
2.3.1.5. SKS and ScS Arrivals	29
2.4. Results	30
2.4.1. Absolute t^* Error.....	30
2.4.2. Estimate Misfit.....	37
2.4.3. Results with Variable Actual t^*	37
2.4.4. Applicability to Real Data Sets.....	42
2.5. Conclusions.....	47
III. ATTENUATION IN THE LABORATORY – A REVIEW	49
3.1. Laboratory Determination of Q	49
3.2. Physical Mechanisms of Attenuation.....	53
3.2.1. Grain Size.....	53
3.2.2. Dislocation Migration	55
3.2.3. Water Content and Partial Melt	58
3.3. Interpretation of Seismic Data	61

Chapter	Page
IV. ATTENUATION TOMOGRAPHY IN THE YELLOWSTONE REGION.....	62
4.1. Introduction.....	62
4.2. Methods.....	68
4.2.1. t^* Estimation	68
4.2.2. Inversion	68
4.2.3. Absolute Q and the Trade-off Parameter	70
4.3. Results.....	72
4.4. Discussion	76
4.4.1. Decoupling of V and Q Anomalies.....	76
4.4.2. Decoupling of Q_p and Q_s	82
4.4.3. Implications for Estimates of Plume Temperature	88
4.5. Conclusions.....	90
V. CONCLUSIONS.....	92
REFERENCES	94

LIST OF FIGURES

Figure	Page
2.1. Histograms of S-wave Polarization Azimuths.....	14
2.2. Radial (a) and Transverse (b) Components for S-waves Recorded at YISA	15
2.3. Data from Honshu Event Rotated into “Polarized” Frame of Reference	16
2.4. Normalized Amplitude Spectra (Dashed) for the Signals Shown in Figure 2.3..	18
2.5. Regions of Greater Relative Standard Deviation.....	19
2.6. $\log(A/A_0)$ for Station Y22 Versus Frequency	20
2.7. Example of Windowing for the WF Method	23
2.8. Example of Synthetically Attenuated and De-attenuated Traces	24
2.9. Selected Polarized Traces from the Honshu Event	25
2.10. t^* Error, in Seconds, due to Addition of Synthetic Lithospheric Scattering	31
2.11. Absolute t^* Error, in Seconds, due to Addition of Synthetic Noise for SR and WF Methods Versus Noise Parameter.....	32
2.12. Absolute t^* Error, in Seconds, due to Addition of Synthetic Noise for SR and WF Methods Versus Noise Parameter for Each Window Length	34
2.13. Absolute t^* Error, in Seconds, due to Addition of Synthetic Noise for SR and WF Methods Versus Window Size.....	36
2.14. Estimate Misfit due to Addition of Synthetic Noise.....	38
2.15. Mean Estimate Uncertainty Versus Window Length	46
4.1. Depth Slices through 1/Qs Models	73

Figure	Page
4.2. S-wave Ray Density Plot	75
4.3. Depth Slices through 1/Qp Models.....	77
4.4. P-wave Ray Density Plot	79
4.5. Average 1/Q for Plume (Solid) and Non-plume (Dashed) Areas	81
4.6. Depth Slices of Qp/Qs	83
4.7. Average of Normalized Spectra.....	85
4.8. Average of Interpolated t* Maps	87
4.9. Mean Plume ΔT Values Versus Depth	89

LIST OF TABLES

Table	Page
2.1. Representative Body Wave Attenuation Studies	11
2.2. Mean Error, Mean Absolute t^* , and Mean Misfit.....	40
2.3. An Average of Linear Regression Results.....	41
2.4. Mean Absolute t^* and Mean Misfit for the Yellowstone and Galapagos.....	43
2.5. Mean Error, Mean Misfit, and Linear Regression Results	44

CHAPTER I

INTRODUCTION

1.1. Q and t*

Measurement of intrinsic seismic attenuation, i.e. the frequency-dependent loss of a seismic energy due to “internal friction” (Nowick and Berry, 1972), can provide direct information about the physical and compositional nature of the Earth’s interior and indirect information important to the interpretation of seismic velocity data. The effects of seismic attenuation are amplitude loss, especially at higher frequencies, and a reduction of propagation speed, especially at lower frequencies. Attenuation often is quantified by the “quality factor” Q, defined implicitly with

$$A(\omega) = A_0(\omega) \exp[-\omega x / 2 Q(\omega)c(\omega)] \quad (1.1)$$

(Aki and Richards, 2002), where A is the amplitude of a Fourier component of the signal, A_0 is the unattenuated or reference amplitude, ω is the angular frequency, x is the distance traveled in an attenuating body, and c is the phase velocity. The integrated effect of Q on A(ω) as a wave propagates through a volume is given by (Teng, 1968)

$$t^* = \int dx / Q(x)c(x). \quad (1.2)$$

This most often is the quantity used for seismic analysis, but its estimation is computationally much more involved than that of arrival times for velocity studies. In

addition, estimation of seismic attenuation involves analysis of a larger portion of the waveform than does determination of arrival time, and this greatly increases susceptibility to contamination by noise.

1.2. Noise

In seismological studies, noise is best defined as “interfering non-linear elastic effects” (Romanowicz and Durek, 2000). It may represent energy completely unrelated to the signal, often called “random” or “background” noise. The principal sources of these “microseisms” at higher frequencies are wind action and anthropogenic; while at longer periods, especially near the microseism peak (periods of ~5-8 seconds), this noise is due mainly to the action of ocean waves (Shearer, 1999). In practice, noise usually involves direct distortion of the signal or involves signal energy travelling paths other than the assumed raypath.

Included in this signal-generated noise are other phases leaving the seismic source and arriving coincident with the signal. For early-arriving P-waves, this is not an issue. For S-waves such interfering arrivals can include multiples (SS, etc.), depth phases (sS, pS), core phases (SKS) and core reflections (ScS). These arrivals are usually easily identifiable and, for velocity studies, cause little problem in determining arrival times. The longer time windows required for attenuation analysis often result in either unavoidable contamination or rejection of data.

On the receiver side, signal-generated noise is created by lithospheric scattering (including P-S conversions), Rayleigh waves generated by interaction with structure and topography (Levander and Hill, 1985; Clouser and Langston, 1995), shear-wave splitting, and basin (or Moho) reverberations. Seismic energy is also scattered by upwelling mantle plumes (Tilman et al., 1998), and the frequency-dependent focusing and defocusing of the signal can significantly affect apparent attenuation (Allen et al., 1999). Apparent attenuation can occur due to small-scale heterogeneities, i.e. layering, but tends to be restricted to higher frequencies and crustal levels (Schoenberger and Levin, 1974; Aki and Chouet, 1975; Aki, 1982). Attenuation in water-saturated porous rocks (Biot, 1956; O'Connell and Budiansky, 1977) also tends to be limited to very shallow depths.

The longer periods used in the study of surface waves (70-400 seconds) and normal modes (100-3000 seconds) greatly reduce sensitivity to most of the forms of noise which plague attenuation analysis in body waves (2-20 second periods). The presence of lateral heterogeneities still introduces error through focusing-defocusing (Romanowicz, 1990) and mode splitting (Sailor and Dziewonski, 1978) especially at relatively shorter periods. Coupling between body waves and normal modes has also been shown to occur (Marquering et al., 1998). At longer periods, the high-frequency approximation upon which ray-theory is based is increasingly violated (Dziewonski and Steim, 1982).

1.3. Resolution

While body wave attenuation studies are more prone to noise than those of surface waves, in many circumstances they have far better resolution, which depends primarily on frequency and ray coverage. To first order, resolution varies as the square root of the seismic wavelength. More specifically, the smallest feature resolvable must, for the most part, be larger than the width of the first Fresnel zone which in 3 dimensions is

$$w = 2 \sqrt{(\lambda x (L - x) / L)} \quad (1.3)$$

where λ is the wavelength, x is the distance of the feature to the receiver, and L is the total raypath length (Spetzler and Snieder, 2004). For $L = 5000$ km and $x = 400$ km, Fresnel zone widths are on the order of 100-400 km for body waves and 600-1600 for surface waves. The values for the latter can be even larger as the distance to the receiver (x) is usually much greater.

Surface and body waves also differ in resolving power because of their ray coverage. For body waves, raypaths are subvertical and receivers are constrained to locations above the study region. Fresnel zone widths are reduced due to smaller “ x ” values allowing improved lateral resolution. Vertical resolution depends on the number of raypaths crossing at sufficiently high angles at depth. For nearly vertical core reflections (ScS), depth resolution is essentially impossible and most studies provide only whole mantle averages (Jordan and Sipkin, 1977; Sipkin and Jordan, 1979; 1980; Nakanishi, 1979; Lay and Wallace, 1983; 1988; Gomer and Okal, 2003) with the

exception of studies using depth phases (e.g. Flanagan and Wiens, 1994). The depth of crossing rays depends on network aperture (area covered by receiver array). In most cases, this limits resolution to the upper mantle and transition zone (Nolet et al., 2007).

The raypaths of surface waves are essentially horizontal allowing them to sample regions far from the receivers. This makes them preferable to body waves for studies of oceanic regions. Lateral resolution is controlled by the number of crossing raypaths, but increasing interference due to off-path heterogeneities limits resolution to spherical harmonic degree 8 (Selby and Woodhouse, 2002) or about 45 great circle arc degrees. Differential body wave multiples (S-SS-SSS etc) can also sample remote regions at their surface reflection points (Sheehan and Solomon, 1992; Ding and Grand, 1993; Bhattacharyya et al., 1996), but the extremely large Fresnel zone widths at these points call into question the value of this approach (Marquering et al., 1998). Some relatively short path fan-shooting studies (e.g. Allen et al., 1999) can utilize wavelengths comparable to body wave studies to achieve much greater resolution in one but not both lateral dimensions. For surface waves, vertical resolution is solely dependent on seismic wavelength, as longer wavelengths can sample progressively deeper regions. Once again this limits resolution to the upper mantle, and lower mantle studies must exploit the much longer wavelengths of Earth's normal modes.

1.4. Input Signal

In general, the greatest resolution both laterally and vertically is provided by large-aperture teleseismic body wave studies, at least for the upper mantle. Critical to attenuation analysis, however, is accurate knowledge of the original, unattenuated “input” signal. For local source studies (Sanders, 1984; Sanders et al., 1988; Ho-Liu et al., 1988; Lees and Lindley, 1994; Wu and Lees, 1996), this input signal can be directly recorded. Active source attenuation studies (Jacobson et al., 1981; Jacobson, 1987; Jacobson and Lewis, 1990; Wepfer and Christensen, 1990; White and Clowes, 1994; Wilcock et al., 1992; 1995) have the additional advantage of being, to some extent, able to control both ray coverage and the frequency content of the signal. All these near-source studies allow the determination of absolute values for Q , but their shallow raypaths tend to restrict them to the crust and uppermost mantle. As input signals, surface wave studies are able to use the arrival from a previous orbit (e.g. R1 for R3) at a given station or the arrival at a preceding receiver along a great circle raypath. Normal mode studies simply plot the temporal amplitude decay of a given mode. Differential S-wave studies use the S arrival as input, and core reflection studies use the previous ScS arrival. These approaches also yield absolute values for Q .

Raypaths for single-phase teleseismic studies have Fresnel zones which tend to diverge quite proximal to the study area (small x), and the signal for all raypaths can be assumed identical up to the point of divergence. But the nature of the signal at this point cannot be determined, and a reference signal must be arbitrarily selected. Clearly neither the signal at the source nor an apparently unattenuated signal at a receiver outside the

array can adequately approximate the actual path-integrated effects of attenuation and Fresnel zone sensitivity. Accordingly, the reference signal is best derived from the observed traces or spectra usually as some sort of weighted average (e.g. Boyd and Sheehan, 2005). In the frequency domain, each station in turn may be used as a reference (e.g. Allen et al., 1999; Lawrence et al., 2006), but upon demeaning and averaging the results, they tend to be identical to those of the weighted average approach. The “common spectrum” method (Halderman and Davis, 1991) solves for the reference spectrum while inverting for t^* . The spectrum obtained is still not significantly different from a weighted average.

1.5. Noise Mitigation

The use of an averaged signal rather than the actual input signal not only precludes the calculation of absolute Q but also introduces considerable uncertainty for the t^* estimate. This uncertainty is compounded by the effects of noise. Attempts to mitigate these effects primarily seek to increase the signal-to-noise ratio. Initially this involves the selection of a frame of reference which enhances signal energy while suppressing that of noise. Seismic data are normally rotated relative to the raypath into vertical, radial, and transverse components. For P-waves, the vertical component is the straightforward choice. For S-waves the transverse component (SH) is usually preferred over the radial (SV) as the former is less likely to be affected by P-S conversions or the arrival of SKS phases. This choice does not preclude other arrivals (e.g. ScS) or the

effects of the other forms of receiver-side noise, and, depending on source kinematics, actual signal energy can be dominantly radial.

The next step in increasing signal energy relative to noise is the truncation, or windowing, of the signal in either the time or frequency domain such as to avoid noise. It is critical that the nature of the noise be well understood to prevent inadvertent truncation of the signal. In the frequency domain, the most common approach is to examine the spectrum of the pre-arrival portion of the trace as a proxy for the frequency content of the noise and to exclude frequency ranges where noise amplitude exceeds some tolerance level. This of course presumes that the noise is not signal-generated. In the time domain, receiver-side noise is usually not sufficiently separated temporally from the signal to allow effective windowing, but later arriving phases can often be identified and removed.

In some circumstances, a correction can be applied to the t^* estimate to remove the effects of a particular type of noise. Boyd and Sheehan (2005) use the functional relationship between t^* error and basin reverberation arrival time to calculate a correction. The relationship is dependent on the range of frequencies used but appears effective in study areas where sedimentary basins are prevalent.

For the most part, it is not possible to reduce the uncertainties associated with t^* estimates to the levels seen for velocity studies. For single-phase teleseismic attenuation studies, values for Q are derived by tomographic inversion of the t^* estimates, which are commonly weighted by the inverse of their uncertainties usually in the form of their variances. This makes reliable estimation of these uncertainties critical.

1.6. Description of Work

In Chapter II, we develop several alternative methods for t^* estimation, noise mitigation, and estimation of t^* uncertainty, and we test them against other commonly used techniques. This chapter is an excerpt from an article submitted for publication for which my co-author, Eugene D. Humphreys, provided technical guidance and considerable editorial assistance. Some data for this article was provided by D.R. Toomey.

Chapter III is a review of attenuation studies in the laboratory, including methods employed, results, and limitations. Application of experimental findings to seismological studies is also addressed.

In Chapter IV, we apply the preferred methods from Chapter II to a dataset from a seismometer deployment in the Yellowstone region. We discuss the results in regard to possible attenuation mechanisms and the effects of the Yellowstone “mantle plume”. This chapter is an excerpt from another article submitted for publication for which my co-author, Eugene D. Humphreys, again provided technical guidance and considerable editorial assistance.

CHAPTER II

EFFECTS OF SIGNAL-GENERATED NOISE ON ESTIMATION OF T^* WITH THE USE OF TELESEISMIC ARRAYS AND STRATEGIES FOR MITIGATION

This chapter was coauthored by Eugene D. Humphreys.

2.1. Introduction

Numerous frequency- and time- domain methods have been developed to estimate seismic attenuation. Table 2.1 lists some representative studies and the methods and parameters used. These and other methods for estimating t^* have been reviewed by Cormier (1982), Jannsen et al. (1985), and Tonn (1989).

In the following study, we assess quantitatively the error associated with various methods for t^* estimation applied to teleseismic data, and seek an approach that optimizes the quality of t^* estimates. We investigate the effects of t^* estimation methods applied to known signals with synthetic noise added, to synthetic data sets, and to actual data sets from Yellowstone and the Galapagos. After trying many methods of analysis, we focus on the two most successful approaches, a spectral ratio (SR) and a waveform modeling (WF) method. Error is directly measured in the synthetic noise tests allowing us to develop a proxy for estimating uncertainty in real data, which is critical for comparing methods and for data weighting during tomographic inversion for Q .

Table 2.1. Representative body wave attenuation studies listing authors; locales; phases studied; t* estimation method employed: spectral ratio (sr), spectral stacking (ss), spectral modeling (sm), spectral inversion (si), waveform matching (wf), and common spectrum (cs); component analyzed: radial (SV), transverse (SH), vertical (V), and anisotropic fast and slow (F-S); spectral estimation method: multitaper (MT), maximum entropy (ME), and discrete Fourier transform (DFT) with width of moving average smoothing window listed in Hz; length of time window; length of frequency window; reference signal used: actual phase (S, P, ScS), explosive source (x), selected station (s), average of selected stations (as), average of all stations (aa), each station in turn (e), common spectrum (cs), and computed (c); and method of noise level estimation: pre-signal spectral amplitude.

Authors	locale	phase	method	component	time window	freq window	spectral est	reference	noise est
active source									
Wilcock et al. (1995)	East Pacific Rise	P	sr	V	0.7 sec	10 - 60 Hz	MT	x	ps
Clawson et al. (1989)	Yellowstone	P	sr	V	0.5 sec	2 - 16 Hz	ME	as	
passive source, multiphase									
Sheehan and Solomon (1992)	North Atlantic	S-SS	sr	SH	100 sec	.016 - .08, .095, .11	DFT .02 Hz	S	ps?
Flanagan and Wiens (1994)	West Pacific	sS-S,sScS-ScS	sr	SH	60 - 80 sec	0.01 - .083 Hz	DFT	S, ScS	ps
Roth et al. (1999)	Tonga-Fiji	P-P,S-P	sr	V,SH,SV	20 sec, 6 sec	.1 - 2 Hz, .75 - 3 Hz	DFT	P	ps
Bhattacharyya et al. (1996)	global	S-SS	si	SH	35 - 50 sec	3 est .02 - .1 Hz	MT	S	
Warren and Shearer (2000)	global	P-PP	sr	V	12.6 sec	.16 - .86 Hz	DFT	P	
Chan and Der (1988)	various	ScS mults	wf	SH	300 sec			ScS	ps?
Sipkin and Jordan (1980)	Japan, S America	ScS mults	ss	SH	180 sec	.006 - .056 Hz	DFT .01 Hz	ScS	ps
Ding and Grand (1993)	East Pacific Rise	S mults	wf	SH	800 sec			c	
Nakanishi (1979)	Japan	ScS mults	sr	SH	120 sec	.01-.04, .01-.1 Hz	DFT	ScS	ps
Lay and Wallace(1983,1988)	W N America	ScS mults	sr sm	SH	150 sec	.008-.04 Hz	DFT	ScS	ps
passive source, single phase									
Taylor et al. (1986)	N America	P, S	sr	V, SH,SV	30-40 sec	.05-1.0 Hz	DFT .11 Hz	s	ps
Halderman and Davis (1991)	Rio Grande & E Africa	P	cs	V	variable	.12 - 4.0 Hz	DFT .11 Hz	cs	ps?
Boyd, et al. (2004)	Sierra Nevada	S	sr	F-S		0.33 - 0.1 Hz		aa?	
Boyd and Sheehan (2005)	Rocky Mtns	S	sr	SH	200 sec	.02 - .1 Hz	MT	aa	ps
Allen et al. (1999)	Iceland	S	sr		50 - 80 sec	.03 - .175 Hz var	DFT .11 Hz	e	ps
Slack et al. (1996)	Rio Grande Rift	P,S	cs		26 sec			cs	ps?
Lees and Lindley (1994)	Loma Prieta	P,S	sm	V,SH	1-3,2.5-5 sec	2-60 Hz, 2-20 Hz	DFT	c	ps

There are two important sources of error in estimating the attenuation of teleseismic arrivals recorded by a seismic array. The first is ignorance of the incoming waveform, which complicates the calculation an absolute value for Q . The second is contamination by noise. This can be background or “random” energy unrelated to the signal including local anthropogenic noise, effects of wind, and microseisms generated by oceanic processes. Of more importance, especially in continental areas, is signal-generated noise, which is created by receiver-side lithospheric scattering, Rayleigh waves generated by interaction with structure and topography (Levander and Hill, 1985; Clouser and Langston, 1995), shear-wave splitting, basin reverberations, arrival of multiple teleseismic phases such as SKS, and focusing effects (Allen et al., 1999). In our investigation, we simulate most of these noise sources and investigate strategies to minimize their influence on t^* estimation.

2.2. Teleseismic t^* Estimation

Our goal in the estimation of t^* is threefold. The first is to minimize the effects of noise without adversely affecting the quality of the data, which we accomplish by selecting an appropriate frame of reference. The second is to obtain a number of t^* estimates using both time domain and frequency domain methods. And the third is to assess to some degree of accuracy the uncertainty associated with these estimates.

2.2.1. Frame of Reference

The most common means of reducing the effects of noise is to analyze the data in a frame of reference which most closely corresponds to the polarization direction of the

signal, thus maximizing the signal to noise ratio. Most studies choose the vertical component for P-waves, the radial component for SKS arrivals, and the transverse component for S-waves. Depending on source kinematics and back azimuth, however, particle motion for S-waves ranges from transverse to radial (Figure 2.1). Expanding on work by Montalbetti and Kansewich (1970) and Vidale (1986), we have developed a means of estimating the polarization direction of the signal.

The radial (ra), transverse (tr), and vertical (ve) S-wave components are converted to analytic traces using the Hilbert transform (H):

$$R(t) = ra(t) + i H[ra(t)] \quad (2.1a)$$

$$T(t) = tr(t) + i H[tr(t)] \quad (2.1b)$$

$$V(t) = ve(t) + i H[ve(t)] \quad (2.1c)$$

The complex covariance matrix $C(t)$ is then constructed as follows:

$$C(t) = \begin{matrix} R(t) R(t)^* & R(t) T(t)^* & R(t) V(t)^* \\ T(t) R(t)^* & T(t) T(t)^* & T(t) V(t)^* \\ V(t) R(t)^* & V(t) T(t)^* & V(t) V(t)^* \end{matrix} \quad (2.2)$$

where asterisks connote the complex conjugate.

Eigenanalysis on the real part of this matrix yields two non-zero eigenvalues (λ_1 as the larger) and their associated normalized eigenvectors. We search a portion of the trace containing the arrival for the point with the largest λ_1 and take the associated eigenvector as the estimate of polarization direction. Taking the dot product of this

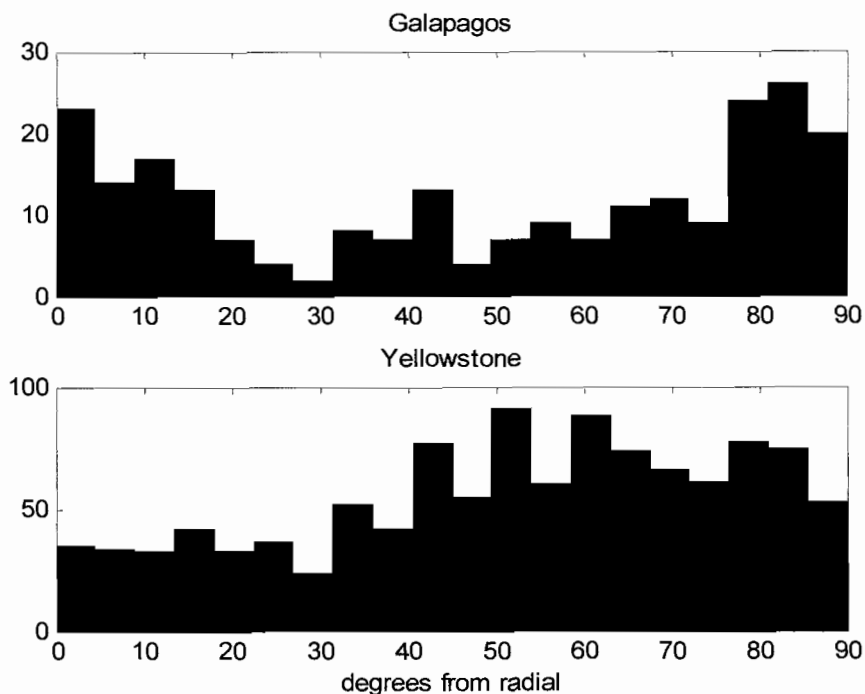


Figure 2.1. Histograms of S-wave polarization azimuths relative to raypath back azimuth for the Yellowstone and Galapagos arrays.

vector with the three components at each point rotates the data into this “polarized” frame of reference. In the interest of maintaining the integrity of the data, we have chosen not to perform any further manipulation or filtration of the time series which would tend to alter the observed waveforms.

Figure 2.2 shows the radial and transverse components for S-waves recorded at YISA stations from an event in Honshu, Japan, as well as IASP predicted arrival times. Figure 2.3 shows the data rotated into the polarized frame of reference and the estimated polarization directions in degrees from radial and degrees from horizontal.

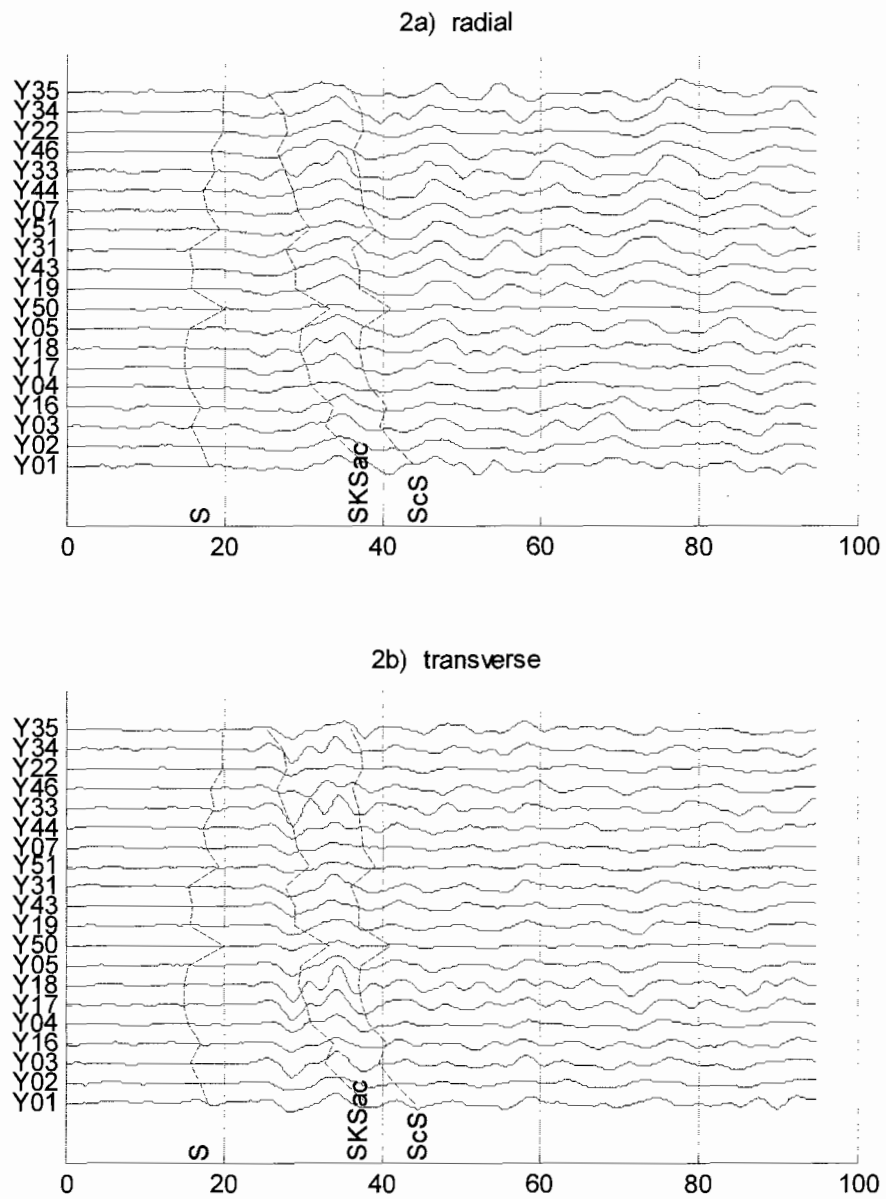


Figure 2.2. Radial (a) and transverse (b) components for S-waves recorded at YISA stations from an event in Honshu, Japan, with IASP-predicted S, SKS, and ScS arrival times.

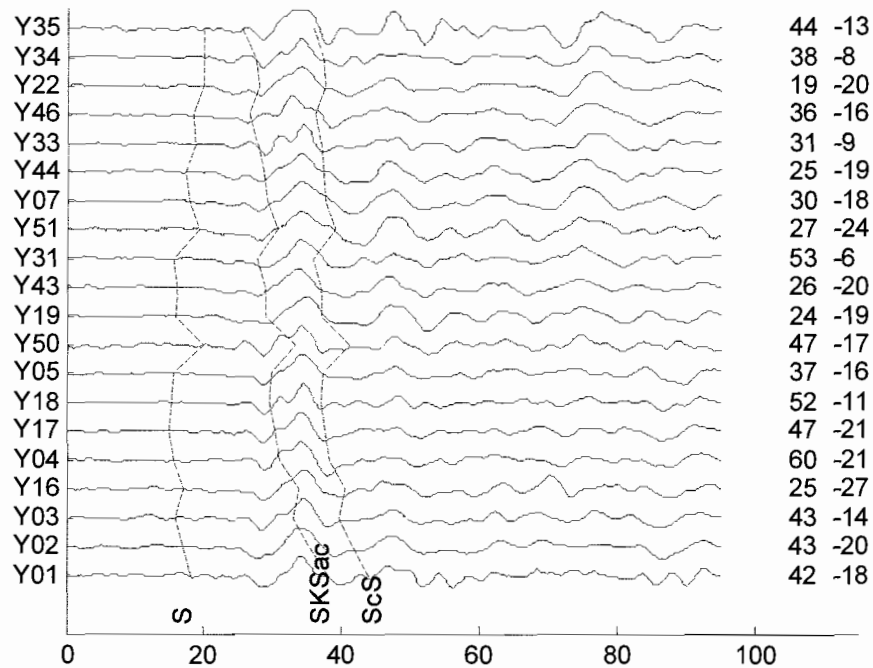


Figure 2.3. Data from Honshu event rotated into the “polarized” frame of reference. Listed are estimated polarization directions for each station in degrees from radial and degrees from horizontal.

2.2.2. Spectral Ratio Method

Usually t^* is determined in the frequency domain with the technique of spectral ratios (Teng, 1968). Combining (1.1) and (1.2) and using frequency $f = \omega/2\pi$,

$$t^* = x / Qc = -\log [A(f)/A_0(f)] / \pi f. \quad (2.3)$$

Analysis typically involves selecting a frequency range that provides the best signal-to-noise ratio, and then finding t^* as the best scaling of $-\pi f$ to produce the log amplitude ratio ($\log[A/A_0]$) within the chosen interval, usually by line-fitting using least squares.

Determining the appropriate frequency interval is not trivial, as windowing to avoid noise can easily lead to loss of attenuation information. Interval selection is most commonly accomplished by comparison with a noise spectrum derived from the pre-arrival portion of the trace (see Table 2.1), which is used to construct a filter to remove frequencies for which the signal to noise ratio does not meet some desired value. Where signal generated noise is important, this approach is clearly inappropriate. Figure 2.4a displays the normalized amplitude spectra and averaged reference spectrum for the traces in Figure 2.3. Figure 2.4b shows the standard deviation of amplitudes at each frequency for this set of signals. For purposes of display, a line is fit to this spectrum which arbitrarily delimits frequency ranges with greater or lesser variance. Areas of greater standard deviation may reflect either the effects of attenuation or of noise. For Yellowstone and Galapagos events (Figure 2.5), plots of these higher variance regions indicate that information (either noise or attenuation) is present at most frequencies from 0 to .5 Hz with slight gaps near .08 and .36 Hz. We have chosen to test our SR method using a five different frequency intervals each with a lower cutoff at .03 Hz and upper cutoffs at .1, .14, .18, .22, and .26 Hz. These will be treated as separate independent t^* estimates. Figure 2.6 displays, for the five different frequency ranges, the results of least squares line-fitting to a representative log amplitude ratio plot along with the resulting t^* estimates.

Estimation of the spectra can in itself be a source of error. The discrete Fourier transform (DFT) yields spectra that are not smooth, which complicates line fitting to spectral ratio plots. One solution is to apply a smoothing window or running average, but

as noted by Press et al. (1992), applying such techniques to non-monotonous sequences tends to introduce significant bias. Use of the DFT can also allow energy to leak to

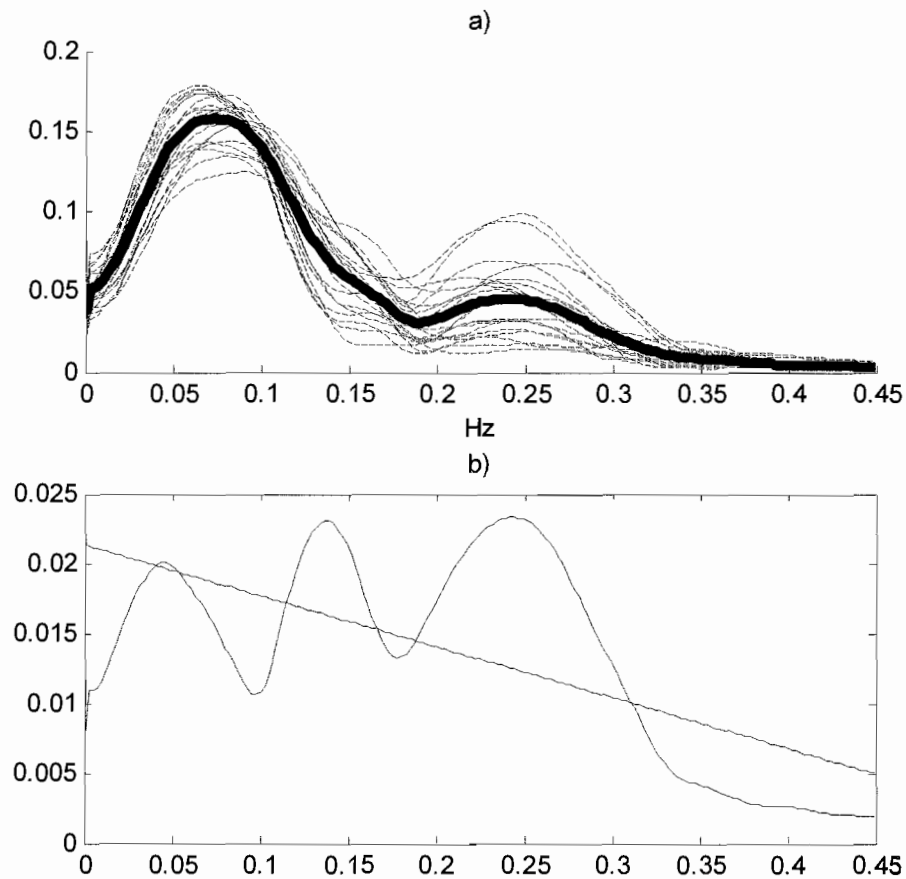


Figure 2.4. a) Normalized amplitude spectra (dashed) for the signals shown in Figure 2.3 using the multitaper method of spectral estimation. The average of these spectra (solid) is used as the reference spectrum for t^* estimation. b) Standard deviation of amplitudes at each frequency for this set of signals with a line fit by least squares.

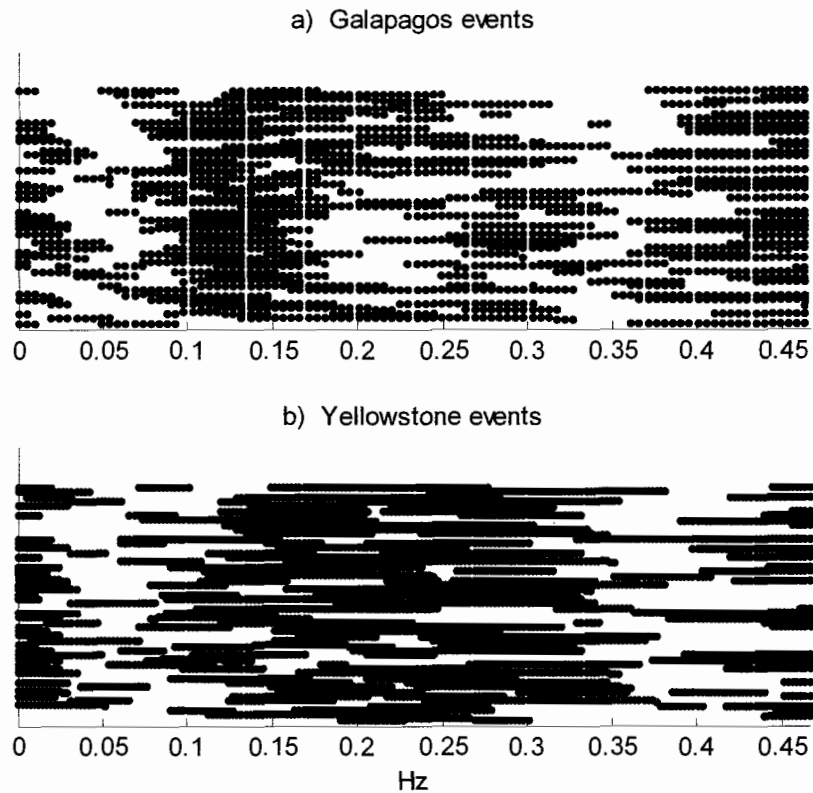


Figure 2.5. Regions of greater relative standard deviation (exceeding the least squares line in Figure 2.4b) versus frequency for a) 54 Galapagos events and b) 51 Yellowstone events.

higher frequencies. This problem can, to a great extent, be addressed by using multitaper spectral analysis (Thomson, 1982; Park et al., 1987; Lees and Park, 1994), and the resulting spectra are considerably smoother than those derived by DFT.

The use of spectral ratios may tend to cancel out the effects of energy leakage and thereby the advantage to using the multitaper method (MTM). Accordingly, we test the effects of using DFT, both smoothed and unsmoothed, and MTM with varying number of tapers. Prior to spectrum estimation, a 2-second cosine taper is applied 8 seconds prior to

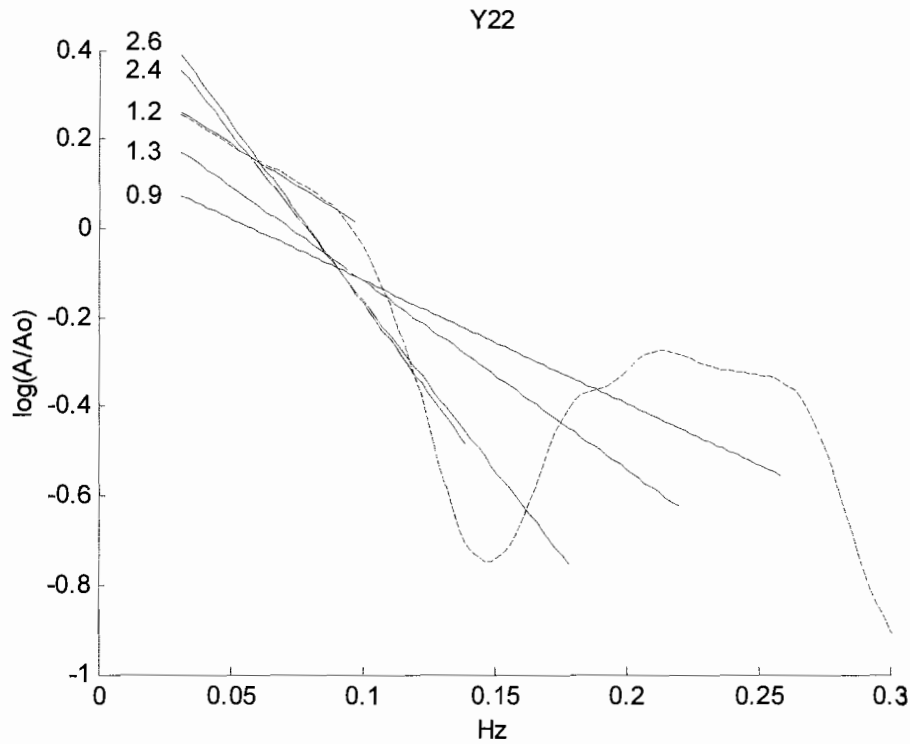


Figure 2.6. $\log(A/A_0)$ for Station Y22 versus frequency and lines fit by least squares over 5 different frequency ranges. For each line the t^* estimate derived from its slope is listed in seconds.

the main arrival peak to remove the pre-signal, and an exponential time taper, in the form $.9^t$ (t is seconds after start of taper) is applied starting 8 seconds after the arrival peak. This serves to damp post signal energy while still allowing the sampling of lower frequencies.

For each frequency interval we normalize individual spectra by their L2 norms and take the mean as the reference spectrum for that interval, which is then also

normalized by its L2 norm. This reference spectrum is equivalent to the “pseudosource” of Boyd and Sheehan (2005) and the “common spectrum” of Halderman and Davis (1991).

2.2.3. Waveform Modeling Method

A series of 100 attenuation operators is created, each taking the following form in the frequency domain:

$$P(\omega) = \exp [- \omega x S(\omega) / 2 Q(\omega) + i \omega D(\omega)] , \quad (2.4)$$

where $D(\omega)$ is slowness due to dispersion and $S(\omega)$ is total slowness and

$$S(\omega) = D(\omega) + 1/V_u , \quad (2.5)$$

where V_u is the unattenuated seismic velocity, specified here at 5 km/s for S-waves (8.5 km/s for P-waves), and we specify the distance traveled through the attenuating medium (x) at 200 km. Values for $1/Q(\omega)$ are acquired by superposition of ~ 70 Debye peaks.

Each peak is constructed following the equations of Aki and Richards (2002):

$$1/Q(\omega) = \omega (\tau_e - \tau_s) / (1 + \omega^2 \tau_e \tau_s) , \quad (2.5)$$

where τ_e is the characteristic relaxation time of strain for a step change in stress and τ_s is that of stress for a step change in strain. Values for $D(\omega)$ are obtained in similar fashion:

$$D(\omega) = (\sqrt{[(\tau_e / \tau_s - 1) / (1 + \omega^2 \tau_e \tau_s)]}) / V_u . \quad (2.7)$$

For each operator and each peak, the relaxation times are obtained as follows:

$$\tau_e(Q_D, \omega_D) = [s b / Q_D + \sqrt{(s^2 b^2 / Q_D^2) + 1}] / \omega_D \quad \text{and} \quad (2.8)$$

$$\tau_s(Q_D, \omega_D) = 1 / \tau_e \omega_D^2 , \quad (2.9)$$

where Q_D is the minimum Q for a given operator (i.e. maximum attenuation), ω_D is the angular frequency where the minimum Q occurs for a given Debye peak, s scales the relaxation times such that after superposition the minimum Q equals Q_D , and $b = \omega_D^\beta$. For these tests, we have chosen to set $\beta = 0$, i.e. frequency-independent Q .

The Debye frequencies ω_D range from 10^{-5} to 100 hertz (times 2π) and are assumed to be within any postulated “absorption band” for the Earth (e.g. Anderson and Given, 1982). The values of Q_D chosen for the operators range from 5 to 1000 but are spaced so as to produce evenly spaced values of t^* (or $1/Q$) rather than of Q . We deconvolve the 100 operators by a selected operator so as to produce a set of operators that primarily attenuate but also deattenuate.

The windows for this method are between 12 and 28 seconds in length commencing between 3 and 7 seconds before arrival with 2-second cosine tapers at either end (Figure 2.7). For each window the traces are normalized by their L2 norms and aligned by cross-correlation. The ratios of these L2 norms to the L2 norms of the full (3-component) windowed signals are used to produce a weighted average of these traces yielding the reference trace for this window. A lowpass filter is applied to this reference trace so as to reduce energy above .3 Hz. The reference trace is then convolved with the set of attenuation operators to produce a set of 100 traces, which are then re-normalized by their L2 norms (Figure 2.8). From this set, a match for each windowed trace is found by cross-correlation (Figure 2.9). Even if Q is taken to be independent of frequency, the

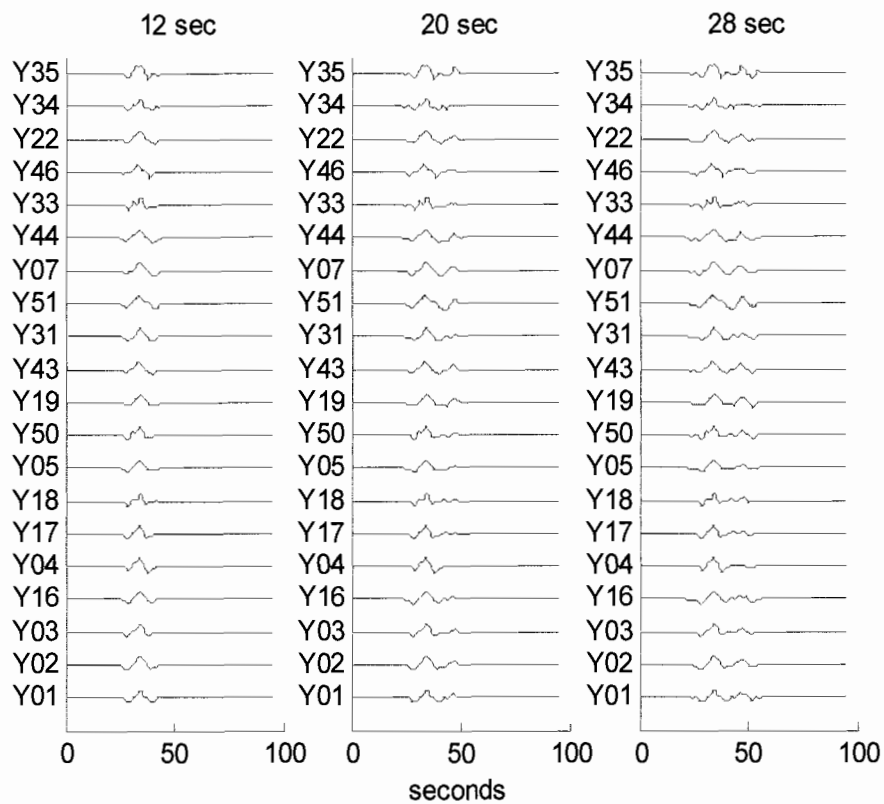


Figure 2.7. Example of windowing for the WF method showing application of 12, 20, and 28 second windows to polarized traces from the Honshu event.

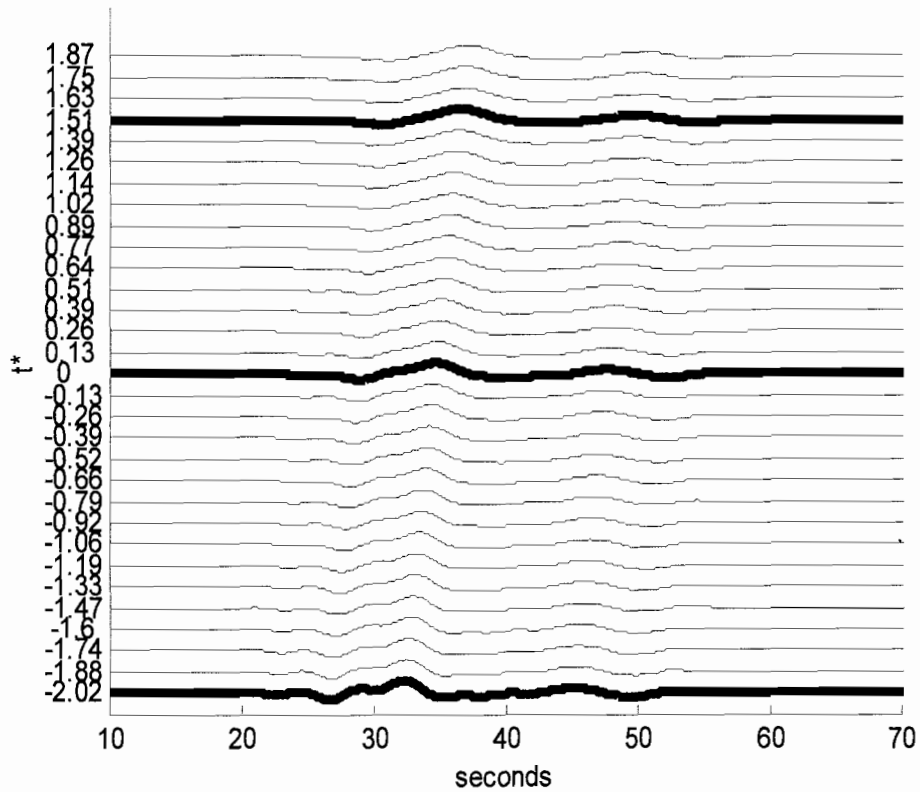


Figure 2.8. Example of synthetically attenuated and de-attenuated traces based on the reference trace ($t^* = 0$). In bold are the matches found by cross-correlation for data from the Honshu event shown in Figure 2.9.

effects of dispersion cause the t^* value associated with the match to be frequency

dependent, and a “dominant” frequency for the signal must be specified. We use .16 Hz

for S-waves (for P-waves we would use .3 Hz), which yields an operator t^* range of -3.5

to +7.5 seconds.

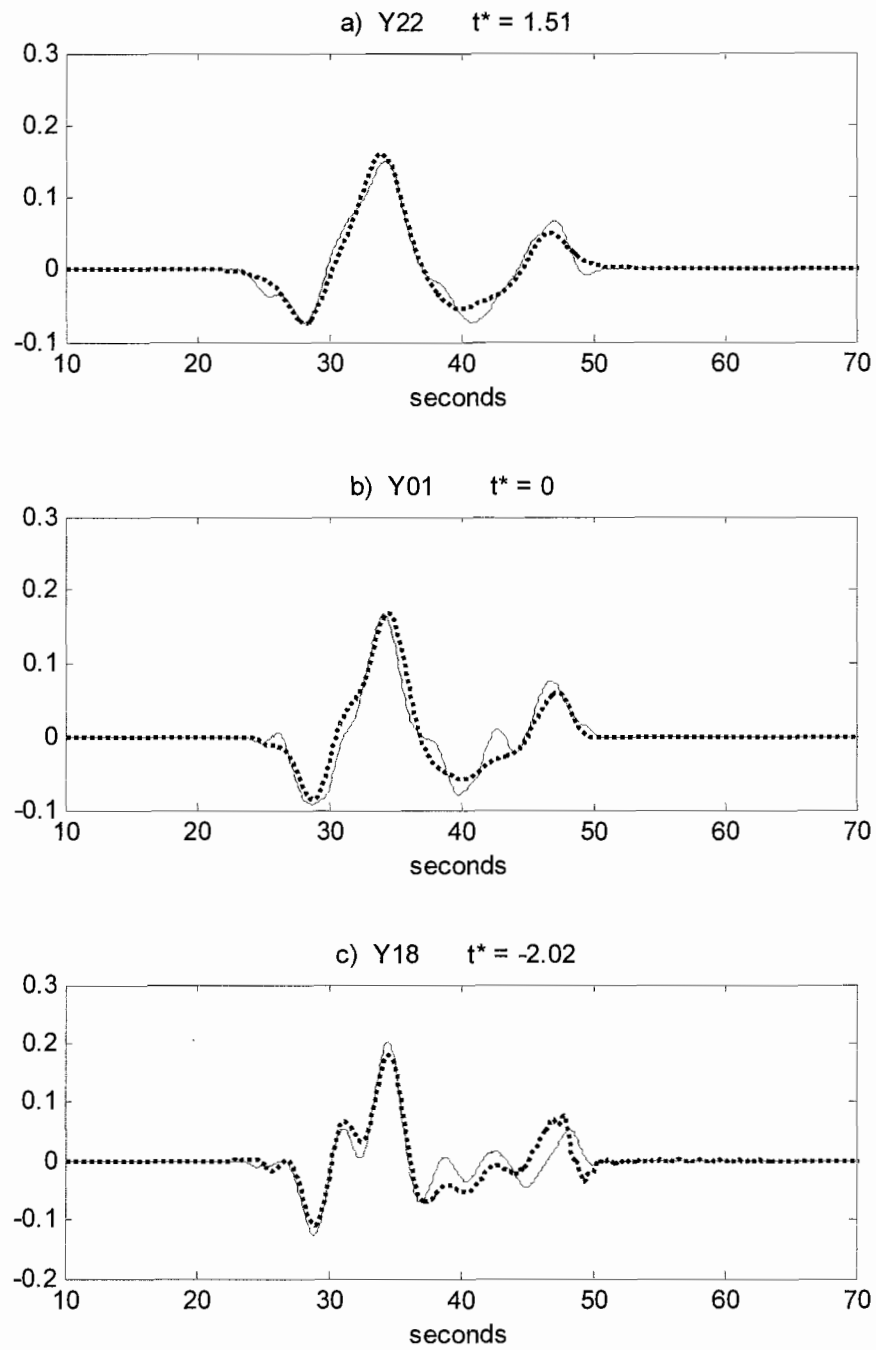


Figure 2.9. Selected polarized traces from the Honshu event (solid) and matching synthetic traces (dotted), also shown in Figure 2.8.

2.2.4. Measures of Uncertainty

Many techniques have been developed to assess the uncertainty associated with a t^* estimate, including trace appearance (Sheehan and Solomon, 1992), scatter of t^* estimates for similar raypaths (Flanagan and Wiens, 1994), spectral ratio variance (Bhattacharyya et al., 1996; Gomer and Okal, 2003), Q response to the addition of random t^* error (Ward and Young, 1980), and t^* response to the addition of random noise (Boyd and Sheehan, 2005).

We employ a measure of the misfit of the observed spectrum or trace with that predicted by the t^* estimate operating on the reference spectrum or trace in the form of the estimated standard error,

$$E = \text{sqrt} [\sum [(A_{\text{obs}}(f \text{ or } t) - A_{\text{pred}}(f \text{ or } t))^2] / (n - 1)], \quad (2.10)$$

where n is the number of points sampled. Clawson et al. (1989), Roth et al. (1999), and Allen et al. (1999) take this approach with line fitting to the log spectral ratio. Dorman (1968, 1969) recommends this “logarithmic transformation” as it makes such metrics independent of absolute amplitude. As we wish to compare and possibly combine the estimates for both frequency and time domains and taking the logarithm of the latter being impossible, we employ the non-logarithmic form and rely on normalizing both observed and reference traces or spectra after windowing to minimize amplitude or gain effects.

Our goal for real data is to derive from these misfit values some measure of estimate error or uncertainty. In the synthetic noise tests, we can obtain values for both

misfit and error and thus examine the correlation between them. As there is reason to assume that these relationships may differ between various methods and window sizes, we compute them separately for the five different SR and five different WF forms of t^* estimation.

2.3. Synthetic Noise Tests

These tests represent 880,000 individual t^* estimates. We use 10 different input signals to produce synthetic traces reflecting the addition of 5 types of signal-generated noise: lithospheric scattering, shear wave splitting, Rayleigh wave arrival, basin reverberation, and arrival of SKS and ScS phases. For each type of noise we use 10 different values for parameters particular to that form of noise. We use 44 different S-wave polarization azimuths ranging from 2 to 88 degrees from raypath back azimuth. We use 3 different frames of reference: the radial (SV), transverse (SH), and that of the estimated polarization direction (PL). We employ the multitaper method for spectral estimation on the 3 frames of reference. For the PL frame of reference, we also use the DFT, both unsmoothed and smoothed using a smoothing window 11Hz in width. To these we apply SR and WF methods using 5 window lengths each, and the input signal is used as the reference signal.

2.3.1. Noise Simulation

2.3.1.1. Lithospheric Scattering

We model the effects of lithospheric scattering by convolving the input signal with a randomly constructed synthetic receiver function, in other words, the superposition of 50 copies of the input signal with varying arrival times, amplitudes, and polarization directions. This does not simulate scattering that modifies the waveform itself such as thin layer scattering with intrabed multiples (e.g. Richards and Menke, 1983; Schoenberger and Levin, 1974) or scattering by small bodies (Aki and Richards, 2002). The noise is then scaled to 20% of the original signal energy and added to the signal.

2.3.1.2. Rayleigh Waves

For Rayleigh waves we first solve the Rayleigh function for the Rayleigh wave slowness, using $V_s = 3.2$ km/sec and $V_p = 5.8$ km/sec. We then compute the P-wave and SV-wave displacements. For each displacement we sum over the positive frequencies up to the Nyquist and combine P and S-wave motions to yield the horizontal and vertical Rayleigh wave components. Since we are varying the synthetic S-wave polarization direction, we can arbitrarily assign the Rayleigh wave back azimuth as 30° from raypath back azimuth. We rotate the horizontal component of the Rayleigh wave to this back azimuth, time shift to a given delay, scale to 20% of total input signal energy, and add to the S-wave.

2.3.1.3. Shear Wave Splitting

We simulate the effects of shear wave splitting by rotating the S-wave reference frame into the specified fast direction. Here the slow direction component is shifted by a specified split time, and the signal is rotated back to the radial direction. The vertical component remains unchanged.

2.3.1.4. Basin Reverberation

We model the first four reverberations of the input signal produced by a single layer over a half space, using a reflection coefficient of .3 at the lower interface. We assume the coefficient at the free surface to be one. The echo is then time-shifted according to a specified velocity ($V_s = 3.1$ km/sec) and layer thickness (up to 30 km), reversed 180° in polarity, and added to the S-wave.

2.3.1.5. SKS and ScS Arrivals

For a given S-wave polarization direction and ray parameter (using an event depth of 30 km) we solve for the coefficients for S-wave reflection (ScS) and S-wave to P-wave transmission followed by P-wave to S-wave transmission (SKS) at the core-mantle boundary. To calculate core interactions, we employ the displacement expressions of Aki and Richards (2002, table 5.1) and assume continuity of vertical displacement and traction and horizontal traction to be zero. These phases are scaled accordingly and added to the original S-wave.

2.4. Results

For the various types of noise and methods of t^* estimation, we examine values for estimate misfit and for error (here defined as absolute t^* error). We wish not only to test the relative efficacy of various techniques but also to determine whether misfit values are an accurate reflection of estimate error and can be used to derive values for estimate uncertainty in real data.

2.4.1. Absolute t^* Error

Figure 2.10 shows representative MTM spectral ratio results for SH, SV, and PL traces with lithospheric scattering. While the results vary significantly with different input signals and lengths of the frequency window, a consistent pattern emerges which persists for all methods and type of noise. As the SV or SH polarization azimuth increasingly diverges from the actual polarization direction, the trace increasingly samples noise rather than signal, and t^* error increases.

Figures 2.11 and 2.12 plot error versus noise parameter for the various types of noise (excluding lithospheric scattering) for different frames of reference and window lengths, respectively. Figure 2.13 plots error versus window length for different frames of reference including the use of smoothed and unsmoothed DFT on the PL frame. In all these figures, error values for the WF method are consistently higher than for the SR method.

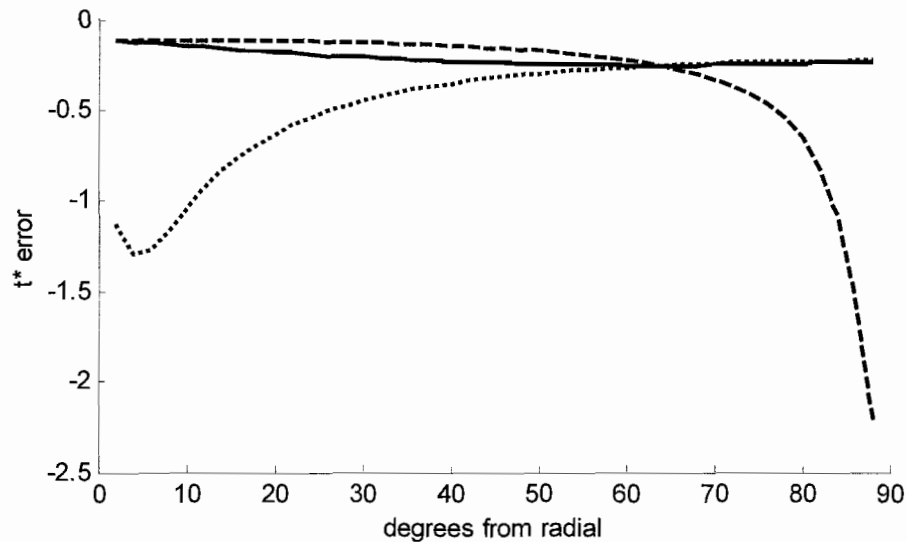


Figure 2.10. t^* error, in seconds, due to addition of synthetic lithospheric scattering noise, representing spectral ratio (SR) results using an upper frequency cutoff of .26 Hz. versus S-wave polarization in degrees from raypath azimuth, or radial. Shown are the results using the SV component (dashed), the SH component (dotted), and the PL component (solid).

In Figure 2.11, the PL frame of reference for Rayleigh waves yields lower error than do SV or SH components. The arbitrary setting of Rayleigh wave azimuth to 30° from radial is responsible for the observed greater error values for SV compared to SH. Error values for basin reverberation are higher than for Rayleigh waves but display little difference due to either method or frame of reference.

SKS and ScS arrivals cause the largest t^* errors, peaking at distances of 84° and 90° , respectively. The WF method appears to be more sensitive to ScS than SKS arrivals. The SV frame of reference is affected most by SKS and least by ScS, while the

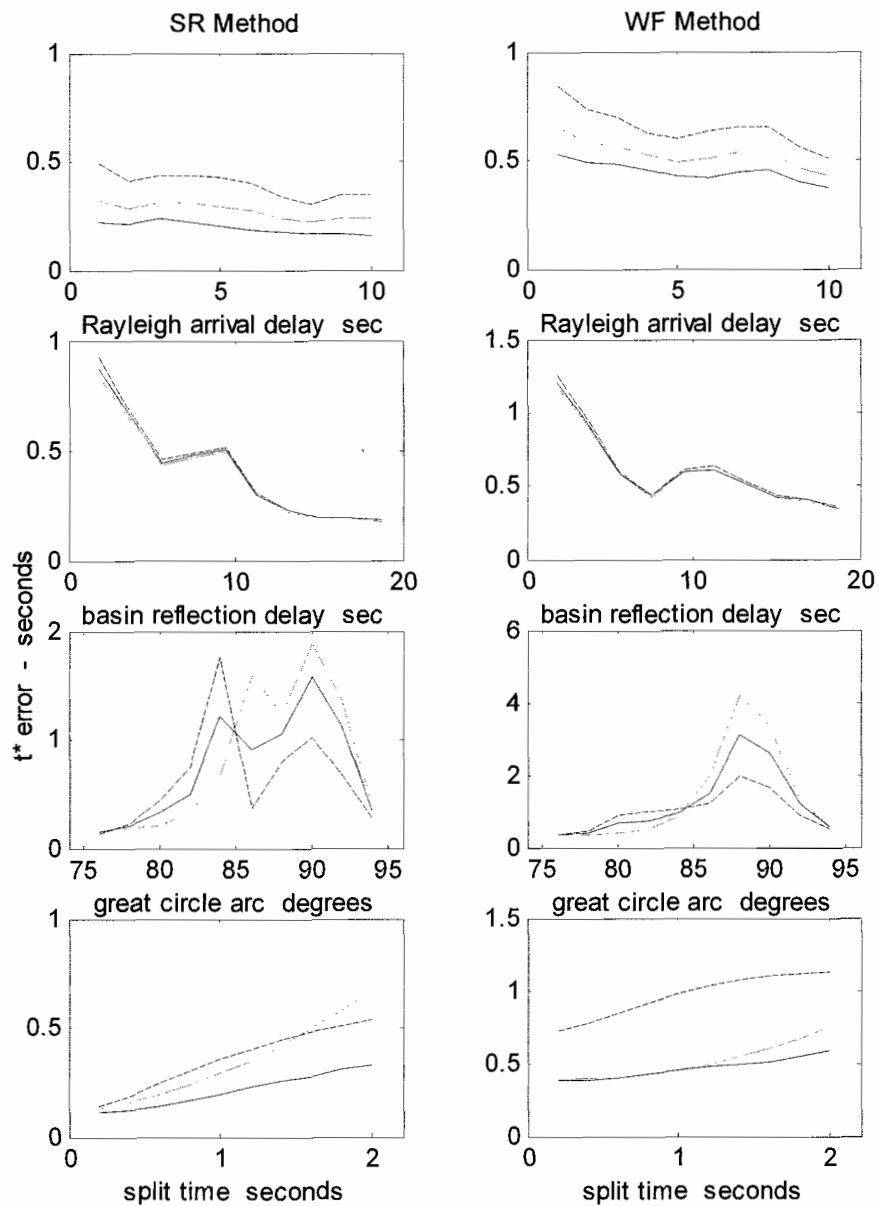


Figure 2.11. Absolute t^* error, in seconds, due to addition of synthetic noise for SR and WF methods versus noise parameter, representing the average of 2200 tests. Shown are the results for Rayleigh wave arrival versus arrival delay in seconds, for basin reverberation versus first reflection arrival delay in seconds, for SKS and ScS arrivals versus great circle arc distance in degrees, and for shear-wave splitting versus split time in seconds. The components are marked as in Figure 2.10.

opposite is the case for the SH component. For the PL frame of reference the results are intermediate.

Error for shear wave splitting is comparable to that for Rayleigh waves and tends to peak at 2.5 to 3 seconds. In regions of strong anisotropy, some have suggested such rotating the data to align with the fast and slow directions (Boyd et al., 2004). Rather than align SV and SH exactly with the fast and slow directions, we have shifted them 10° . This shift serves to test the effects of secular variation of fast direction on such techniques. The resulting error values are higher than for the PL frame of reference, although the SH (slow) component appears less affected when the WF method is employed.

Figure 2.12 displays the same results averaged over the frames of reference and with the window lengths plotted separately. The results for the WF method appear essentially insensitive to window length, whereas those for the SR method, with the exception of shear wave splitting, are strongly affected. As the frequency windows are lengthened to include higher frequencies, the error peaks for both Rayleigh waves and basin reverberation shift toward shorter delay times. This feature was noted by Boyd and Sheehan (2005) in regard to the calculation of their basin correction for t^* , i.e. that the corrections must differ for different frequency ranges. For SKS and ScS arrivals, longer frequency windows decrease sensitivity to SKS and shift the ScS peak toward greater distances.

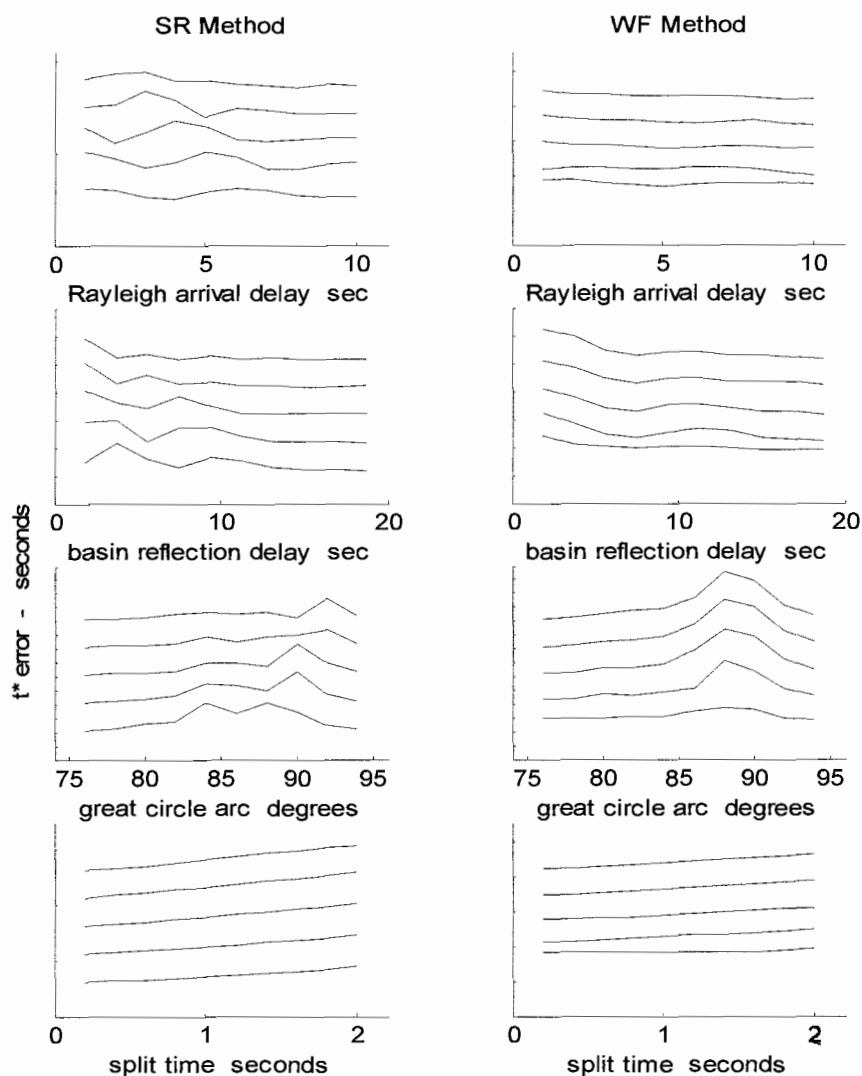


Figure 2.12. Absolute t^* error, in seconds, due to addition of synthetic noise for SR and WF methods versus noise parameter for each window length, representing the average of PL, SH, and SV components (1320 tests). Shown are the results for Rayleigh wave arrival versus arrival delay in seconds, for basin reverberation versus first reflection arrival delay in seconds, for SKS and ScS arrivals versus great circle arc distance in degrees, and for shear-wave splitting versus split time in seconds. In each plot from bottom to top for the SR method, the lines represent results for upper frequency cutoffs of .1, .14, .18, .22, and .26 Hz. Similarly for the WF method, the lines represent results for window widths of 12, 16, 20, 24, and 28 seconds. Spacing for y-axis tick marks is 1 second.

Figure 2.13 plots error versus window length. For the WF method, these are inversely correlated except in the case of SKS-ScS arrivals. For the SR method, the correlation is inverse for basin reverberation and SKS-ScS arrivals, slightly positive for shear wave splitting, and essentially absent for lithospheric scattering and Rayleigh waves. Also displayed are results using DFT applied to the PL component, both with and without smoothing. The unsmoothed DFT results consistently show considerable error for the shortest windows. This tendency has been noted by both Ward and Young (1980) and Taylor et al. (1986). For the other window lengths, however, the unsmoothed DFT consistently outperforms the multitaper method. Multitaper results shown here represent the use of 7 Slepian tapers. When we have conducted lithospheric scattering tests with down to 3 tapers, the results vary considerably based on frequency content of the input signal. On average, however, the use of 7 tapers yields less error than the use of fewer tapers and slightly more error than the unsmoothed DFT.

Use of a smoothing technique would appear to yield even less error, but these results are misleading, as an inherent tendency of smoothing is to erase distinctive spectral features. When the actual t^* value is non-zero and the width of the smoothing window approaches that used for line-fitting, we have found that the absolute value of t^* can be underestimated by over 70%.

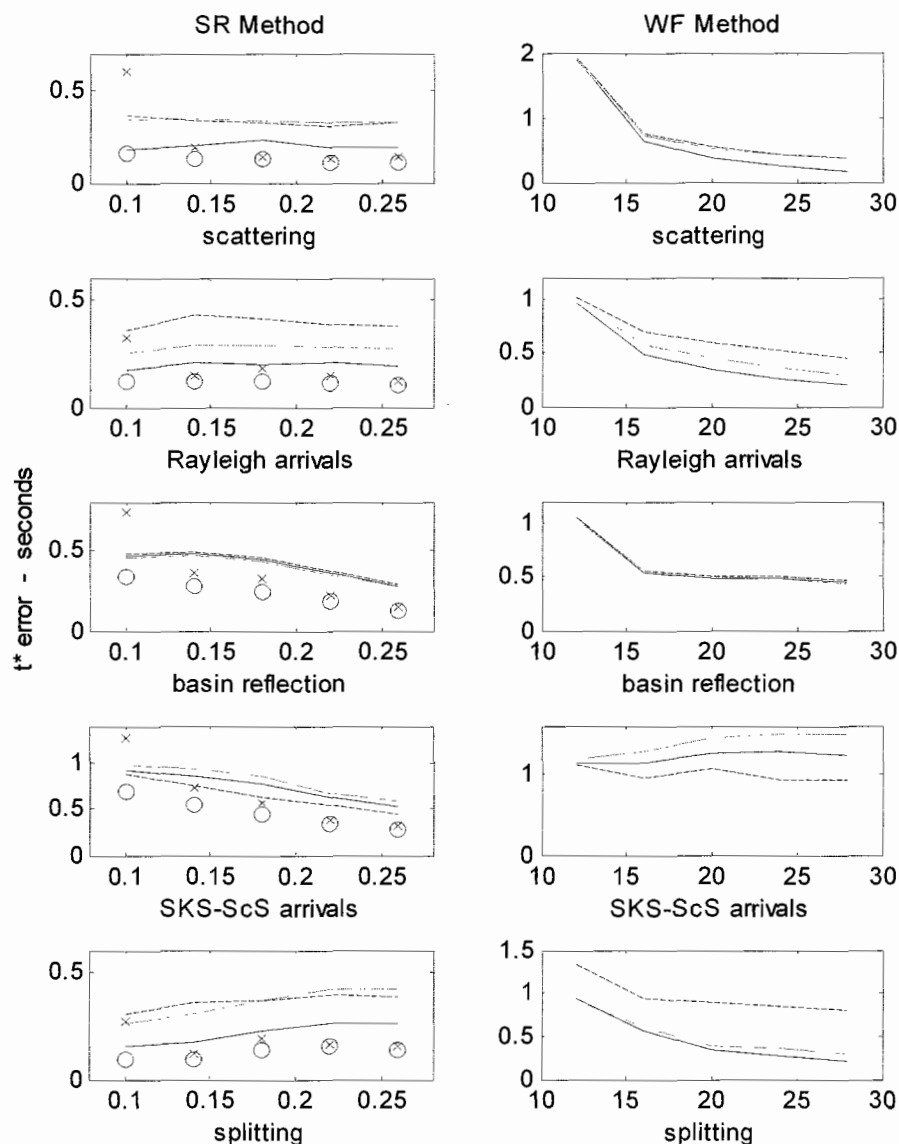


Figure 2.13. Absolute t^* error in seconds, due to addition of synthetic noise for SR and WF methods versus window size (upper cutoff in Hz for SR and window length in seconds for WF), representing the average of 4400 tests. Shown are the results for lithospheric scattering, Rayleigh wave arrival, basin reverberation, SKS and ScS arrivals, and shear-wave splitting. The components are marked as in Figure 2.10. Also shown are the results for the PL component using a DFT with no smoothing (x's) and moving average window .11 Hz in width (o's).

2.4.2. Estimate Misfit

Estimate misfit values for the various forms of noise are shown as a function of window size in Figure 2.14. Comparing these misfit trends to the error trends shown in Figure 2.13 clearly indicates the relationship between misfit and error varies with method and window size. In particular, short windows in the spectral ratio method are characterized by high error but low misfit values. This is most likely a result of the greater relative smoothness of shorter, often monotonous spectral segments. Normalization of these segments and the corresponding segments of the reference spectrum can lead to very low misfit values. Such is not the case in the time domain, where shorter trace segments are never monotonous.

2.4.3. Results with Variable Actual t^*

The synthetic results presented so far differ from real data in one important respect. They represent apparent attenuation due to noise for one station with no actual attenuation. Real data comprises t^* estimates for several stations with varying amounts of actual attenuation. To represent results for an array we apply our attenuation operators to an input signal to generate 20 traces with t^* values ranging from -2.5 to +2.5 seconds. For each of these stations, we randomly generate lithospheric scattering, using a signal-to-noise ratio of 2:1, and basin reverberation, with a basin reflection coefficient of .3. We use 48 different input signals (i.e. events), thus the data resembles a typical teleseismic dataset. We test the WF method and the SR method using both MTM and unsmoothed

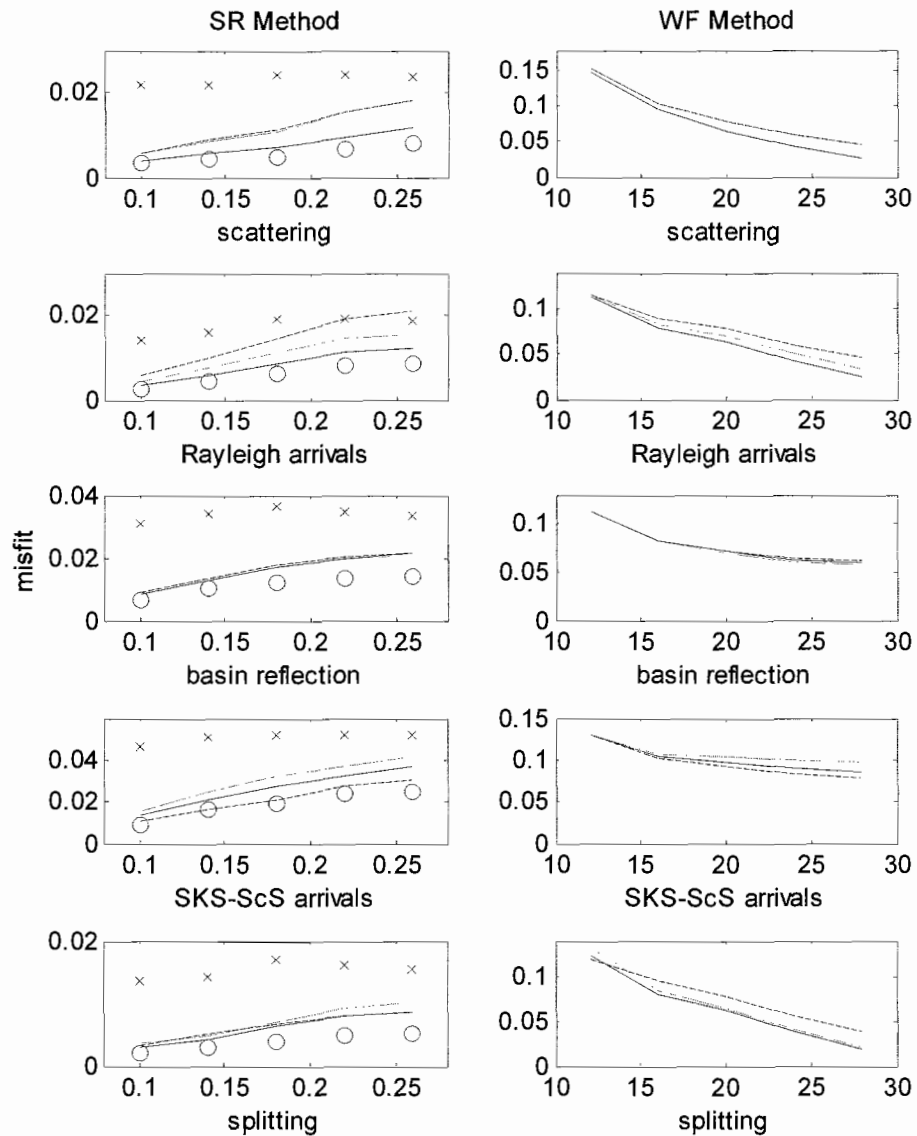


Figure 2.14. Estimate misfit due to addition of synthetic noise for SR and WF methods versus window length (upper cutoff in Hz for SR and window length in seconds for WF), representing the average of 4400 tests. Shown are the results for lithospheric scattering, Rayleigh wave arrival, basin reverberation, SKS and ScS arrivals, and shear-wave splitting. The components are marked as in Figure 2.13.

DFT means of spectral estimation. For these methods we also examine the effects of using an averaged trace versus the actual input signal as reference.

Table 2.2 lists mean misfit, mean absolute t^* error, and mean absolute t^* for various window widths for our synthetic datasets. In all cases, the use of an averaged reference signal yields lower error, misfit and absolute t^* than does the use of the actual input signal. Due to greater spectral smoothness, the multitaper method produces consistently lower misfit values than does the DFT. For the DFT estimates, mean error decreases rapidly with the use of higher frequency cutoffs; while for the MTM estimates, error tends to decrease more slowly. With the use of longer time windows, error for the WF method also decreases slightly. Mean absolute t^* values show a similar trend for the DFT estimates but not for the MTM and WF methods. Mean misfit values increase with frequency cutoff for MTM estimates, show no trend with DFT estimates, and decrease with increasing time window for the WF method.

Table 2.3 lists linear regression results for our synthetic array for absolute t^* error against estimate misfit, absolute t^* against estimate misfit and absolute t^* against absolute t^* error. While only one of the coefficients of determination (R^2) exceeds 0.5, all the regressions yield F tests which reject the null hypothesis due to the large number of samples ($n = 960$). The greatest correlation appears to be between absolute t^* and absolute t^* error, particularly for MTM estimates and DFT estimates using shorter frequency ranges. This correlation reflects the association of extreme error and outlier t^* values and the general effect that as absolute t^* increases the observed signal decreasingly resembles the reference signal, which tends to increase the likelihood of

Table 2.2. Mean error, mean absolute t^* , and mean misfit for 5 different synthetic datasets for the SR method, using DFT and MTM, and the WF method. Both the original input signal and an averaged signal were used as reference. Results are listed for frequency ranges with different upper cutoffs (SR) and time windows of different lengths (WF).

absolute t^* error		.1 Hz	.14 Hz	.18 Hz	.22 Hz	.26 Hz
DFT	input	2.16	1.40	1.09	0.91	0.85
	average	2.03	1.28	0.96	0.80	0.73
MTM	input	2.11	2.29	2.33	2.34	2.31
	average	1.58	1.53	1.41	1.29	1.21
WF		12 sec	16 sec	20 sec	24 sec	28 sec
	input	0.91	0.87	0.84	0.74	0.71
	average	0.81	0.82	0.78	0.72	0.69
mean absolute t^*		.1 Hz	.14 Hz	.18 Hz	.22 Hz	.26 Hz
DFT	input	2.36	1.74	1.51	1.34	1.28
	average	2.23	1.60	1.36	1.20	1.08
MTM	input	2.30	2.70	2.84	2.87	2.78
	average	1.86	2.07	2.09	2.03	1.93
WF		12 sec	16 sec	20 sec	24 sec	28 sec
	input	1.27	1.31	1.33	1.24	1.26
	average	1.12	1.23	1.23	1.18	1.22
mean misfit		.1 Hz	.14 Hz	.18 Hz	.22 Hz	.26 Hz
DFT	input	0.021	0.023	0.023	0.022	0.021
	average	0.019	0.022	0.021	0.020	0.019
MTM	input	0.011	0.019	0.023	0.024	0.025
	average	0.008	0.012	0.015	0.016	0.017
WF		12 sec	16 sec	20 sec	24 sec	28 sec
	input	0.025	0.024	0.023	0.021	0.019
	average	0.024	0.022	0.021	0.019	0.018

Table 2.3. An average of linear regression results for 5 different synthetic datasets. Slope and coefficient of determination (R^2) are listed for regressions of error versus misfit, absolute t^* versus misfit, and absolute t^* versus error for the SR method, using DFT and MTM, and the WF method with an averaged reference signal. Results are listed for frequency ranges with different upper cutoffs (SR) and time windows of different lengths (WF).

absolute t^* error vs misfit		.1 Hz	.14 Hz	.18 Hz	.22 Hz	.26 Hz
DFT	slope	28.49	16.86	13.23	13.34	13.95
average	R2	0.087	0.054	0.038	0.041	0.044
MTM						
	slope	67.26	54.78	50.23	40.41	30.95
average	R2	0.108	0.137	0.166	0.133	0.084
WF		12 sec	16 sec	20 sec	24 sec	28 sec
	slope	21.06	25.17	24.45	13.61	1.75
	R2	0.149	0.143	0.116	0.024	0.003
absolute t^* vs misfit		.1 Hz	.14 Hz	.18 Hz	.22 Hz	.26 Hz
DFT	slope	26.63	11.50	4.98	-1.57	-7.15
	R2	0.059	0.018	0.004	0.001	0.007
MTM						
	slope	91.31	79.03	70.96	58.57	45.99
	R2	0.143	0.165	0.173	0.132	0.084
WF		12 sec	16 sec	20 sec	24 sec	28 sec
	slope	9.40	11.25	3.40	-13.86	-15.89
	R2	0.036	0.043	0.013	0.018	0.008
absolute t^* vs absolute error		.1 Hz	.14 Hz	.18 Hz	.22 Hz	.26 Hz
DFT	slope	0.80	0.58	0.28	0.09	-0.07
	R2	0.535	0.213	0.048	0.006	0.007
MTM						
	slope	0.77	0.87	0.92	0.93	0.88
	R2	0.424	0.433	0.450	0.415	0.369
WF		12 sec	16 sec	20 sec	24 sec	28 sec
	slope	0.20	0.32	0.25	0.16	0.21
	R2	0.072	0.135	0.091	0.027	0.029

estimate error. Regressions against misfit have much lower R^2 values, but all methods show a decrease with increasing window width and are generally higher for MTM estimates.

These results suggest that for the spectral ratio methods, estimate misfit correlates with estimate error only when the error is relatively large. This correlation is probably fairly dependable but can only be detected where the set of estimates contains a larger number of error-related outliers, e.g. DFT estimates with short frequency windows and MTM estimates in general. The relatively limited range of t^* operators used in the WF method tend to preclude the generation of extreme t^* estimates, thus the lack of correlation of t^* with error and misfit. The slight correlation between error and misfit suggests that, for the WF method, errors are still large enough to cause proportionally large misfits.

2.4.4. Applicability to Real Data Sets

For real datasets from Yellowstone and the Galapagos, mean misfit, mean absolute t^* , and the results of regressions between misfit and absolute t^* are listed in Table 2.4. The trends and magnitudes of these statistics are similar to those for the synthetic datasets, except for the absolute t^* values for the MTM estimates, which are much lower, and the R^2 values for all the regressions, which are significantly higher.

For the synthetic noise tests, mean misfit, mean absolute t^* error, and regression results are shown in Table 2.5. Compared to the synthetic dataset results, the DFT and MTM methods yield much lower misfit and error values; while those for the WF method

Table 2.4. Mean absolute t^* and mean misfit for the Yellowstone and Galapagos datasets for the SR method, using DFT and MTM, and the WF method. Averaged signals were used as reference. Results are listed for frequency ranges with different upper cutoffs (SR) and time windows of different lengths (WF).

Yellowstone		.1 Hz	.14 Hz	.18 Hz	.22 Hz	.26 Hz
DFT	mean absolute t^*	2.03	1.55	1.21	1.00	0.87
	mean misfit	0.017	0.021	0.022	0.023	0.023
	slope	58.1	27.52	18.38	15.61	13.2
	R2	0.191	0.071	0.048	0.039	0.034
MTM	mean absolute t^*	1.17	1.08	0.95	0.83	0.75
	mean misfit	0.005	0.008	0.011	0.012	0.013
	slope	116.37	56.17	30.86	25.08	22.33
	R2	0.218	0.151	0.075	0.068	0.069
WF		12 sec	16 sec	20 sec	24 sec	28 sec
	mean absolute t^*	1.16	1.25	1.35	1.40	1.42
	mean misfit	0.028	0.027	0.027	0.026	0.026
	slope	25.85	30.9	31.14	32.06	31.12
R2	0.123	0.112	0.082	0.072	0.060	
Galapagos		.1 Hz	.14 Hz	.18 Hz	.22 Hz	.26 Hz
DFT	mean absolute t^*	1.75	1.42	1.28	0.96	0.76
	mean misfit	0.017	0.021	0.023	0.023	0.022
	slope	49.25	41.18	32.16	11.96	7.93
	R2	0.160	0.203	0.128	0.031	0.019
MTM	mean absolute t^*	0.89	0.98	0.96	0.79	0.64
	mean misfit	0.004	0.008	0.010	0.012	0.013
	slope	57.44	65.01	51.11	21.39	17.52
	R2	0.110	0.206	0.168	0.054	0.061
WF		12 sec	16 sec	20 sec	24 sec	28 sec
	mean absolute t^*	0.88	1.01	0.97	1.08	1.10
	mean misfit	0.024	0.023	0.023	0.023	0.022
	slope	42.56	34.76	28.09	28.69	28.69
R2	0.271	0.116	0.082	0.072	0.060	

Table 2.5. Mean error, mean misfit, and linear regression results for the synthetic noise tests for the SR method, using DFT and MTM, and the WF method. Original input signals were used as reference. Results are listed for frequency ranges with different upper cutoffs (SR) and time windows of different lengths (WF).

Synthetic noise tests		.1 Hz	.14 Hz	.18 Hz	.22 Hz	.26 Hz	
DFT	mean absolute t* error	0.66	0.34	0.30	0.21	0.17	
	mean misfit	0.010	0.010	0.010	0.010	0.009	
	absolute t* error vs misfit	slope	44.87	27.23	21.74	11.88	7.87
		R2	0.252	0.211	0.182	0.106	0.044
MTM	mean absolute t* error	0.43	0.40	0.39	0.34	0.29	
	mean misfit	0.003	0.004	0.005	0.005	0.006	
	absolute t* error vs misfit	slope	141.38	77.95	59.97	40.49	27.79
		R2	0.472	0.347	0.342	0.288	0.166
WF		12 sec	16 sec	20 sec	24 sec	28 sec	
	mean absolute t* error	1.27	0.79	0.64	0.55	0.47	
	mean misfit	0.035	0.024	0.018	0.013	0.009	
	absolute t* error vs misfit	slope	38.31	22.73	27.28	35.98	43.59
R2		0.273	0.174	0.136	0.142	0.187	

are more negatively proportional to window width. The R^2 values for are also higher than those of the synthetic datasets. We suspect that the differences seen for the synthetic datasets are due to the large t* range assigned to the synthetic “stations” and the fact that these values that did not change with “event”. For more realistic synthetic data, the correlations between misfit and error and between misfit and absolute t* would be more likely to resemble those of the noise tests and the real data, respectively. In summary, we believe that misfit values are adequately correlated with t* error (at least

for errors of sufficient size) and can be used to derive weights for t^* estimates during inversion for Q .

In Figure 2.15 we have used an average of regression slopes to scale misfit values for each method, producing a weighted average of uncertainty (estimated absolute t^* error) for various frames of reference (SH, SV, PL, and anisotropic fast-slow) in real data. For S-waves there appears to be some advantage to using the PL versus the SH component except for the SR method on the Yellowstone data. For SKS arrivals, there is either no advantage or a slight disadvantage to using the PL versus the SV component. Uncertainty tends to be higher for lower frequency and longer time windows, and uncertainties for the WF tend to be slightly higher than for the SR method. This may be the result of including phase information, which, as noted by Bhattacharyya et al. (1996), is more prone than amplitude to be contaminated by noise.

The mantle beneath the Yellowstone region is known to exhibit pronounced anisotropy with a fast direction of $\sim 65^\circ$ (Schutt et al., 1998; Waite et al., 2005). In such circumstances, Boyd et al. (2004) have recommended the use of this frame of reference. Using this approach, uncertainty is consistently higher than results using the other components, which is likely due to secular deviation from this fast direction azimuth.

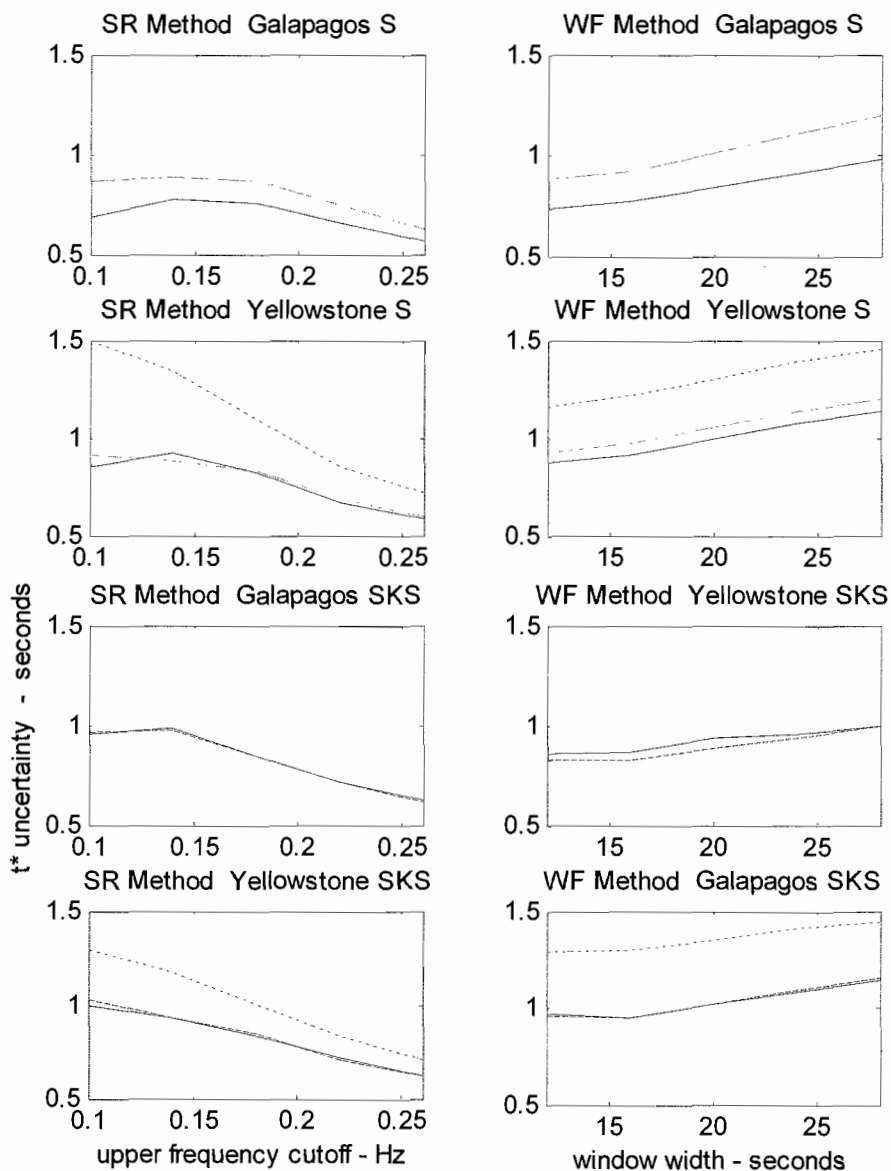


Figure 2.15. Mean estimate uncertainty versus window length (upper cutoff in Hz. for SR and window length in seconds for WF) comprising 1110 S and 492 SKS estimates from the Yellowstone array and 237 S and 134 SKS estimates from the Galapagos array. The components are marked as in Figure 2.11 plus results for the Yellowstone regional fast direction component (dash-dot).

2.5. Conclusions

We have found that the effects of noise may be reduced somewhat by estimating the polarization direction of the input signal and rotating the data into that frame of reference. Rotation to the fast direction azimuth in regions of known anisotropy does not appear to be effective. The use of an averaged reference spectrum or trace does not appear to affect significantly the accuracy of the t^* estimate except in its ability to yield absolute values for Q . The multitaper method of spectral estimation functions best using 7 Slepian tapers but is more prone to error than the discrete Fourier Transform (DFT). We suspect that error for the multitaper method is due to the use of less than the full set of Slepian tapers and that energy leakage is not a factor when ratios of spectra are considered. Smoothing of the DFT may improve line-fitting but can also lead to significant t^* underestimation.

To be useful for tomography, an estimate of t^* must be accompanied by a reliable estimate of its uncertainty. Efforts to assess and possibly reduce this uncertainty usually involve some assumptions as to the nature of input signal and noise content that are seldom well-founded. This is especially true in the selection of window sizes in both time and frequency domains. We propose making multiple t^* estimates using a variety of methods and window sizes. Estimate uncertainties are then based on the degree to which the trace or spectrum predicted by a given reference and t^* estimate matches the observed data, i.e. estimate misfit. These estimate sets may be averaged prior to inversion; however, inverting them separately, using their uncertainties for weights, appears more appropriate; as the results for each set may in a sense be viewed as a “sample of the a

posteriori probability distribution of the model space” (Tarantola, 2005). Finally, our synthetic tests have demonstrated that some degree of correlation exists between estimate misfit and estimate error. This suggests that reliable estimates of uncertainty for real attenuation data can be derived from the observed misfits.

CHAPTER III

ATTENUATION IN THE LABORATORY – A REVIEW

3.1. Laboratory Determination of Q

Currently most laboratory studies on attenuation consist of microcreep or torsional oscillation tests, which yield data in the form of time series of values for strain per unit stress to which is fitted a model creep function ($J(t)$) of either an Andrade or Burgers type (Jackson, 2000):

$$J(t) = J_u + \beta t^n + t/\eta \quad (\text{Andrade}) \quad (3.1)$$

$$J(t) = J_u + \delta J [1 - \exp(-t/\tau)] + t/\eta \quad (\text{Burgers}), \quad (3.2)$$

where J_u is the unrelaxed (fully elastic) compliance, δJ is the storage (anelastic) compliance, τ is the relaxation time constant for the anelastic response, η is the steady state viscosity, and β and n are empirical constants. The Laplace transform of the creep function yields the complex "dynamic compliance":

$$J^*(\omega) = J_u + \delta J (1 + i\omega\tau) - i\omega/\eta, \text{ and} \quad (\text{simple Burgers}) \quad (3.3)$$

$$J^*(\omega) = J_u + \beta \Gamma(1 + n)(i\omega)^{-n} - i/\eta\omega, \quad (\text{Andrade}) \quad (3.4)$$

where Γ is the gamma function, and whose real and negative imaginary parts are, respectively:

$$J_R(\omega) = J_u + \delta J (1 + \omega^2 \tau^2), \text{ and} \quad (3.5)$$

$$J_I(\omega) = \omega \tau \delta J (1 + \omega^2 \tau^2) + 1/\omega \eta; \quad (\text{simple Burgers}) \quad (3.6)$$

$$J_R(\omega) = J_U + \beta \Gamma (1 + n) \omega^{-n} \cos(n\pi/2), \text{ and} \quad (3.7)$$

$$J_I(\omega) = \beta \Gamma (1 + n) \omega^{-n} \sin(n\pi/2) + 1/\eta \omega. \quad (\text{Andrade}) \quad (3.8)$$

Attenuation at each frequency is then calculated as:

$$Q^{-1}(\omega) = J_I(\omega) / J_R(\omega). \quad (3.9)$$

Both models comprise three components: time-independent, recoverable elastic; time-dependent, recoverable anelastic; and time-dependent, non-recoverable viscous; but are ultimately derived from models comprising only two types of mechanical elements, elastic (springs) and viscous (dashpots). For instance, Findley et al. (1976) gives a creep function for a three-component, four-element model:

$$\varepsilon(t) = \sigma_0 / R_1 + \sigma_0 / R_2 [1 - \exp(-R_2 t / \eta_2)] + \sigma_0 t / \eta_1, \quad (3.10)$$

where ε is the strain, σ_0 is the constant applied stress, R_1 and R_2 are spring constants and η_1 and η_2 are coefficients of viscosity. The second term on the right-hand side is the anelastic effect and is described in terms of elastic and viscous parameters. Anelastic and viscous mechanisms tend to be closely linked for both Burgers and Andrade models (Tan et al., 2001) and in the Earth (Karato, 1993). Elastic and anelastic responses are linked for the Andrade model (Jackson, 2000; Tan et al., 2001) and are not always separable for creep responses in general (Findley et al., 1976). This lack of physical transparency poses problems for the use of these simplified creep functions.

These models also do not lend themselves to incorporating the influence of factors other than frequency (e.g. temperature, grain size, partial melting, water content, etc.) unless the number of parameters is substantially increased (Jackson et al., 2002). These other factors are usually modeled in the form of an Arrhenius relationship, e.g. for temperature,

$$Q^{-1} = A \exp(E / RT), \quad (3.11)$$

where A is some constant, E is the activation energy, R is the Gas Constant, and T is the temperature. Grain-size and frequency dependence are incorporated as

$$Q^{-1} = Ad^{-m} T_0^\alpha \exp(-\alpha E/RT), \quad (3.12)$$

where d is the grain size, m is a constant, T_0 is the oscillation period, and α is the frequency dependence exponent (Jackson et al., 2002). The effects of pressure can be included by scaling with the Arrhenius relation, $\exp(PV^*/RT)$, where P is the pressure and V^* is the activation volume. Although based only on dislocation creep studies (Karato and Jung, 2003), Karato (2003) proposes that the effects of temperature, pressure, and water content can be modeled as

$$Q^{-1}(T,P,C_{OH}) \sim [A_d \exp(-H^*_d/RT) + A_w \exp(-H^*_w/RT)]^\alpha, \quad (3.13)$$

where A_d and A_w are constants, and H^*_d and H^*_w are the activation energies for dry and wet conditions, respectively. These relations can be applied to the relaxation time τ or to β and incorporated into the Burger or Andrade models, respectively.

Certain potential attenuation mechanisms have characteristic relaxation times.

For elastically accommodated grain-boundary sliding,

$$\tau = (M\eta_b)/G_U\alpha_b, \quad (3.14)$$

where M is some constant, η_b is grain-boundary viscosity, G_U is the unrelaxed shear modulus, and α_b is the aspect ratio of the grain-boundary region (Faul et al., 2004). For diffusion accommodated grain-boundary sliding,

$$\tau = [(1 - \nu)kTd^p] / [40\pi^3 G_U \delta D_b \Omega], \quad (3.15)$$

where ν is the Poissons ratio, k is the Boltzmann's constant, p is the grain-size sensitivity exponent, δ is the grain-boundary thickness, D_b is grain-boundary diffusivity, and Ω is the molecular volume of the diffusing species. For diffusion-controlled dislocation damping,

$$\tau = (2L^2kT) / (\pi^2\mu b^2\lambda D), \quad (3.16)$$

where L is the dislocation link length, μ is rigidity, b is the Burgers vector, λ is the scale length for dislocation drag mechanism, and D is diffusivity (Minster and Anderson, 1981). Relaxation times can also be calculated for various forms of melt squirt (O'Connell and Budiansky, 1977; Mavko, 1980).

Most commonly a mechanism is not assumed, and a broad distribution of relaxation times is employed:

$$D(\tau) = \alpha H(\tau - \tau_m) H(\tau_M - \tau) / [\tau^{1-\alpha}(\tau_M^\alpha - \tau_m^\alpha)], \quad (3.17)$$

where H is the Heaviside function, and τ_m and τ_M are the minimum and maximum relaxation times (Minster and Anderson, 1981). This is used to form the extended Burgers model:

$$J(t) = J_u \left\{ 1 + \Delta \int_0^\infty D(\tau) [1 - \exp(-t/\tau)] d\tau \right\} + t/\eta, \quad (3.18)$$

where Δ is the anelastic relaxation strength $J_U/\delta J$.

In summary, no model can fully describe attenuation in the Earth without the use of an impractical number of parameters. For this reason, experimental conditions are usually carefully controlled and simplified in order to isolate parameters of interest. This tends to limit the usefulness of laboratory results for the interpretation of seismological data, as do the difficulties associated with extrapolating from laboratory to mantle. These limitations serve to focus current research and debate on a set of related topics: the importance of grain size, the role of dislocation migration, and the effects of water content and partial melt.

3.2. Physical Mechanisms of Attenuation

3.2.1. Grain Size

Studies of mantle xenoliths suggest that considerable portions of the upper mantle are distinctly coarse-grained (1-10 mm) with some megacrysts up to 20 cm (Harte, 1983). While some attenuation studies have been conducted on large (20 mm) olivine single grains (Gueguen et al., 1989), polycrystalline studies, which allow examination of grain

boundary effects, have employed material such as Aheim dunite (Berckhemer et al., 1982; Jackson et al., 1992) with an average grain size of 300 μm . Recent experimental studies have increasingly favored the use of even finer-grained (10-50 μm) synthetic olivine aggregates, which have the advantage of both controlled microstructure and resistance to thermal cracking (Jackson, 2000).

Currently, there is some consensus that the dominant attenuation mechanism under most currently imposed laboratory conditions is elastic or diffusion accommodated grain-boundary sliding (Cooper, 2002; Tan et al., 2001). Diffusion creep is characterized by linear stress dependence and by grain-size dependence varying as either the inverse square (Nabarro-Herring creep) or inverse cube (Coble creep) of the grain diameter. Thus the importance of diffusion creep diminishes rapidly as one approaches anticipated mantle grain sizes, where some suggest that an intragranular process such as dislocation migration is responsible for both creep (Karato et al., 1986) and attenuation (Karato and Spetzler, 1990).

Gribb and Cooper (1998) argue that subgrain boundaries are functionally identical to grain boundaries and thus there is no effective grain size increase in the mantle. They assert that even the results of large single grain studies can be explained on the basis of subgrain size. However, Ashby (1972) provides evidence that the viscosity of low-angle (i.e. subgrain) boundaries is considerably greater than that of grain boundaries, and Stone (1991) and Minster and Anderson (1981) acknowledge that the importance of subgrain boundaries is most likely restricted to long-term steady-state deformation (i.e. creep), whereas smaller scale deformation involving rapid changes in applied stress (such as seen

at seismic frequencies) are more likely to involve dislocations at the centers of subgrains. Under conditions of partial melting the two types of boundary are quite dissimilar, as wetting of sub grain boundaries by melt is not known to occur, and Faul et al. (2004) have demonstrated that elastically accommodated grain boundary sliding is clearly facilitated by the presence of melt. Thus, in the absence of microstructural evidence to the contrary, it is likely that subgrain boundaries do not play a significant role in seismic attenuation.

3.2.2. Dislocation Migration

Although the role of dislocations in steady-state deformation has been extensively studied, such is not the case for their role in attenuation. Dislocation density, style, and distribution have been shown to be sensitive to a number of factors including long-term tectonic stress (Hirth and Lothe, 1982), stress orientation and oxygen fugacity (Bai and Kohlstedt, 1992a), and water content (Mackwell et al., 1985). Such sensitivity has led to difficulties for experimental control of dislocation features (Karato and Spetzler, 1990). Accordingly, in order to assure microstructural uniformity, most experimental attenuation studies anneal their samples so as to remove as many dislocations as possible and also to prevent nucleation of new ones (Gribb and Cooper, 1998; Jackson et al., 2002; Faul et al., 2004). Thus, to date, no experimental study of dislocation-accommodated attenuation in olivine has been undertaken.

Dislocation creep is characterized by exponential stress dependence (exponent ranging from 3 to 5 empirically) and grain-size insensitivity. The transition from

diffusion creep to dislocation creep depends not only upon increasing grain size but also upon temperature and applied stress. For dry, melt-free olivine, Hirth and Kohlstedt (1995a) detected the change in stress dependence at a grain size between 11 and 18 μm . Karato et al. (1986) similarly found the transition in both stress dependence and grain-size sensitivity to occur between 11 and 65 μm .

These studies were conducted at applied stress levels (5 - 250 MPa) far in excess of those typical of seismic waves, which range from 10^{-3} to 10^{-1} MPa (Karato and Spetzler, 1990). On a stress/temperature deformation mechanism map for 100 μm grain size olivine (Twiss and Moore, 1992), mantle temperatures and seismic wave shear stresses lie well within the field of diffusion creep. Such is also the case on a stress/grain-size map for 1300°C (Drury and Fitzgerald, 1998). In attenuation studies at seismic stress levels, Jackson et al. (2002) report a mild grain-size sensitivity over a range of 3 to 23 μm and linear stress dependence. They also suggest that their results can be confidently extrapolated to mantle grain-sizes producing attenuation values that match seismological observations and that diffusion-controlled grain-boundary sliding may be the dominant mechanism in attenuation of seismic waves in the mantle.

Attenuation might involve a mechanism such as Harper-Dorn creep, which involves dislocation climb and is insensitive to both grain-size and stress (Poirier, 1985). Although not yet experimentally verified in olivine, it does occur at low levels of applied stress, such that its deformation map fields (Drury and Fitzgerald, 1998) are appropriate for seismic waves in the mantle.

It is also possible that creep and attenuation under mantle conditions may not involve the same mechanism. Several models for dislocation-controlled mantle rheology distinguish between attenuation and creep mechanisms. Karato (1998) suggests that attenuation in high Peierl's stress minerals is controlled by kink migration and creep by kink nucleation. Minster and Anderson (1981) attribute attenuation to glide of relatively isolated intragrain dislocations and creep to climb and annihilation of dislocations in cell walls.

As noted by Drury and Fitzgerald (1998), each field in a deformation mechanism map indicates that a particular mechanism is dominant but not that other mechanisms are insignificant, particularly when close to field boundaries. In fact, it may be incorrect to consider various deformation mechanisms as fundamentally separate. Dislocation climb, as opposed to dislocation glide, involves diffusion, and grain-boundary sliding involves dislocation migration as well as diffusion (Hirth and Lothe, 1982).

An additional critical factor is dislocation density, which is controlled by accumulated strain. Beyond an optimal density, dislocation mobility is reduced due to interaction between dislocations. Under such conditions, grain-boundary mechanisms would become more important for attenuation. If dislocations can easily climb to cell walls or grain boundaries, dislocation density is reduced, mobility is increased, and intragrain attenuation mechanisms are enhanced. Continued strain and dislocation climb would also promote dynamic recrystallization and reduction in grain size, enhancing grain-boundary mechanisms.

Thus diffusion and dislocation migration, at grain boundaries and interiors, can be simultaneously involved in the attenuation of seismic waves. Their relative importance is likely a function of several factors including tectonic stress and water content.

3.2.3. Water Content and Partial Melt

Water, as H^+ , diffuses rapidly in olivine under mantle conditions (Mackwell and Kohlstedt, 1990), and various lines of evidence (Karato, 1990; Bai and Kohlstedt, 1992b; Hirth and Kohlstedt, 1996) suggest that a significant quantity of water exists in the mantle dissolved as defects in nominally anhydrous minerals such as olivine rather than in hydrous phases. While no experiments have been conducted specifically examining the effects of intragranular water on attenuation in olivine, Jackson et al. (1992) did detect a significant reduction in attenuation as samples were dried during preparation, and Aizawa et al. (2007) have recently developed procedures for studying the effects of *intergranular* water. The effect of water on viscosity is well established in both olivine aggregates (Karato et al., 1986; Chopra and Paterson, 1981) and single crystals by means of enhancing the rate of dislocation glide or climb (Mackwell et al., 1985). In addition, water has been shown to affect preferred lattice orientation (Jung and Karato, 2001a) and grain boundary mobility and thereby grain-size (Jung and Karato, 2001b) in dynamically recrystallized olivine.

Water enhances dislocation climb by increasing interstitial Si defects, which occurs once a sufficient number of metal vacancy defects are occupied by H^+ , shifting the

charge neutrality condition (Mei and Kohlstedt, 2000a, 2000b). This increase directly affects Si diffusion and thus the rate of climb. Dislocation glide (which involves no diffusion) may also be affected by water as H^+ segregates into the dislocation core (Drury, 1991). Water-enhanced diffusion also facilitates grain-boundary sliding (Karato et al., 1986). In the presence of water, therefore, one might expect several mechanisms to be operating yielding non-integer values for stress and/or grain-size exponents between 1 and 2 (e.g. Jackson et al., 2002).

The importance of intracrystalline water content may be highlighted by the introduction of small amounts of melt. In both diffusion and dislocation creep regimes, water-free melt fractions less than 4% show little effect on creep rates (Hirth and Kohlstedt, 1995a, 1995b), which appears to represent a threshold of grain boundary wetting by melt below which strain is not significantly enhanced. This enhancement has been ascribed to both enhanced stress concentration due to decreased grain-to-grain contact and effectively shortened diffusion paths via the melt (Cooper et al., 1989) with the former assuming greater importance in the dislocation creep regime. For attenuation, these would pertain to elastically-accommodated (Faul et al., 2004) and diffusion-accommodated (Gribb and Cooper, 1998) grain-boundary sliding models respectively.

Karato (1986) suggests that for water-undersaturated conditions, onset of partial melting can lead to an *increase* in viscosity (and velocity) as water is partitioned out of the olivine crystal into the melt. Hirth and Kohlstedt (1995a) provided experimental support for this theory. Karato (1995) argues that attenuation should also decrease, although this is yet to be experimentally demonstrated.

Water may have multiple effects on seismic attenuation. It may directly enhance dislocation glide and, by facilitating Si diffusion, dislocation climb and grain-boundary sliding. In the presence of significant tectonic stress, water may, by promoting dislocation climb, both reduce excessive dislocation density enhancing dislocation mobility and promote recrystallization. At low to moderate water concentrations, recrystallization via dislocation recovery can lead to reduction in grain size enhancing grain-boundary mechanisms. At water concentrations above 800 ppm H/Si, however, recrystallization via grain-boundary migration can lead to significant increase in grain size (Jung and Karato, 2001a), which would have the opposite effect.

Stress-induced recrystallization can serve to align the easiest slip system in olivine (i.e. the lattice preferred orientation or LPO) with tectonic stress field. At lower water content, the LPO is (010)[100]. At higher water content, but low to moderate stress, it is (100)[001]. And at high water and high stress, the LPO is (010)[001] (Jung and Karato, 2001b). S-waves whose polarization aligns with the LPO would experience enhanced dislocation mobility and thus greater attenuation. A change in water content after recrystallization would tend to change the LPO but not the crystallographic orientation and might thereby significantly affect attenuation. All these effects require water to be dissolved in the olivine. Any process which significantly reduces intragranular water content such as the partitioning of water from the crystal into partial melt, could be expected to have pronounced and readily detectable consequences.

3.3. Interpretation of Seismic Data

Insight gained from laboratory studies forms the basis for interpreting the results of seismic attenuation studies in terms of the physical attributes of the Earth's interior, particularly in combination with the results of velocity studies. It has been commonly assumed that the primary control on both attenuation and velocity is temperature, resulting in a close inverse correlation between the two. Recently, instances of positive correlation between attenuation and velocity have been reported in the western Pacific (Gomer and Okal, 2003) and the Pacific Northwest (Lawrence et al., 2006), which have been ascribed to olivine composition and water content, respectively.

The next chapter is an excerpt from an article co-authored with Eugene D. Humphreys in which the methods outlined in Chapter II have been applied to a dataset obtained from a recent deployment of broadband seismometers in the Yellowstone area (Wyoming, USA). We examine the nature of both S-wave and P-wave attenuation and its relation to published velocity results.

CHAPTER IV

ATTENUATION TOMOGRAPHY IN THE YELLOWSTONE REGION

This chapter was coauthored by Eugene D. Humphreys.

4.1. Introduction

The Yellowstone-Snake River Plain (YSRP) volcanic system entails an ENE-younging series of silicic eruptive centers buried by subsequent basalt flows. The earliest caldera-forming eruption is thought to have occurred in the McDermitt volcanic field in southeast Oregon at 16-15 Ma (Pierce and Morgan, 1992). Some have also suggested a connection to the eruption of the voluminous Columbia River Basalts to the north at 17.2-14.5 Ma (Brandon and Goles, 1988; Geist and Richards, 1993; Takahashi et al., 1998; Humphreys et al., 2000; Camp and Ross, 2004). The youngest caldera-forming eruption occurred at Yellowstone National Park at 600 Ka with smaller rhyolite flows as recently as 70Ka (Christiansen, 2001). The nature of this magmatic system at depth has occasioned a considerable amount of geological, geochemical, and geophysical investigation along with an extraordinary amount of speculation and controversy.

One theory that has enjoyed widespread popularity interprets the YSRP system as the result of the southwestward transit of the North American Plate over an upwelling of hot mantle material, or plume, which is stationary with regard to and originating at the core-mantle boundary (Pierce and Morgan, 1992). Morgan (1971) was the first to attribute such a lower mantle plume origin to Yellowstone along with about twenty other

“hotspots”, including Iceland and Hawaii. Recently, serious doubts have been raised as to the validity of the deep mantle plume concept in general and its applicability to the YSRP system in particular. Depaolo and Manga (2003) note that the controversy involves two separate questions. First, do any deep mantle plumes exist? And second, are they required for all volcanism not associated with plate boundaries, i.e. all hotspots?

Results from theoretical and laboratory experiments suggest that plumes can form in the thermal boundary layer at the core-mantle boundary (Campbell and Griffiths, 1990), possibly associated with the edges of subducted slabs (Tan et al., 2002). It appears that plumes can also easily cross the transition zone into the upper mantle (Davies, 1995). Courtillot et al. (2003) present a set of criteria that a hot spot fed by deep mantle plume must meet, including the presence of a long-lived track of volcanism, the presence of a flood basalt at the initiation of the track, adequate buoyancy flux based on a topographic anomaly, high $^3\text{He}/^4\text{He}$ ratios presumably characteristic of lower mantle input, and the presence of anomalously low shear velocities at 500 km, indicative of a plume crossing the transition zone. Some question the need for an associated flood basalt (Anderson, 1994; King and Anderson, 1995) or the significance of helium isotope ratios (Meibom et al., 2005). Others consider evidence of the thermal effects of an upwelling plume in the form of thinning of the transition zone due to deflection of the 410 km and 660 km discontinuities to be most critical (Bina and Helffrich, 1994).

Based on their five criteria, Courtillot et al. (2005) find that only 7 out of 49 hotspots examined can be confidently ascribed to deep mantle plumes; while the rest are likely due to upwellings of different sorts. Similarly, Montelli et al. (2004) found

seismological evidence for six hotspots associated with lower-mantle plumes while others appeared confined to the upper mantle. Current consensus is therefore that hotspots fed by mantle plumes originating at the core-mantle boundary probably do exist but are limited in number.

Courtillot et al. (2005) scored Yellowstone positive on four of their deep mantle plume characteristics. A hotspot track is clearly present, and the Columbia River Basalts are a potential candidate for an associated flood basalt. A large long-wavelength topographic anomaly is centered on Yellowstone (Smith and Braile, 1994), from which Sleep (1990) calculated a buoyancy flux of 1.5 Mg/s. And elevated $^3\text{He}/^4\text{He}$ ratios have been detected in hydrothermal fluids in Yellowstone Park (Kennedy et al., 1985). All that was lacking at the time was clear evidence of a negative V_s anomaly at 500km.

In addition to the permanent seismometer network operated by the University of Utah since 1983, there have been several deployment of temporary seismometer arrays in the Yellowstone region. For some of these, the focus has been primarily crustal structure, such as the Yellowstone-Snake River Plain seismic experiments in 1978 and 1980 (Smith et al., 1982) and a 1990-1994 deployment in Yellowstone Park by Miller and Smith (1999). Other arrays have sought to image the entire upper mantle, including deployments by the United States Geological Survey (USGS) in 1973-1975 and 1980 in Yellowstone and the eastern Snake River Plain and three deployments by the Program for the Array Seismic Studies of the Continental Lithosphere (PASSCAL): the 1993 eastern Snake River Plain array (ESRP), the 1999-2000 Billings array, and the 2000-2001 Yellowstone Intermountain Seismic Array (YISA).

Based on data from the USGS arrays, Iyer (1984) identified a negative Vp anomaly beneath Yellowstone extending to 250 km in depth. Using the same data, Dueker and Humphreys (1990) were unable to resolve this anomaly below 240 km. Christiansen et al. (2002) re-examined this dataset and placed the lower limit of the Vp anomaly at 175 km. Their model does show a negative anomaly trending to the northwest with depth extending from 300 to 400 km, which they deem to be an artifact due to streaking.

Data from the PASSCAL-ESRP array revealed negative Vp and Vs anomalies extending to 190 km (Saltzer and Humphreys, 1997; Schutt and Humphreys, 2004) and strong seismic anisotropy in the mantle aligned with the hotspot track (Schutt et al., 1998). Dueker and Sheehan (1997) identified considerable topography on both the 410-km and 660-km discontinuities beneath this array but also a lack of any correlation as evidence of plume transit. Beucler et al. (1999) arrived at a similar conclusion and ascribed discontinuity anomalies to the presence of fragments of the subducted Farallon plate.

Using data from the permanent network and the YISA and Billings Arrays, Waite et al. (2006) have been able to resolve negative anomalies for both Vp and Vs extending to at least 400 km beneath Yellowstone Park, which trend to the WNW at depth. This dip is evident to some extent in all the tomographic models to date. Using P-wave data from all three PASSCAL arrays, Yuan and Dueker (2005) have identified a 100 km diameter plume dipping to the northwest and extending from Yellowstone Park to 500 km. Where this plume contacts the transition zone, Fee and Dueker (2004) detected a depression in

the 410-km discontinuity, consistent with a warm plume, but no corresponding elevation of the 660-km discontinuity.

According to Courtillot et al. (2005), the presence of a negative velocity anomaly at 500 km would qualify Yellowstone as a deep mantle plume, and some global tomographic models image the Yellowstone plume to depths of 1300 km (Bijwaard et al., 1998). Nevertheless, the absence of 660-km discontinuity deflection and the failure of the deep mantle plume model to account for many geologic and tectonic features in the region (Christiansen et al., 2002) have led many to conclude that the upwelling responsible for the YSRP system is confined to the transition zone and upper mantle. Suggested mechanisms for upper mantle upwelling are numerous, including spontaneous development of Rayleigh-Taylor instabilities (Tackley and Stevenson, 1993), convection generated by abrupt variations in lithospheric thickness (King and Anderson, 1995), melt-driven convective instabilities due to plate transport shear (Humphreys et al., 2000), upwelling due to extensional decompression localized by lithospheric features (Christiansen et al., 2002) or opening of a slab window (Thompson, 1977), and transient release of lower mantle material across the 660-km discontinuity (Cserepes and Yuen, 2000; Yuan and Dueker, 2005), among many others. None of these alternatives have been rigorously tested, as the physical state of the mantle beneath the Yellowstone region is yet to be sufficiently constrained.

The studies cited above seek to infer physical characteristics, such as temperature, from seismic velocity, which is in turn inferred from arrival times. Where additional factors, such as composition or partial melt can affect velocity, these inferences are no

longer straightforward; and several studies on the YSRP system have sought to account for their effects (e.g. Saltzer and Humphreys, 1997; Humphreys et al. 2000). Perhaps of far greater importance are the effects of seismic attenuation, which Karato (1993) contends may be responsible for most, if not all, of the velocity anomalies in the mantle commonly attributed to temperature. Several studies on the YSRP system have sought to account for these attenuation, or anelastic, effects (e.g. Schutt and Humphreys, 2004; Waite et al., 2006; Schutt and Dueker, 2008), but in the absence of an attenuation model for the region, these studies could only apply geologically reasonable values derived from the literature.

Historically, the difficulties involved with measuring the raypath integrated effects of attenuation (t^*) have tended to preclude the degree of tomographic resolution possible for velocity studies. The approach presented in Chapter II appears to alleviate some of these problems. In this paper, we apply these techniques to S-wave and P-wave data obtained from the Yellowstone Intermountain Seismic Array (YISA) and invert the results to produce models for S-wave and P-wave attenuation (Q_s and Q_p) for the mantle beneath the Yellowstone region.

4.2. Methods

4.2.1. t^* Estimation

The large uncertainties associated with t^* estimation commend the use of more than one method, each employing multiple parameters. As outlined in Chapter II, we employ both a time domain, wave-form modeling method (WF) and a frequency domain, spectral ratio method (SR). For S-waves we first estimate the polarization direction of the wave and rotate the data into that frame of reference. For P-waves we take the vertical component. We use a Discrete Fourier Transform (DFT) for spectrum estimation rather than the multi-taper method (MTM), and we perform separate estimates on frequency ranges .03-.1Hz, .03-.14Hz, .03-.18Hz, .03-.22Hz, and .03-.26Hz (for S-waves) and .03-.2Hz, .03-.25Hz, .03-.3Hz, .03-.35Hz, and .03-.4Hz (for P-waves). For the wave-form modeling method, we apply time windows of 12, 16, 20, 24, and 28 seconds in length. We also incorporate frequency dependent Q in our attenuation operators in the form $1/Q \sim \omega^\alpha$, setting $\alpha = .2$. We measure the misfit (mean standard error) of the actual windowed trace or spectrum to that predicted by the t^* estimate operating on the reference trace or spectrum. For each set of estimates, these misfit values will be scaled to serve as data weights during inversion.

4.2.2. Inversion

Our grid consists of 60 km blocks arranged 7 deep and 23 by 23 horizontally, and we apply no corrections for station elevations or variations in Moho depth. We use a

biconjugate gradient method (Press et al., 1992) to solve for \mathbf{x} in the basic inverse problem:

$$\mathbf{Ax} = \mathbf{b}, \quad (4.1)$$

where \mathbf{A} is the N by M data kernel matrix comprising the ray-tracing results in seconds, \mathbf{x} is the M by 1 model vector reflecting $1/Q$ for each block, and \mathbf{b} is the N by 1 data vector of t^* estimates. Each side of (4.1) is multiplied by a data covariance matrix \mathbf{C} whose diagonal would normally comprise the inverses of the data variances (σ^2). As these variances are not known, we use the squares of appropriately scaled misfit values. Inversion is regularized by an M by M , nearest neighbor, Laplacian smoothing matrix \mathbf{L} , which is weighted by a scalar smoothing parameter (s).

To minimize the effects of streaking, we employ an approach developed by Humphreys and Clayton (1988), where each block is weighted by the mean of the inverses of the number of rays traversing the block that share a given 20° back azimuth range (e.g. $0-20^\circ$, $20-40^\circ$, etc.). These weights constitute the diagonal of an M by M matrix \mathbf{B} . The final form of the problem becomes:

$$\mathbf{B} \begin{bmatrix} \mathbf{CA} \\ \mathbf{sL} \end{bmatrix}^T \begin{bmatrix} \mathbf{CA} \\ \mathbf{sL} \end{bmatrix} \mathbf{x} = \mathbf{B} \begin{bmatrix} \mathbf{CA} \\ \mathbf{sL} \end{bmatrix}^T \begin{bmatrix} \mathbf{Cb} \\ \mathbf{0} \end{bmatrix} \quad (4.2)$$

where $\mathbf{0}$ is an M by 1 zero vector and T indicates the transpose of a matrix. The iterations continue as long as the L2 norm of the residual vector \mathbf{r} (R.H.S. minus L.H.S. of (4.2)) continues to decline.

4.2.3. Absolute Q and the Trade-off Parameter

As with t^* estimation, attenuation tomography yields only relative values for $1/Q$; yet integration with velocity data usually requires absolute values. A common approach is simply to assign an absolute value to the lowest relative result (e.g. Boyd and Sheehan, 2005). However, the actual range of $1/Q$ is fundamentally determined by the balance between minimizing the norm of the residual vector and minimizing the $1/Q$ model norm (i.e. smoothing). Parker (1994) defines a scalar trade-off parameter (ν) which sets the relative weighting for these two minimization processes. He also suggests that the sum of “standardized” squared residuals (i.e. divided by their variances) is distributed as chi-square with $n - 1$ degrees of freedom. For large n , the median value for this sum would be:

$$\sum_{i=1}^n (r_i / \sigma_i)^2 \sim n - 1. \quad (4.3)$$

If the variances (σ_i^2) are known, a value for ν can be selected which produces residuals that satisfy (4.3). For most inversions, this may not be technically correct; as the residuals should all be drawn from the same underlying distribution and thus share the same variance (Hogg and Ledolter, 1992). But it does suggest an intuitively appropriate constraint, i.e. that the squared residuals and the variances, as data weights, should be of roughly the same magnitude. We use this constraint not to determine the trade-off parameter but instead to determine the scaling factors for the misfit values to yield appropriate variance estimates for data weighting.

For determining the proper trade-off parameter in the form of our smoothing parameter (s), we make use of the following relationship between velocity and attenuation (Minster and Anderson, 1981):

$$V_p(\omega) \sim V_u[1 - \frac{1}{2}(\cot(\pi\alpha/2))Q^{-1}(\omega)], \quad (4.4)$$

Where V_p is the phase velocity, V_u is the unrelaxed velocity, ω is the angular frequency, and α is the frequency dependence exponent for Q . If the velocity anomaly is entirely due to attenuation, the ratio between maximum observed attenuation and maximum negative velocity anomaly would be

$$\Delta Q^{-1}_{\max} / \Delta V_{\max} \sim -2 / \cot(\pi\alpha/2). \quad (4.5)$$

As a ratio exceeding this value would be aphysical, this sets an effective upper limit on the absolute value of $\Delta 1/Q$ and therefore on the range of relative $1/Q$ results from inversion. Anderson and Givens (1982) have observed the value for α to vary between .1 and .3. We have found that misfit values for the SR method can be slightly reduced by using α values in a similar range. For this range of α , the velocity anomalies reported by Waite et al. (2006) for Yellowstone, $\Delta V_s = -5.5\%$ and $\Delta V_p = -2.3\%$, yield maximum $\Delta 1/Q$ values ranging from .0199 to .0585 and .0097 to .0259, respectively. As with our WF method attenuation operators, we have chosen to set $\alpha = .2$, yielding a maximum $\Delta 1/Q_s$ of .0382 and a maximum $\Delta 1/Q_p$ of .0174. But constraining maximum $\Delta 1/Q_p$ to this value requires a degree of smoothing which tends to make inversions unstable. Accordingly, we employ the commonly accepted Q_p/Q_s ratio of 1.75 and set maximum $\Delta 1/Q$ to .0218. We have also assigned a minimum $1/Q$ value of .0025, yielding ranges of 25-400 for Q_s and 41-400 for Q_p . Since it is unlikely that attenuation

is entirely responsible for the velocity anomalies, we would expect actual Q to be somewhat higher than these values.

4.3. Results

Figure 4.1 displays horizontal slices through the S-wave attenuation models derived from the different t^* estimate sets. Results from waveform estimates tend to be more coherent and more consistent than those from spectral ratio estimates, but, for the most part, all appear quite similar. Also plotted is a $\Delta V_s = -0.25\%$ contour. The main region of high attenuation tends to track the region of lower velocity which trends to the NW with depth, although most models show it offset slightly to the SE from the velocity anomaly. The WF models also show a region of increased attenuation to the southeast at depth, which the SR models reflect less clearly.

The dominant back azimuths for events used in this study are to the NW and to a lesser extent, the SW and SE. This would suggest that the models at depth may be the result of vertical “streaking” along dominant raypaths lacking crossing rays. Figure 4.2 shows the number of rays entering the base of the model for the dominant back azimuths, along with a contour delimiting the regions of $Q_s < 50$ (for an average of WF models). The low- Q_s lobe to the NW appears to be covered by both NW and SW raypaths and does not coincide with that of the highest density of raypaths from either back azimuth. The central low- Q_s region coincides somewhat with the highest density of SW, but not NW, raypaths. The SE low- Q_s zone is covered only by SE raypaths but does not

Figure 4.1. Depth slices through $1/Q_s$ models from inversion of ten different sets of t^* estimates. The models are listed by upper frequency cutoff in hertz for spectral ratio estimates and by window width in seconds for waveform estimates. Shown are the location of the Yellowstone caldera (X) and the contour for $\Delta V_s = -0.25\%$. Variance reduction of weighted data for each model are listed along the base of the figure.

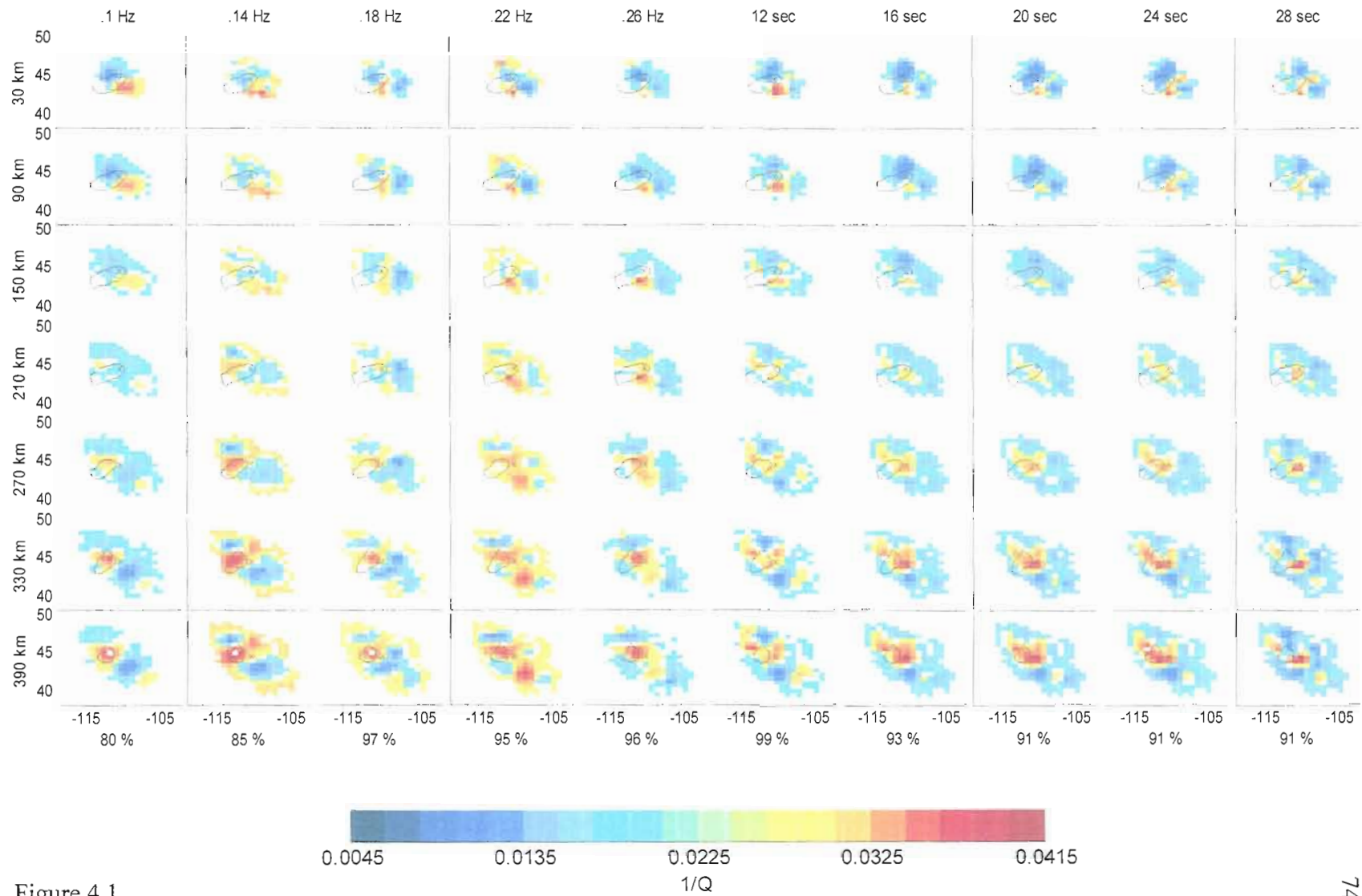


Figure 4.1.

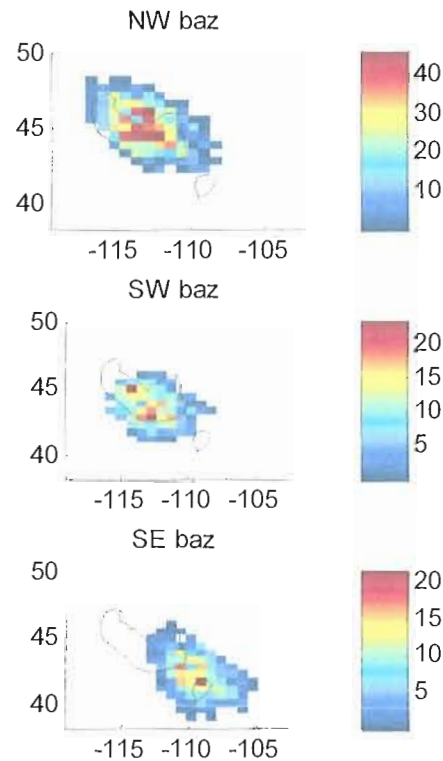


Figure 4.2. S-wave ray density plot for the base of the model for events with northwest, southwest, and southeast back azimuths. Shown are contours for $Q_s < 50$.

coincide with the area of their highest density. When we perform inversions using only events with NW back azimuths, the NW low- Q_s zone is evident but less so than when all events are used. It is also present in some inversions when only SW back azimuths are used. The SE low- Q zone is only evident when inversions are limited to SE back azimuths; while the central zone is clearly evident in all the inversions. We conclude that the central and NW zones are likely not due to streaking; whereas the SE zone is of doubtful validity. Traces recorded at stations within Yellowstone National Park were prone to distortion most likely due to interaction with the magma body known to underlie

the area. This tends to complicate picking arrivals in velocity studies (Waite et al., 2006). When these stations are excluded the attenuation models are not markedly affected.

Figure 4.3 shows horizontal slices through the P-wave attenuation models along with a $\Delta V_p = -0.25\%$ contour. As with the S-wave results, a high attenuation zone consistently develops to the NW at depth, but none appears to the SE. The central low- Q_p zone appears to be even more offset to the SE from the low V_p zones of Waite et al. (2006). Most of the models place a significant amount of attenuation at shallower levels but not directly beneath the Park, especially for WF models. Figure 4.4 is similar to Figure 4.2 with the contour for $Q_p < 70$. The central low Q_p zone is covered by rays from all three back azimuths, and the northwest low- Q_p zone is covered mainly by raypaths from the northwest. Both zones coincide with the respective low- Q_s zones in Figure 4.2. On this basis we consider both features to be valid.

4.4. Discussion

4.4.1. Decoupling of V and Q Anomalies

Velocity perturbations are, to first order, the result of variations in temperature with the relationship given by Karato (1993):

$$\delta \ln V(\omega, X_V) / \delta T = \delta \ln V_0(\omega) / \delta T - H^* / \pi Q(\omega, T, X_Q) RT^2, \quad (4.6)$$

where H is the activation enthalpy and R is the gas constant. The first part of the right hand side constitutes the anharmonic and the second part the anelastic (i.e. dispersion) effects. Q not only mediates the temperature dependency of velocity but is also itself dependent on temperature. The normal expectation is that higher temperature should

Figure 4.3. Depth slices through $1/Q_p$ models from inversion of ten different sets of t^* estimates. The models are listed by upper frequency cutoff in hertz for spectral ratio estimates and by window width in seconds for waveform estimates. Shown are the location of the Yellowstone caldera (X) and the contour for $\Delta V_p = -0.25\%$. Variance reduction of weighted data for each model are listed along the base of the figure.

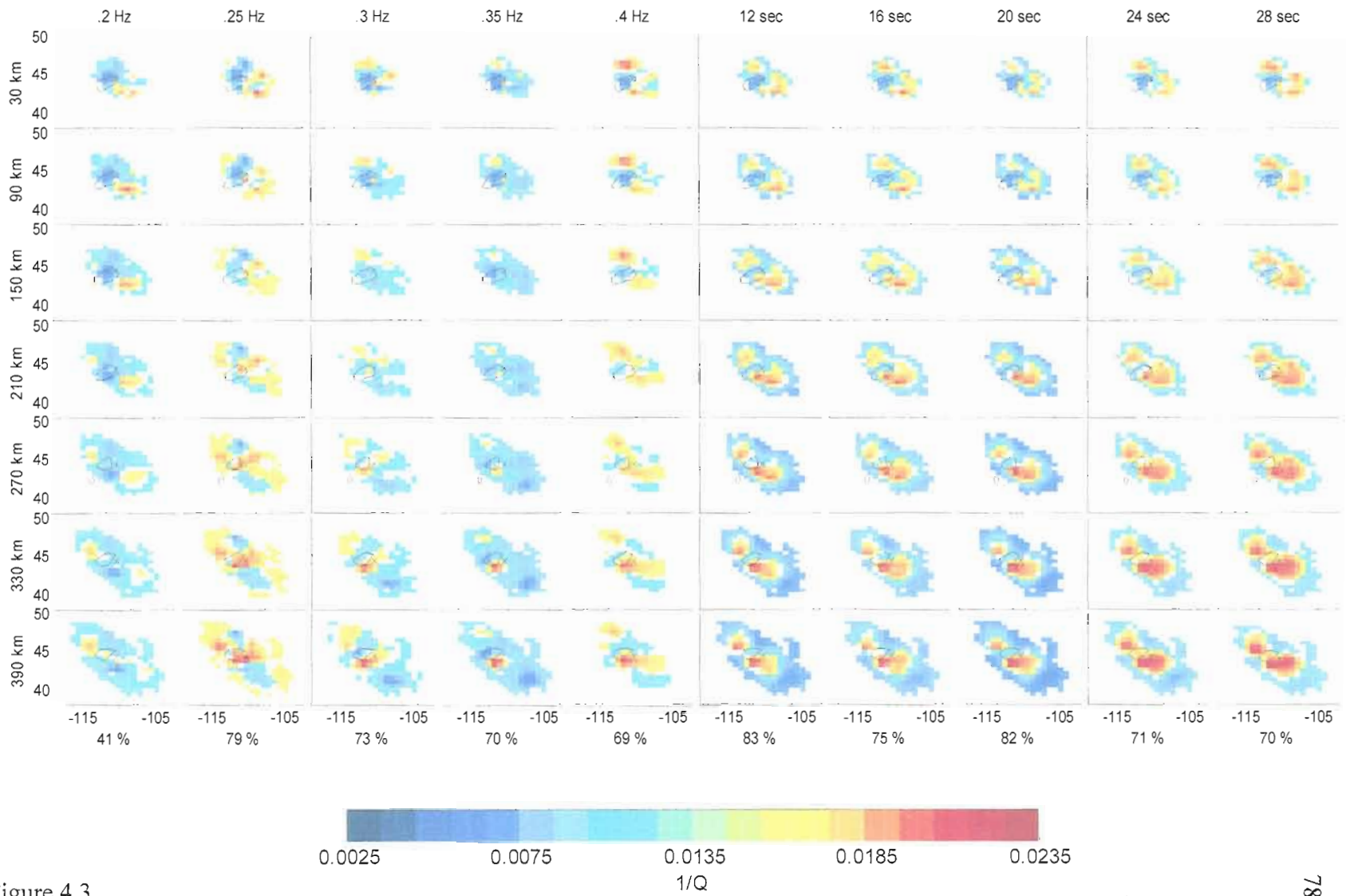


Figure 4.3.

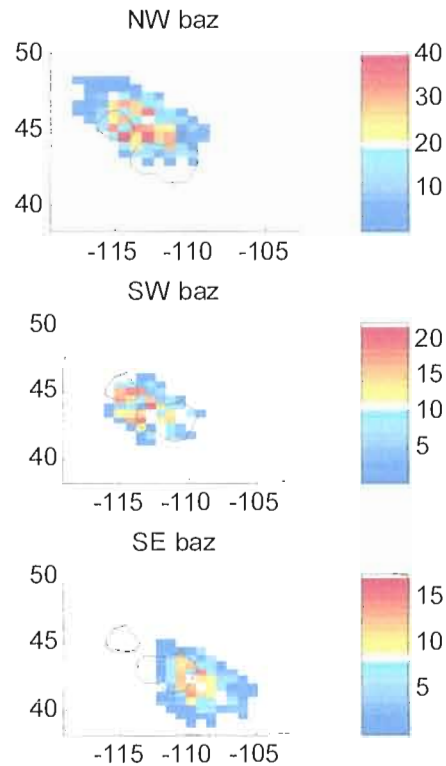


Figure 4.4. P-wave ray density plot for the base of the model for events with northwest, southwest, and southeast back azimuths. Shown are contours for $Q_p < 70$.

yield lower velocity and lower Q . It is therefore unusual that in our Yellowstone attenuation models, Q does not exactly follow velocity. Lawrence et al. (2006), in a continental-scale study, also note this decoupling in the northwestern US, which appeared particularly pronounced in the Yellowstone region and which they ascribe to variations in water content.

Equation (6) shows both V and Q as dependent on not only frequency (ω) but also composition (X). Compositional changes such as due to basalt depletion affect velocity primarily through changes in density to which Q is relatively insensitive (Karato, 2003).

On the other hand, high water content (primarily as intracrystalline H^+ ions) can reduce Q by more than 75% under mantle conditions (Karato, 1995) but affects velocity only by means of attenuation and to a much lesser degree.

Partial melting can exploit this water effect as water will partition into the melt, thereby dehydrating the olivine crystal and increasing Q , particularly if the melt is immediately removed, i.e. fractional versus batch melting (Karato and Jung, 1998). Schutt and Humphreys (2004) suggest that 0.4% partial melt exists between 90 and 180 km beneath the Snake River Plain. Waite et al. (2006) propose that up to 1% partial melt exists between 50 and 200 km beneath Yellowstone and interpret the decrease in velocity anomaly amplitude between 200 and 250 km as due to partial melt dehydration.

Figure 4.5 plots the average $1/Q$ for the plume versus depth for the ten different attenuation models. The average of all models for non-plume areas show little variation with depth. At depth, average plume $1/Q_s$ ($\sim .03$) is higher than the non-plume $1/Q_s$ ($\sim .02$) and decreases steadily toward the top of the model ($\sim .017$). Average plume $1/Q_p$ at the base of the model ($\sim .014$) is also slightly larger than non-plume $1/Q_p$ and achieves a maximum at ~ 300 km, where it decreases rapidly towards the surface ($\sim .007$). In both cases attenuation at the top of the model is greater for non-plume areas than for the plume.

There is considerable reason to believe that during the Laramide orogeny extensive hydration of the lithospheric mantle, due to shallow subduction of the Farallon plate, occurred beneath the western U.S. to depths of 200 km (Humphreys et al., 2003) and especially the Yellowstone region (Feeley, 2003). There is also reason to believe that

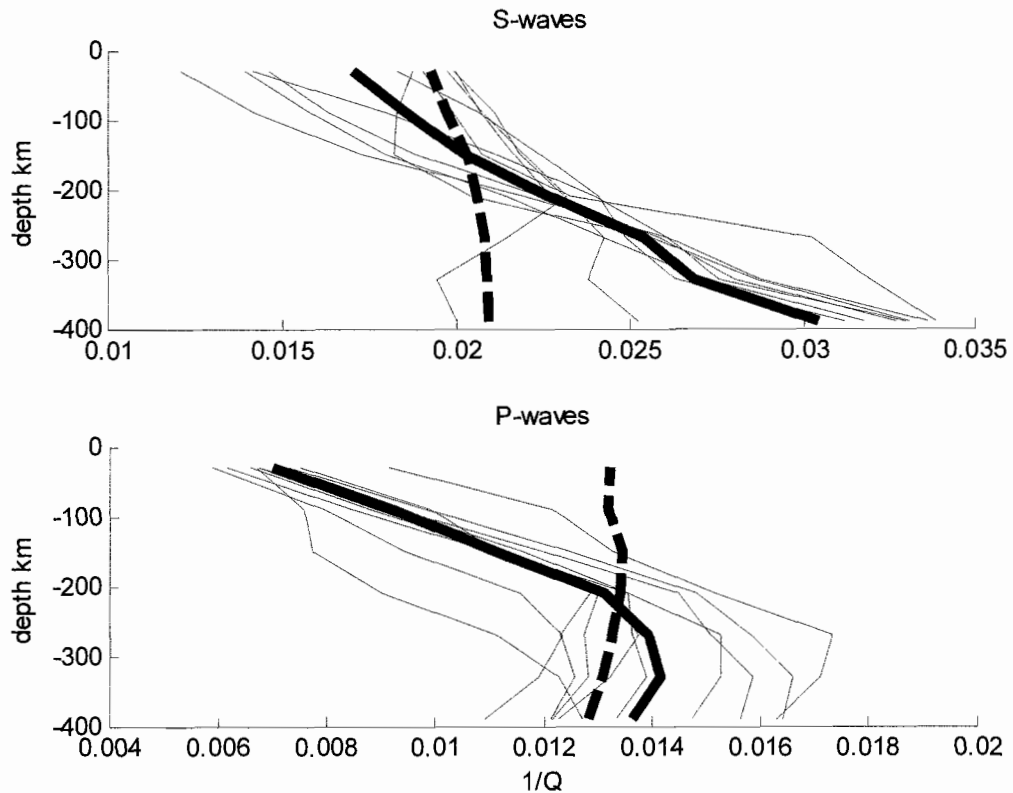


Figure 4.5. Average $1/Q$ for plume (solid) and non-plume (dashed) areas versus depth for ten estimate sets. Averages of all sets are in bold. Demarcation of plume and non-plume areas is $\Delta V = -0.25\%$. Shown are results for a) S-waves and b) P-waves.

in comparison the upwelling plume material is relatively dry (Adams, 1997, 1999, 2004). Rapid increase in slab dip (e.g. Coney and Richards, 1977) and/or more rapid removal by downward buckling (Humphreys, 1995) may have caused some hydration across the entire upper mantle. If so, the low- Q zones at the base of the models (Figures 4.1 and 4.3) may reflect relatively hydrous asthenospheric mantle adjacent to (i.e. offset from) the dry plume. Heat from the plume would drive this mantle toward its solidus, which is lowered due to presence of water. Sato et al. (1989) have demonstrated that the ratio of temperature to solidus temperature is more important for attenuation than temperature

itself or, for dry peridotite, the onset of partial melting. The plume itself, though hotter than the surrounding mantle, has lower intracrystalline water content and would be farther from its solidus, thus appearing as a relatively high-Q zone.

As the plume rises and decompresses, it approaches its solidus and $1/Q_p$ increases until ~ 250 km where partial melting of the plume material and/or the directly adjacent mantle begins. Crystal dehydration rapidly decreases $1/Q$, increasing velocity and causing the reduction of velocity anomaly noted by Waite et al. (2006) and the anomaly “gap” evident in the model of Christiansen et al. (2002). Though cooler, the adjacent mantle is still wetter than the plume which still appears as relatively high-Q. As the plume continues to ascend (Figure 4.5), it cools rapidly, further decreasing $1/Q$; while the surrounding mantle, now non-convecting lithosphere, cools more slowly maintaining more or less constant Q . At the top of the model, which represents the top 60 km, the average Q_s is roughly 60 and 50, and Q_p is roughly 140 and 80, for plume and non-plume areas, respectively. For reference, within the Yellowstone caldera Clawson et al. (1989) report $Q_p \sim 40$ for hydrothermally-altered sediments and $Q_p \sim 200$ for unaltered, yet hot, solidified granitic material. Outside the caldera they report Q_p for the upper crust greater than 200.

4.4.2. Decoupling of Q_p and Q_s

In general, Q_p and Q_s are felt to be tightly coupled, such that if one is known the other may be calculated by means of

$$Q_p/Q_s = (3/4)(V_p/V_s)^2. \quad (4.7)$$

For a Poisson solid this yields a value of 1.75 (Anderson and Given, 1982), which has been seen to fit the data in phase pair attenuation studies (Roth et al., 1999). Upper mantle PREM velocities yield an average of 2.45. For Yellowstone, Waite et al. (2006) use a value of 2.5. In our case, the value ranges from .72 to 3.83 with a mean of 1.67. Some, but not all, of this variation is likely due to differences in ray coverage between S-wave and P-wave models (e.g. Schutt and Humphreys, 2004). Figure 4.6 shows horizontal slices for Q_p/Q_s (average of all models). For all depths, the region underlying

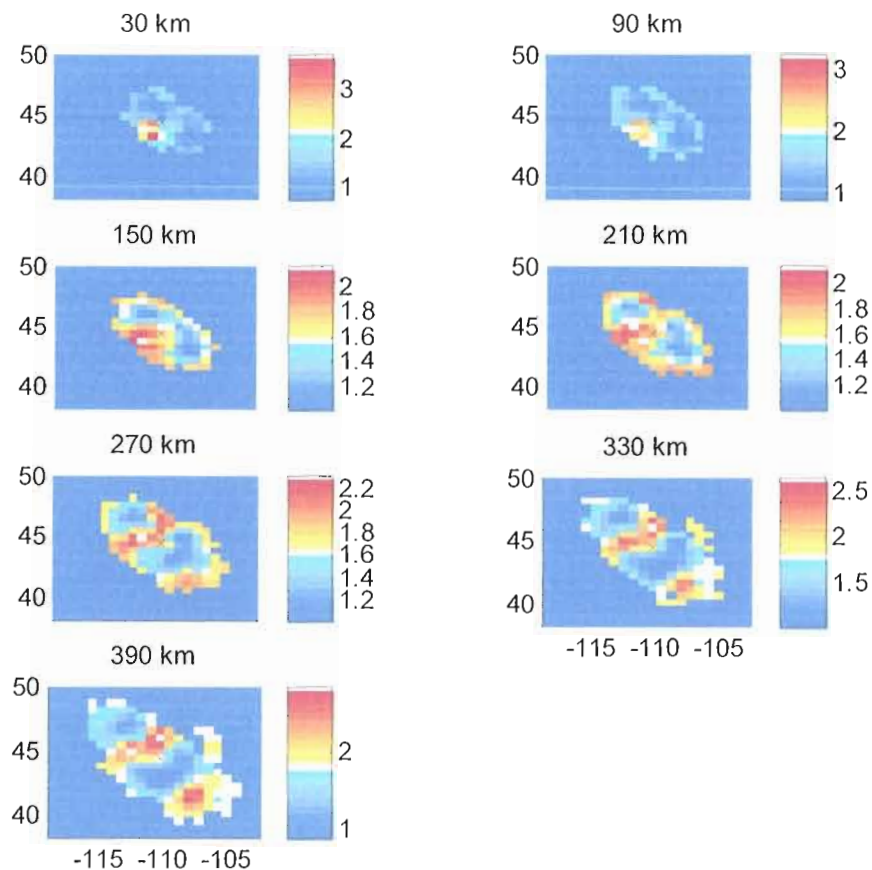


Figure 4.6. Depth slices of Q_p/Q_s , average for 10 models.

Yellowstone and the Snake River Plain shows relatively higher Q_p compared to the areas to the south, southeast, and northwest of Yellowstone which show relatively higher Q_s .

One possible explanation is that P-waves can better resolve the narrow low-attenuation plume due to their higher average frequency (Figure 4.7). But given $V_p > V_s$, S-wave and P-wave wavelengths, and therefore Fresnel zones, are roughly similar. Lawrence et al. (2006) use the same frequency range (.08-.083 Hz) in t^* estimation for both waves; yet the low-attenuation anomaly for Yellowstone is still much better resolved by the P-waves. It appears more likely that S-waves are more sensitive to interference by some feature of the hotspot.

The presence of partial melt affects V_s more than V_p , allowing V_p/V_s to be used as a proxy in detecting its presence (e.g. Schutt and Humphreys, 2004). In the absence of water, such is not the case for Q where the onset of melting is not seen to cause a marked change in Q_p (Sato et al., 1989). Hammond and Humphreys (2000) show that, at seismic frequencies using realistic pore geometries, the melt squirt mechanism contributes to neither S-wave nor P-wave attenuation; although the presence of a few larger pockets of melt or zones of preferentially aligned pores does allow for considerable attenuation at seismic frequencies. Stevenson (1989) suggests that in a region undergoing large-scale deformation, melt will preferentially migrate into melt-rich lenses or veins which may eventually form an interconnected drainage network, greatly facilitating fractional as opposed to batch melting. The Yellowstone-Snake River Plain magmatic system has experienced considerable extensional deformation from its inception 17 my ago to the present (Pierce and Morgan, 1992; Smith and Braile, 1994). In the mantle beneath this

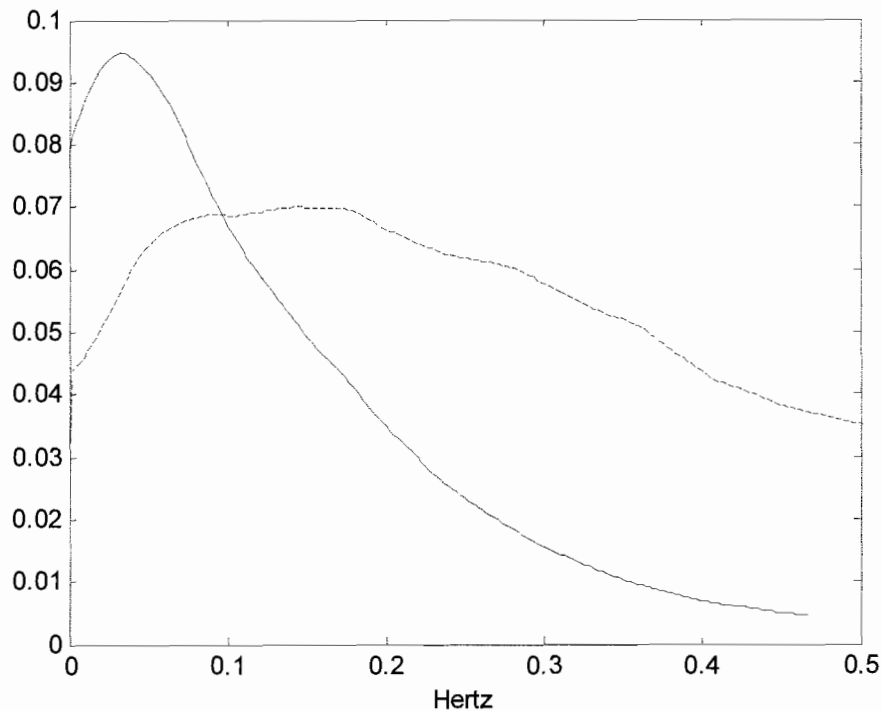


Figure 4.7. Average of normalized spectra for 1602 S-wave traces (solid) and 1166 P-wave traces (dashed).

region large, oriented bodies of melt may be the rule rather than exception. Geologically recent volcanism both in Yellowstone and the Snake River Plain suggest that these drainage systems may remain substantially molten. In response to extensional deformation it is possible that these bodies assume a form (perhaps sheeted) to which S-waves are more sensitive than P-waves, thus generating some of the Q_p/Q_s variation seen in our results.

A more likely explanation is some interaction with the plume which preferentially affects S-waves. Tilmann et al. (1998) have modeled such interaction and find that while P- and S-waves are similarly susceptible to phase conversion and scattering, S-waves are

much more strongly focused by the plume. This focusing can cause apparent attenuation by diffraction of seismic energy. As modeled by Allen et al. (1999), the resulting apparent attenuation pattern consists of a central zone of low attenuation flanked by zones of high attenuation occurring some distance “downstream” from the plume depending on epicentral distance, plume diameter, and degree of velocity reduction within the plume.

In Figure 4.8 we have stacked interpolated t^* plots which have been rotated so that the back azimuth is toward the top. We use the plume’s position at depth rather than at the surface (i.e. the caldera) as the point of rotation. The S-wave plot differs from that of the P-wave in that it contains significantly more high attenuation between 50 and 250 km downstream from the plume. Tillman et al. (1998) have determined that for P-waves an epicentral distance of 90° would have roughly half the focal length of an event with an epicentral distance of 60° . In Figure 4.8 we have stacked results from events with epicentral distances varying from 29° to 112° degrees. Thus we would expect considerable upstream and downstream smearing of the apparent attenuation patterns of Allen et al. (1999), which assume a distance of $\sim 60^\circ$. Their models are based on plume diameters ranging from 100-175 km and negative S-wave velocity anomalies of 4.2-12%. These values are broadly consistent with the estimated 100km plume diameter (Yuan and Dueker, 2005) and V_s anomaly of -5.5% (Waite et al., 2006) for Yellowstone. Tilmann et al. (1998) report much weaker focusing (i.e. longer focal lengths) for P-waves, suggesting that whatever apparent attenuation might occur for P-waves would not be observed by the YISA.

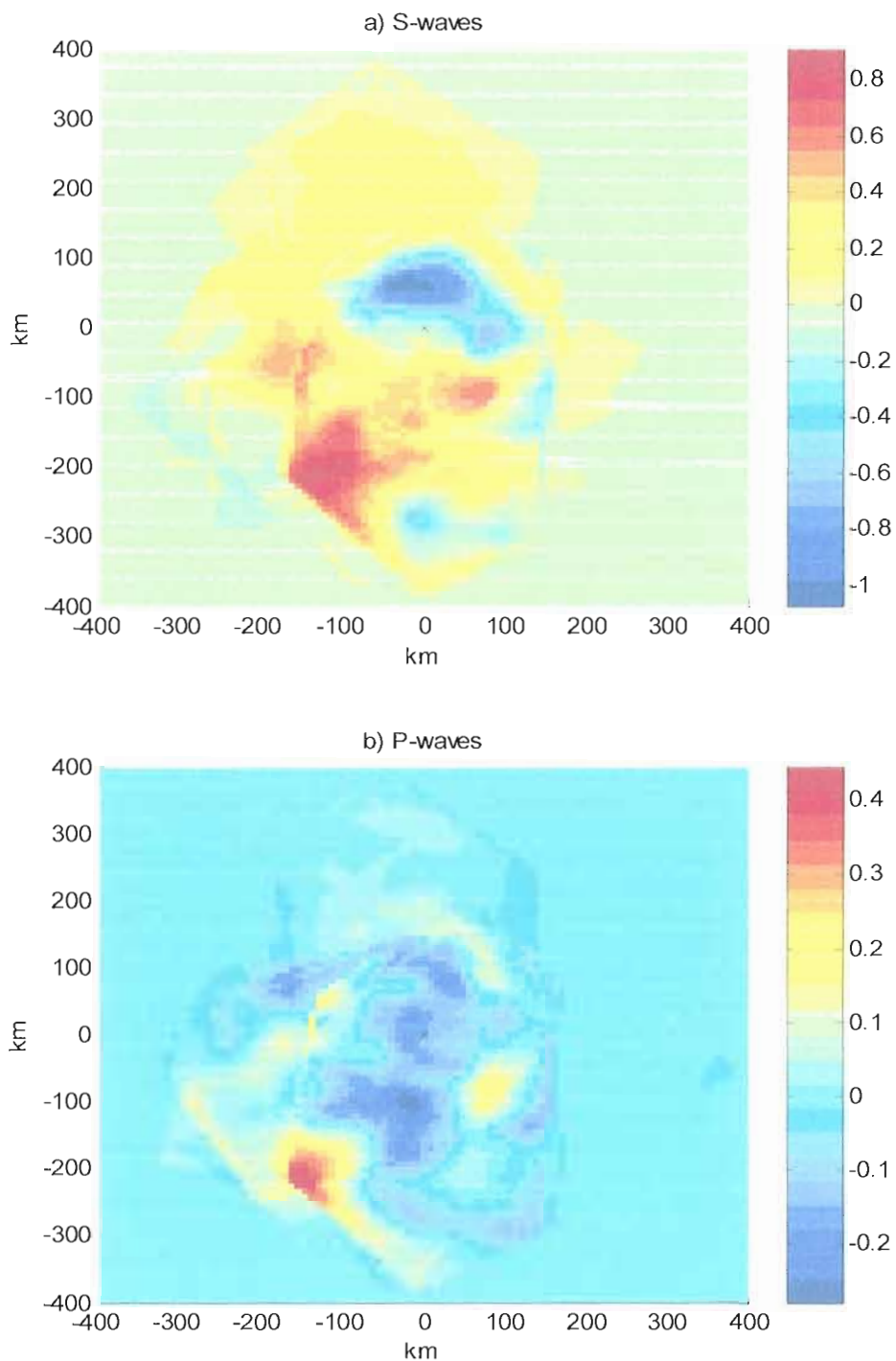


Figure 4.8. Average of interpolated t^* maps which have been rotated to place the back azimuth upwards for a) S-waves (51 events) and b) P-waves (38 events). Pole of rotation is marked by an x. t^* values used are averages of the 10 estimate sets.

4.4.3. Implications for Estimates of Plume Temperature

The most commonly employed method for derivation of temperature anomalies given velocity anomaly and attenuation is that of Karato (1993),

$$\delta \ln V / \delta T = \delta \ln V_0 / \delta T - (\pi\alpha/2) \cot(\pi\alpha/2) (1/(\pi Q)) (H/(RT_0^2)), \quad (4.8)$$

where $\delta \ln V_0 / \delta T$ is the anharmonic temperature derivative, α is the attenuation frequency dependence exponent, H is the attenuation activation energy, R is the Gas Constant, and T_0 is average mantle temperature. For α , H , and T_0 , we use .2, 500 kJ/mol, and 1600°K, respectively. Figure 4.9 displays the mean values for plume excess temperature (ΔT) versus depth, where the plume is delimited by $\Delta V < -0.25\%$. The results for P-waves and S-waves are broadly equivalent at depth, where ΔT is between 30°C and 50°C until ~250 km, where ΔT increases rapidly. For P-waves, excess temperatures are between 100°C and 180°C at the top of the model. For S-waves at this level, ΔT values are similar but some exceed 200°C. These shallow ΔT values most likely reflect a sharp decrease the temperature of the surrounding non-plume mantle.

In our temperature calculations we have not considered the effects of composition, grain size, water content, or partial melt. These effects, though potentially significant, are probably less important than anelastic effects and would likely not change the basic trends in the temperature model presented here. Other studies on the YSRP system have taken these other factors into account but have lacked attenuation data. Compared to these studies, our results are in general agreement as to the magnitude of ΔT in the upper 200 km. Schutt and Humphreys (2004) estimate ΔT to be $80^\circ \pm 90^\circ$ between the central low-velocity zone and the high-velocity sides at depths from 80 to 190 km

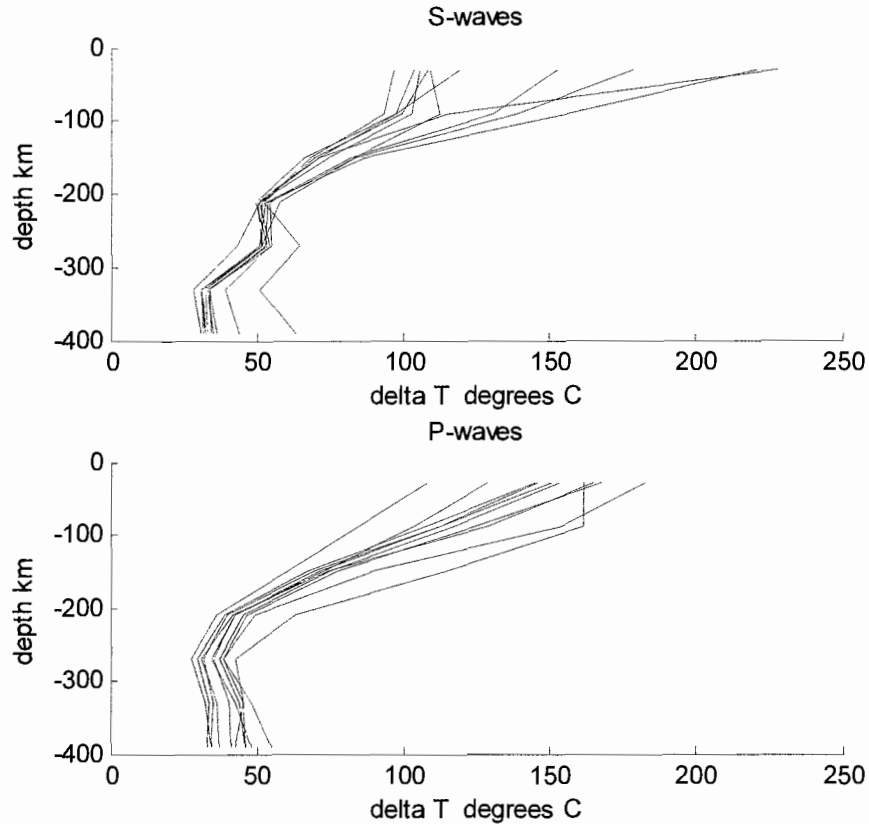


Figure 4.9. Mean plume ΔT values versus depth for 10 $1/Q$ models for a) S-waves and b) P-waves.

beneath the eastern Snake River Plain. For the “plume layer” (50-120 km) beneath the Yellowstone hotspot track, Schutt and Dueker (2008) estimate $\Delta T > 70^\circ$ for a grain-size sensitive model (2 mm) and $\Delta T > 120^\circ$ for two anelastic and two melt-velocity scaling models. Waite et al. (2006) suggest that from 50 to 200 km beneath Yellowstone Park $\Delta T < 100^\circ$ with $Q_s < 100$ and $< 1\%$ partial melt. From 250 to 400 km, they estimate low Q and ΔT up to 120° .

A significant difference in our model is that all of our attenuation estimates yield relatively low ΔT values at 400 km. These could be shifted to higher values by applying

greater smoothing during inversion yielding generally lower $1/Q$. This tends to make inversion unstable and does not affect the overall ΔT trends. Models which produce greater ΔT at depth would also produce excessive ΔT at shallow levels.

This low excess temperature may explain the minimal deflection seen in the 410-km discontinuity and lack of deflection in the 660-km discontinuity. In modeling plume penetration of the transition zone, Davies (1995) assumed a ΔT of 570° . It is not clear the excess temperature revealed by this study would allow a Yellowstone plume to penetrate the 660-km discontinuity, let alone traverse the lower mantle from the core-mantle boundary.

4.5. Conclusions

Although S-wave t^* estimates appear to be more susceptible to error due to the effects of plume focusing, all S-wave and P-wave tomographic models reveal relatively high attenuation at depth within the region that velocity models suggest to be the mantle plume responsible for the Yellowstone hotspot. The low excess plume temperatures implied by these attenuation models suggest that the origin of the plume is restricted to the upper mantle and perhaps the transition zone. These models, of course, depend on the maximum $1/Q$ assumed to be physically reasonable given the velocity model for the region. If smaller values for this maximum are assumed, the resulting models will yield higher ΔT values at depth but will also yield higher excess temperatures and lower attenuation at shallow levels than may be geologically reasonable. In addition, the degree

of smoothing required to produce lower attenuation values adversely affects inversion due to overweighting of the smoothing matrix compared to the data.

Depth profiles for P-wave attenuation and for both P-wave and S-wave excess temperature show a pronounced inflection at ~ 250 km, which we believe can be ascribed to the onset of partial melting. Intracrystalline water is partitioned out of the olivine and into the melt, decreasing dislocation mobility and thereby attenuation. It is likely that most of the “plume” portions of the models which show high attenuation at depth and the effects of melting at ~ 250 km are actually previously hydrated lithospheric and/or asthenospheric mantle surrounding the relatively dry, upwelling mantle plume. Our results suggest that in certain circumstances water content, by means of its effects on attenuation, may be more important than temperature in the generation of velocity anomalies.

CHAPTER V

CONCLUSIONS

The difficulties involved in the study of seismic attenuation have tended to limit the extent to which such studies are undertaken and/or their results are useful in the interpretation of seismic velocity models. These difficulties are primarily the result of signal contamination by noise, but efforts to reduce or eliminate this contamination by selective filtering or windowing have often increased error by eliminating portions of the signal as well. Since it appears that the nature of noise, especially signal-generated, is impossible to assess *a priori*, it is preferable to employ t^* estimation methods in both time and frequency domains using a variety of window sizes in each. Associated with each estimate is a careful assessment of its uncertainty, which is used to weight the estimate during tomographic inversion.

Tomographic models based on these methods for t^* estimation using the data from the Yellowstone Intermountain Seismic Array display both some variation and some basic consistency between methods. Also evident are some consistent differences between S-wave and P-wave results, which can be ascribed to the effects of preferential focusing of S-wave energy by the mantle plume. For shallower levels, all models show the plume (defined as a negative velocity anomaly) as having lower attenuation than the surrounding mantle. This reflects the juxtaposition of a hot but relatively dry plume and

a pre-existing mantle which has been extensively hydrated during shallow subduction of the Farallon plate.

At depth all models show a plume with relatively high attenuation. When combined with velocity models this tends to limit possible values for excess plume temperature to $< 100^{\circ}\text{C}$ and more likely $< 50^{\circ}\text{C}$. These temperatures do not support the theory that the Yellowstone-Snake River Plain volcanic system is fed by a mantle plume which originates at the core-mantle boundary and traverses both the lower mantle and the transition zone.

REFERENCES

- Adams, D.C. 1996. Late Miocene calc-alkaline volcanism in southern Jackson Hole, Wyoming: evidence of subduction-related volcanism? Geological Society of America Abstracts with Program **28**:A-483.
- Adams, D.C., 1997. Miocene calc-alkaline volcanism in southern Jackson Hole, Wyoming: evidence of subduction-related volcanism. M.S. Thesis. Montana State University, Bozeman, Montana.
- Adams, D.C. 2004. Mantle hydration and Sr-Nd isotope systematics in the Yellowstone region. Geological Society of America Abstracts with Program **36-4**:96.
- Aki, K. 1982. Scattering and attenuation. Bulletin of the Seismological Society of America **72**:S319-S330.
- Aki, K., and B. Chouet. 1975. Origin of coda waves: Source, attenuation, and scattering effects. Journal of Geophysical Research **80-23**:3322-3342.
- Aki, K., and P.G. Richards. 2002. Quantitative Seismology, 2nd edition, University Science Books, Sausalito, California, 700 pp.
- Allen, R.M., G. Nolet, W.J. Morgan, K. Vogfjord, B.H. Bergsson, P. Erlendsson, G.R. Foulger, S. Jakobsdottir, B.R. Julian, M. Pritchard, S. Ragnarsson, and R. Stefansson. 1999. The thin hot plume beneath Iceland. Geophysical Journal International **137**:51-63.
- Anderson, D.L. 1994. The sublithospheric mantle as the source of continental flood basalts: the case against the continental lithosphere and plume head reservoirs. Earth and Planetary Science Letters **123**:269-280.
- Anderson, D.L., and J.W. Given. 1982. Absorption band Q model for the Earth. Journal of Geophysical Research **87B5**:3893-3904.
- Anderson, D.L., and J.B. Minster. 1979. The frequency dependence of Q in the Earth and implications for mantle rheology and Chandler wobble. Geophysical Journal of the Royal Astronomical Society **58**:431-440.

- Ashby, M.F. 1972. Boundary defects, and atomistic aspects of boundary sliding and diffusional creep. *Surface Science* **31**:498-542.
- Bai, Q., and D.L. Kohlstedt. 1992a. High-temperature creep of olivine single crystals, 2. Dislocation structures. *Tectonophysics* **206**:1-29.
- Bai, Q., and D.L. Kohlstedt. 1992b. Substantial hydrogen solubility in olivine and implications for water storage in the mantle. *Nature* **357**:672-674.
- Berckhemer, H., W. Kampfmann, E. Aulbach, and H. Schmeling. 1982. Shear modulus and Q of forsterite and dunite near partial melting from forced-oscillation experiments. *Physics of the Earth and Planetary Interiors* **29**:30-41.
- Beucler, E., S., Chevrot, and J. Montagner. 1999. The Snake River Plain experiment revisited: relationships between a Farallon plate fragment and the transition zone. *Geophysical Research Letters* **26**:2673-2676.
- Bhattacharyya, J., G. Masters, and P. Shearer. 1996. Global lateral variations of shear wave attenuation in the upper mantle. *Journal of Geophysical Research*. **101B10**:22273-22289.
- Bijwaard, H., W. Spakman, and E.R. Engdahl. 1998. Closing the gap between regional and global travel time tomography. *Journal of Geophysical Research* **103-B12**:30055-30078.
- Bina, C.R., and G. Helffrich. 1994. Phase transition Clapeyron slopes and transition zone seismic discontinuity topography. *Journal of Geophysical Research* **99**:15853-15860.
- Biot, M.A. 1956. Theory of propagation of elastic waves in a fluid-saturated porous solid. I. Low-frequency range. *Journal of the Acoustical Society of America* **28-2**:168-178.
- Boyd, O.S., C.H. Jones, and A.F. Sheehan. 2004. Foundering lithosphere imaged beneath the southern Sierra Nevada, California, USA. *Science* **305**:660-662.
- Boyd, O.S., and A.F. Sheehan. 2005. Attenuation tomography beneath the Rocky Mountain Front: Implications for the physical state of the upper mantle: in *The Rocky Mountain Region: An Evolving Lithosphere*. *Geophysical Monograph Series* **154**. Karlstrom, K.E., and G.R. Keller, eds. American Geophysical Union, Washington, D.C.
- Brandon, A.D., and G.G. Goles. 1988. A Miocene subcontinental plume in the Pacific Northwest: geochemical evidence. *Earth and Planetary Science Letters* **88**:273-283.

- Camp, V.E., and M.E. Ross. 2004. Mantle dynamics and genesis of mafic magmatism in the intermontane Pacific Northwest. *Journal of Geophysical Research* **109**:B08204. doi:10.1029/2003JB002838.
- Campbell, I.H., and R.W. Griffiths. 1990. Implications of mantle plume structure for the evolution of flood basalts. *Earth and Planetary Science Letters* **99**:79-93.
- Chan, W.W., and Z.A. Der. 1988. Attenuation of multiple ScS in various parts of the world. *Geophysical Journal*. **92**:303-314.
- Chopra, P.N., and M.S. Paterson. 1984. The role of water in the deformation of dunite. *Journal of Geophysical Research* **89**:7861-7876.
- Christiansen, R.L. 2001. The Quaternary and Pliocene Yellowstone Plateau volcanic field of Wyoming, Idaho, and Montana. United States Geological Survey Professional Paper **729-G** 144p.
- Christiansen, R.L., G.R. Foulger, and J.R. Evans. 2002. Upper-mantle origin of the Yellowstone hotspot. *Geological Society of America Bulletin* **114**:1245-1256.
- Clawson, S.R., R.B. Smith, and H.M. Benz. 1989. P wave attenuation of the Yellowstone caldera from three-dimensional inversion of spectral decay using explosion source seismic data. *Journal of Geophysical Research* **94B6**:7205-7222.
- Clouser, R.H., and C.A. Langston. 1995. Modeling P-Rg conversions from isolated topographic features near the NORESS array. *Bulletin of the Seismological Society of America* **85**:859-873.
- Coney, P.J. and S.J. Reynolds. 1977. Cordilleran Benioff zones. *Nature* **270**:403-406.
- Cooper, R.F. 2002. Seismic wave attenuation: Energy dissipation in viscoelastic crystalline solids. *in* Plastic Deformation of Minerals and Rocks, Reviews in Mineralogy and Geochemistry **51**:253-290.
- Cooper, R.F., and D.L. Kohlstedt. 1986. Rheology and structure of olivine-basalt partial melts. *Journal of Geophysical Research* **91**:9315-9323.
- Cooper, R.F., D.L. Kohlstedt, and K. Chyung. 1989. Solution-precipitation enhanced creep in solid-liquid aggregates which displays a non-zero dihedral angle. *Acta Metall.* **37**:1759-1771.

- Cormier, V.F. 1982. The effect of attenuation on seismic body waves. *Bulletin of the Seismological Society of America* **72**:S169-S200.
- Courtillot, V., A. Davaille, J. Besse, and J. Stock. 2003. Three distinct types of hotspots in the Earth's mantle. *Earth and Planetary Science Letters* **205**:295-308.
- Cserepes, L., and D.A. Yuen. 2000. On the possibility of a second kind of mantle plume. *Earth and Planetary Science Letters* **183**:61-71.
- Davies, G.F. 1995. Penetration of plates and plumes through the mantle transition zone. *Earth and Planetary Science Letters* **133**:507-516.
- DePaolo, D.J. and M. Manga. 2003. Deep origin of hotspots: the mantle plume model. *Science* **300**:920-921.
- Ding, X.Y. and S.P. Grand. 1993. Upper mantle Q structure under the East Pacific Rise. *Journal of Geophysical Research* **98**:1973-1975.
- Dorman, L.M. 1968. Anelasticity and the spectra of body waves. *Journal of Geophysical Research* **73-12**:3877-3883.
- Dorman, L.M. 1969. Reply to J.-Cl. DeBremaeker's comments on 'Anelasticity and the spectra of body waves'. *Journal of Geophysical Research* **74-12**:3304-3307.
- Drury, M.R. 1991. Hydration-induced climb dissociation of dislocations in naturally deformed mantle olivine. *Physics and Chemistry of Minerals* **18**:106-116.
- Drury, M.R., and J.D. Fitzgerald. 1998. Mantle rheology: Insights from laboratory studies of deformation and phase transition. *in* *The Earth's Mantle: Composition, Structure, and Evolution*. I. Jackson. ed. Cambridge University Press. New York. p. 503-559.
- Dueker, K., and E.D. Humphreys. 1990. Upper-mantle velocity structure of the Great Basin. *Geophysical Research Letters* **17**:1327-1330.
- Dueker, K.G., and A.F. Sheehan. 1997. Mantle discontinuity from midpoint stacks of converted P to S waves across the Yellowstone hotspot track. *Journal of Geophysical Research* **102**:8313-8327.
- Dziewonski, A.M., and J.M. Steim. 1982. Dispersion and attenuation of mantle waves through waveform inversion. *Geophysical Journal of the Royal Astronomical Society* **70**:503-527.

- Engelhard, L. 1996. Determination of seismic-wave attenuation by complex trace analysis. *Geophysical Journal International* **125**:608-622.
- Faul, U.H., J.D. Fitzgerald, and I. Jackson. 2004. Shear-wave attenuation and dispersion in melt-bearing olivine polycrystals II. Microstructural interpretation and seismological implications. *Journal of Geophysical Research* **109**:B06202. doi:10.1029/2003JB002407.
- Fee, D., and K. Dueker. 2004. Mantle transition zone topography and structure beneath the Yellowstone hotspot. *Geophysical Research Letters* **31**:L18603 doi:10.1029/2004GL020636.
- Feeley, T.C. 2003. Origin and tectonic implications of across-strike geochemical variations in the Eocene Absaroka volcanic province, United States. *Journal of Geology* **111**:329-346.
- Findley, W.N., J.S. Lai, and K. Onaran. 1976. Creep and relaxation of non-linear viscoelastic materials. North-Holland, Amsterdam, 367 pp.
- Flanagan, M.P., and D.A. Wiens. 1994. Radial upper mantle attenuation structure of inactive back arc basins from differential shear wave measurements. *Journal of Geophysical Research* **99**:15469-15484.
- Futterman, W.I. 1962. Dispersive body waves. *Journal of Geophysical Research* **67**-**13**:5279-5291.
- Geist, D., and M. Richards. 1993. Origin of the Columbia Plateau and Snake River Plain: deflection of the Yellowstone plume. *Geology* **21**:789-792.
- Gladwyn, M.T., and F.D. Stacey. 1974. Anelastic degradation of acoustic pulses in rock. *Physics of the Earth and Planetary Interiors* **8**:332-336.
- Gomer, B.M., and E.A. Okal. 2003. Multiple-ScS probing of the Ontong-Java Plateau. *Physics of the Earth and Planetary Interiors* **138**:317-331.
- Gribb, T.T., and R.F. Cooper. 1998. Low-frequency shear attenuation in polycrystalline olivine: Grain boundary diffusion and the physical significance of the Andrade model for viscoelastic rheology. *Journal of Geophysical Research* **103**:27267-27279.
- Guegen, Y., M. Darot, P. Mazot, and J. Woignard. 1989. Q^{-1} of forsterite single crystals. *Physics of the Earth and Planetary Interiors* **55**:254-258.

- Halderman, T.P., and P.M. Davis. 1991. Qp beneath the Rio Grande and East Africa rift zones. *Journal of Geophysical Research* **96**-B6:10113-10128.
- Hammond, W.C., and E.D. Humphreys. 2000. Upper mantle seismic wave attenuation: Effects of realistic partial melt distribution. *Journal of Geophysical Research* **105**:10987-10999.
- Harte, B. 1983. Mantle peridotites and processes: the kimberlite sample. *in* Continental basalts and mantle xenoliths. C.J. Hawkesworth and M.J. Norry, eds. Shiva Publishing, Chesire, U.K.
- Hirth, G., and D.L. Kohlstedt. 1995a. Experimental constraints on the dynamics of the partially molten upper mantle: Deformation in the diffusion creep regime. *Journal of Geophysical Research* **100**:1981-2001.
- Hirth, G., and D.L. Kohlstedt. 1995b. Experimental constraints on the dynamics of the partially molten upper mantle 2. Deformation in the dislocation creep regime. *Journal of Geophysical Research* **100**:15441-15449.
- Hirth, G., and D.L. Kohlstedt. 1996. Water in the upper mantle: implications for rheology, melt extraction, and the evolution of the lithosphere. *Earth and Planetary Science Letters* **144**:93-108.
- Hirth, J.P., and J.L. Lothe. 1982. *Theory of Dislocations*. Krieger Publishing Company, Malabar, Florida. 856pp.
- Hogg, R.V., and J. Ledolter. 1992. *Applied statistics for engineers and physical scientists*. MacMillan Publishing Company, New York. 472pp.
- Ho-Liu, P., H. Kanamori, and R.W. Clayton. 1988. Applications of attenuation tomography to Imperial Valley and Coso-Indian Wells region, southern California. *Journal of Geophysical Research* **93**:10501-10520.
- Humphreys, E.D. 1995. Post-Laramide removal of the Farallon slab, western United States. *Geology* **23**:987-990.
- Humphreys, E.D., and R.W. Clayton. 1988. Adaptation of back projection tomography to seismic travel time problems. *Journal of Geophysical Research* **93**:1073-1085.
- Humphreys, E.D., K.G. Dueker, D.L. Schutt, and R.B. Smith. 2000. Beneath Yellowstone: Evaluating plume and non-plume models using teleseismic images of the upper mantle. *GSA Today* **10**:1-7.

- Humphreys, E.D., E. Hessler, K. Dueker, G.L. Farmer, E. Erslev, and T. Atwater. 2003. How Laramide-age hydration of the North American lithosphere by the Farallon slab controlled subsequent activity in the western United States. *International Geology Review* **45**:575-595.
- Iyer, H.M. 1984. A review of crust and upper mantle structure studies of the Snake River Plain-Yellowstone volcanic system: A major lithospheric anomaly in the western U.S.A. *Tectonophysics* **105**:291-308.
- Jackson, I. 2000. Laboratory measurement of seismic wave dispersion and attenuation: Recent progress: in Earth's deep interior: Mineral physics and tomography from the atomic to global Geophysical Union, Washington, p. 265-289.
- Jackson, I., M.S. Paterson, and J.D. Fitzgerald. 1992. Seismic wave dispersion and attenuation in Aheim dunite: an experimental study. *Geophysical Journal International* **108**:517-534.
- Jackson, I., J.D. Fitzgerald, U.H. Faul, and B.H. Tan. 2002. Grain-size sensitive seismic-wave attenuation in polycrystalline olivine. *Journal of Geophysical Research* **107**:2360 doi:10.1029/2001JB001225.
- Jacobson, R.S. 1987. An investigation into the fundamental relationships between attenuation, phase dispersion, and frequency using seismic refraction profiles over sedimentary structures. *Geophysics* **52**:72-87.
- Jacobson, R.S., G.G. Shor, and L.M. Dorman. 1981. Linear inversion of body wave data – Part II: Attenuation versus depth using spectral ratios. *Geophysics* **46**:152-162.
- Jacobson, R.S., and B.T.R. Lewis. 1990. The first direct measurements of upper oceanic crustal compressional wave attenuation. *Journal of Geophysical Research* **95**:17417-17429.
- Jannsen, D., J. Voss, and F. Theilen. 1985. Comparison of methods to determine Q in shallow marine sediments from vertical reflection seismograms. *Geophysical Prospecting* **33**:479-497.
- Jung, H., and S. Karato. 2001a. Water-induced fabric transitions in olivine. *Science* **293**:1460-1463.
- Jung, H., and S. Karato. 2001b. Effects of water on dynamically recrystallized grain-size in olivine. *Journal of Structural Geology* **23**:1337-1344.

- Karato, S. 1986. Does partial melting reduce the creep strength of the upper mantle? *Nature* **319**:309-310.
- Karato, S. 1990. The role of hydrogen in the electrical conductivity of the upper mantle. *Nature* **347**:272-273.
- Karato, S. 1993. Importance of anelasticity in the interpretation of seismic tomography. *Geophysical Research Letters* **20**:1623-1626.
- Karato, S. 1995. Effects of water on seismic wave velocities in the upper mantle. *Proceedings of the Japanese Academy* **71**:61-66.
- Karato, S. 1998. A dislocation model of seismic wave attenuation and micro-creep in the Earth: Harold Jeffreys and the rheology of the solid Earth. *Pure and Applied Geophysics* **153**:239-256.
- Karato, S. 2003b. Mapping water content in the upper mantle. *in* The subduction factory. *American Geophysical Union Monograph* **135**.
- Karato, S., M.S. Paterson, and J.D. Fitzgerald. 1986. Rheology of synthetic olivine aggregates: Influence of grain size and water. *Journal of Geophysical Research* **91**:8151-8176.
- Karato, S., and H.A. Spetzler. 1990. Defect microdynamics in minerals and solid-state mechanisms of seismic wave attenuation and velocity dispersion in the mantle. *Reviews of Geophysics* **28**:399-421.
- Karato, S., and H. Jung. 1998. Water, partial melting, and the origin of the low velocity and high attenuation zone in the upper mantle. *Earth and Planetary Science Letters* **157**:193-207.
- Karato, S., and H. Jung. 2003. Effects of pressure on high-temperature dislocation creep in olivine. *Philosophical Magazine A* **83**:401-414.
- Kennedy, B.M., M.A. Lynch, J.H. Reynolds and S.P. Smith. 1985. Intensive sampling of noble gases in fluids at Yellowstone: early overview of the data; regional patterns. *Geochimica et Cosmochimica Acta* **49**:1251-1261.
- King, S.D., and D.L. Anderson. 1995. An alternative mechanism of flood basalt formation. *Earth and Planetary Science Letters* **136**:269-279.

- Lawrence, J.F., P.M. Shearer, and G. Masters. 2006. Mapping attenuation beneath North America using waveform cross-correlation and cluster analysis. *Geophysical Research Letters* **33**:L07315. doi:10.1029/2006GL025813.
- Lay, T., and T.C. Wallace. 1983. Multiple ScS travel times and attenuation beneath Mexico and Central America. *Geophysical Research Letters* **10**:301-304.
- Lay, T., and T.C. Wallace. 1988. Multiple ScS attenuation and travel times beneath western North America. *Bulletin of the Seismological Society of America* **78**:2041-2061.
- Lees, J.M., and G.T. Lindley. 1994. Three-dimensional attenuation tomography at Loma Prieta: inversion of t^* for Q. *Journal of Geophysical Research* **99-B4**:6943-6863.
- Lees, J.M., and J. Park. 1995. Multiple-taper spectral analysis: a stand-alone C-subroutine. *Computers and Geosciences* **21**:199-236.
- Levander, A.R., and N.R. Hill. 1985. P-SV resonances in irregular low-velocity surface layers. *Bulletin of the Seismological Society of America* **75**:847-864.
- Liu, H-P., D.L. Anderson, and H. Kanamori. 1976. Velocity dispersion due to anelasticity; implications for seismology and mantle composition. *Geophysical Journal of the Royal Astronomical Society* **47**:41-58.
- Mackwell, S.J., D.L. Kohlstedt, and M.S. Paterson. 1985. The role of water in the deformation of olivine single crystals. *Journal of Geophysical Research* **90-B13**:11319-11333.
- Mackwell, S.J., and D.L. Kohlstedt. 1990. Diffusion of hydrogen in olivine: Implications for water in the mantle. *Journal of Geophysical Research* **95**:5079-5088.
- Marquering, H., G. Nolet, and F.A. Dahling. 1998. Three-dimensional waveform sensitivity kernels. *Geophysical Journal International* **132**:521-534.
- Maquering, H., F.A.Dahlen, and G. Nolet. 1999. Three-dimensional sensitivity kernels for finite-frequency traveltimes: The banana-doughnut paradox. *Geophysical Journal International* **137**:805-815.
- Mavko, G.M. 1980. Velocity and attenuation in partially molten rocks. *Journal of Geophysical Research* **85**:5173-5189.

- Mei, S., and D.L. Kohlstedt. 2000a. Influence of water on plastic deformation of olivine aggregates 1. Diffusion creep regime. *Journal of Geophysical Research* **105**:21457-21469.
- Mei, S., and D.L. Kohlstedt. 2000b. Influence of water on plastic deformation of olivine aggregates 2. Dislocation creep regime. *Journal of Geophysical Research* **105**:21471-21481.
- Meibom, A., N.H. Sleep, K. Zahnle, and D.L. Anderson. 2005. Models for noble gases in mantle geochemistry: some observations and alternatives. *Geological Society of America Special Paper* **338**:347-363.
- Menke, W. 1989. *Geophysical Data Analysis: Discrete Inverse Theory*. International Geophysics Series, v. **45**, Academic Press, San Diego, California.
- Miller, D.S., and R.B. Smith. 1999. P and S velocity of the Yellowstone volcanic field from local earthquake and controlled-source tomography. *Journal of Geophysical Research* **104-B7**:15105-15121.
- Minster, J.B., and D.L. Anderson. 1981. A model of dislocation-controlled rheology for the mantle. *Philosophical Transactions, Royal Society of London A* **299**:319-356.
- Montalbetti, J.F., and E.R. Kanasevich. 1970. Enhancement of teleseismic body phases with a polarization filter. *Geophysical Journal of the Royal Astronomical Society* **21**:119-129.
- Montelli, R.G., G. Nolet, F.A. Dahlen, G. Masters, E.R. Engdal, and S.-H. Hung. 2004. Finite-frequency tomography reveals a variety of plumes in the mantle. *Science* **303**:338-343.
- Morgan, W.J. 1971. Convection plumes in the lower mantle. *Nature* **230**:42.
- Nakanishi, I. 1979. Attenuation of multiple ScS waves beneath the Japanese arc. *Physics of the Earth and Planetary Interiors* **19**:337-347.
- Nolet, G., R. Allen, and D. Zhao. 2007. Mantle plume tomography. *Chemical Geology* **241**:248-263.
- Nowick, A.S., and B.S. Berry. 1972. *Anelastic relaxation in crystalline solids*. Academic, San Diego, 667p.
- O'Connell, R.J., and B. Budiansky. 1977. Viscoelastic properties of fluid-saturated cracked solids. *Journal of Geophysical Research* **82**:5719-5735.

- Park, J., C.R. Lindberg, and F.L. Vernon. 1987. Multitaper spectral analysis of high-frequency seismograms. *Journal of Geophysical Research* **92-B12**:12,675-12,684.
- Parker, R.L. 1994. *Geophysical Inverse Theory*. Princeton University Press. Princeton, New Jersey, USA.
- Pierce, K.L., and L.A. Morgan. 1992. The track of the Yellowstone hot spot: Volcanism, faulting, and uplift. *in* *Regional Geology of Eastern Idaho and Western Wyoming*. P.K. Link, M.A. Kuntz, and L.B. Platt, eds. Geological Society of America Memoir **179**: 1-53.
- Poirier, J.P. 1985. *Creep of Crystals. High –Temperature Processes in Metals, Ceramics, and Minerals*. Cambridge University Press.
- Press, W.H., S.A. Teukolsky, W.T. Vetterling, and B.P. Flannery. 1992. *Numerical Recipes in C: The Art of Scientific Computing*. Cambridge University Press, Cambridge, U.K.
- Reid, F.J.L., J.H. Woodhouse, and H.J. van Heijst. 2001. Upper mantle attenuation and velocity structure from measurements of differential S phases. *Geophysical Journal International* **145**:615-630.
- Richards, P.G., and W. Menke. 1983. The apparent attenuation of a scattering medium: *Bulletin of the Seismological Society of America* **73-4**:1005-1021.
- Romanowicz, B. 1990. The upper mantle degree 2: Constraints and inferences from global mantle wave attenuation measurements. *Journal of Geophysical Research* **95-B7**:11051-11071.
- Romanowicz, B., and J.J. Durek. 2000. Seismological constraints on attenuation in the Earth: a review. *in* *Earth's deep interior: Mineral physics and tomography from the atomic to the global scale*. S. Karato, A.M. Forte, R.C. Liebermann, G. Masters, and L. Stixrude eds., American Geophysical Union Geophysical Monograph **117**.
- Roth, E.G., D.A. Wiens, L.M. Dorman, J. Hildebrand, and S.C. Webb. 1999. Seismic attenuation tomography of the Tonga-Fiji region using phase pair methods. *Journal of Geophysical Research* **104-B3**:4795-4809.
- Sailor, R.V., and A.M. Dziewonski. 1978. Measurements and interpretation of normal mode attenuation. *Geophysical Journal of the Royal Astronomical Society* **53**:559-581.

- Saltzer, R.L., and E.D. Humphreys. 1997. Upper mantle P wave velocity structure of the eastern Snake River Plain and its relationship to geodynamic models of the region. *Journal of Geophysical Research* **102-B6**:11829-11841.
- Sanders, C. 1984. Location and configuration of magma bodies beneath Long Valley, California, determined from anomalous earthquake signals. *Journal of Geophysical Research* **89**:8287-8392.
- Sanders, C., P. Ho-Liu, D. Rinn, and H. Kanamori. 1988. Anomalous shear wave attenuation in the shallow crust beneath the Coso Volcanic Region, California. *Journal of Geophysical Research* **93-B4**:3321-3338.
- Sato, H., I.S. Sacks, T. Murase, G. Muncill, and H. Fukuyama. 1989. Qp-melting temperature relation in peridotite at high pressure and temperature: Attenuation mechanism and implications for the mechanical properties of the upper mantle. *Journal of Geophysical Research* **94**:10647-10661.
- Schoenberger, M., and F.K. Levin. 1974. Apparent attenuation due to intrabed multiples. *Geophysics* **39-3**:278-291.
- Schutt, D., E.D. Humphreys, and K. Dueker. 1998. Anisotropy of the Yellowstone hot spot wake, eastern Snake River Plain, Idaho. *Pure and Applied Geophysics* **151**:443-462.
- Schutt, D., and K. Dueker. 2008. Temperature of the plume layer beneath the Yellowstone hotspot. *Geology* **36**:623-626. doi:10.1130/G24809A.1.
- Schutt, D.L., and E.D. Humphreys. 2004. P and S wave velocity and Vp/Vs in the wake of the Yellowstone hot spot. *Journal of Geophysical Research* **109**:B01305. doi:10.1029/2003JB002442.
- Selby, N.D., and J.H. Woodhouse. 2002. The Q structure of the upper mantle: Constraints from Rayleigh wave amplitudes. *Journal of Geophysical Research* **107**:ESE5-1–ESE5-11. 10.1029/2001JB000257.
- Sheehan, A.F., and S.C. Solomon. 1992. Differential shear wave attenuation and its lateral variation in the North Atlantic region. *Journal of Geophysical Research* **97**:15339-15350.
- Shearer, P.M. 1999. *Introduction to Seismology*. Cambridge University Press, Cambridge, U.K.

- Sipkin, S.A., and T.H. Jordan. 1980. Regional variation of Qscs. *Bulletin of the Seismological Society of America* **70**:1071-1102.
- Slack, P.D., P.M. Davis, W.S. Baldrige, K.H. Olsen, A. Glahn, U. Achauer, and W. Spence. 1996. The upper mantle structure of the central Rio Grande region from teleseismic P and S wave travel time delays and attenuation. *Journal of Geophysical Research* **101-B7**:16003-16023.
- Smith, R.B., L.W. Braille, M.M. Schilly, J. Ansorge, C. Prodehl, M. Baker, J.H. Healey, S. Mueller, and R. Greensfelder. 1982. The Yellowstone-eastern Snake River Plain seismic profiling experiment: crustal structure of Yellowstone. *Journal of Geophysical Research* **87**:2583-2596.
- Smith, R.B. and L.W. Braile. 1994. The Yellowstone Hotspot. *Journal of Volcanology and Geothermal Research* **61**:121-187.
- Sleep, N.H. 1990. Hotspots and mantle plumes: some phenomenology. *Journal of Geophysical Research* **95-B5**:6715-6736.
- Spetzler, J., and R. Snieder. 2004. The Fresnel volume and transmitted waves. *Geophysics* **69**:653-663.
- Stevenson, D.J. 1989. Spontaneous small-scale melt segregation in partial melts undergoing deformation. *Geophysical Research Letters* **16**:1067-1070.
- Stone, D.S. 1991. Scaling laws in dislocation creep. *Acta metall.mater.* **39**:599-608.
- Tackley, P.J., and D.J. Stevenson. 1993. A mechanism for spontaneous self-perpetuating volcanism on the terrestrial planets. *in.*, *Flow and Creep in the Solar System: Observations, Modeling, and Theory*. D.B. Stone and S.K. Runcorn, eds. Kluwer Academic Publishers, Netherlands, p. 307-321.
- Takahashi, E., K. Nakajima, and T.L. Wright. 1998. Origin of the Columbia River Basalts: melting model of a heterogeneous plume head. *Earth and Planetary Science Letters* **162**:63-80
- Tan, B.H., I. Jackson, and J.D. Fitzgerald. 2001. High-temperature viscoelasticity of fine-grained poly-crystalline olivine. *Physics and Chemistry of Minerals* **28**:641-664.
- Tan, E., M. Gurnis, and L. Han. 2002. Slabs in the lower mantle and their modulation of plume formation. *Geochemistry Geophysics Geosystems* **3(11)**:1067
doi:10.1029/2001GC000238.

- Tarantola, A. 2005. Inverse Problem Theory and Methods for Model Parameter Estimation. Society for Industrial and Applied Mathematics, Philadelphia, Pennsylvania.
- Taylor, S.R., B.P. Bonner, and G. Zandt. 1986. Attenuation and scattering of broadband P and S waves across North America. *Journal of Geophysical Research* **91-B7**:7309-7325.
- Teng, T. 1968. Attenuation of body waves and the Q structure of the mantle. *Journal of Geophysical Research* **73-6**:2195-2208.
- Thompson, R.N. 1977. Columbia/Snake River – Yellowstone magmatism in the context of western U.S.A. Cenozoic geodynamics. *Tectonophysics* **39**:621-636.
- Thomson, D.J. 1982. Spectrum estimation and harmonic analysis. *Proceedings of the IEEE* **70**:1055-1096.
- Tilman, F.J., D. McKenzie, and K.F. Priestly. 1998. P and S wave scattering from mantle plumes. *Journal of Geophysical Research* **103-B9**:21145-21163.
- Tonn, R. 1989. Comparison of seven methods for the computation of Q. *Physics of the Earth and Planetary Interiors* **55**:259-268.
- Twiss, R.J., and E.M. Moores. 1992. *Structural Geology*. W.H. Freeman and Company. New York. 532 pp.
- Vidale, J.E. 1986. Complex polarization analysis of particle motion. *Bulletin of the Seismological Society of America* **76**:1393-1405.
- Vidale, J.E. 1987. Waveform effects of a high-velocity, subducted slab. *Geophysical Research Letters* **14**:542-545.
- Waite, G.P., D.L. Schutt, and R.B. Smith. 2006. Models of lithosphere and asthenosphere anisotropic structure of the Yellowstone hot spot from shear wave splitting. *Journal of Geophysical Research* **110**:B11304. doi: 10.1029/2004JB003501.
- Ward, R.W., and C-Y Young. 1980. Mapping seismic attenuation within geothermal systems using teleseisms with application to the Geysers-Clear Lake region. *Journal of Geophysical Research* **85-B10**:5227-5236.
- Warren, L.M., and P.M. Shearer. 2000. Investigating the frequency dependence of mantle Q by stacking P and PP spectra. *Journal of Geophysical Research* **105**:25391-25402.

- Wepfer, W.W., and N.I. Christiansen. 1990. Compressional wave attenuation in oceanic basalts. *Journal of Geophysical Research* **95-B11**:17431-17439.
- White, D.J., and R.M. Clowes. 1994. Seismic attenuation structure beneath the Juan de Fuca Ridge from tomographic inversion of amplitudes. *Journal of Geophysical Research* **99**:3043-3056.
- Wilcock, W.S.D., S.C. Solomon, G.M. Purdy, and D.R. Toomey. 1992. The seismic attenuation structure of a fast-spreading mid-ocean ridge. *Science* **258**:1470-1474.
- Wilcock, W.S.D., S.C. Solomon, G.M. Purdy, and D.R. Toomey. 1995. Seismic attenuation structure of the East Pacific Rise near 9°30'N. *Journal of Geophysical Research* **100**:24,147-24,165.
- Wu, H., and J.M. Lees. 1996. Attenuation structure of Coso Geothermal Area, California, from wave pulse widths. *Bulletin of the Seismological Society of America* **86-5**:1574-1590.
- Yuan, H., and K. Dueker. 2005. Teleseismic P-wave tomogram of the Yellowstone plume. *Geophysical Research Letters* **32**:L07304. doi:10.1029/2004GL022056.